Improvement of current-carrying capabilities of high-temperature superconducting thin films and heterostructures

Khoryushin, Alexey

Publication date:
2011

Document Version
Early version, also known as pre-print

Improvement of current-carrying capabilities of high-temperature superconducting thin films and heterostructures

Alexey Khoryushin

Ph.D. thesis

2011

Department of Physics

Technical University of Denmark

Acknowledgments

This thesis reports the results of my Ph.D. project, which has been carried out at the Department of Physics, Technical University of Denmark under supervision of Prof. Jørn Bindslev Hansen and co-supervision of Prof. Claus Schelde Jacobsen and Dr. Peter B. Mozhaev.

I would like to thank my supervisors for giving me an opportunity to work in the research group, for guiding and teaching me during this project. Their patience and friendly attitude made this work possible.

I wish to acknowledge Prof. Niels Hessel Andersen, Julia E. Mozhaeva, Dr. Vitaliy V. Yurchenko and Dr. Oleksandr Stupakov for their important experimental contributions.

Finally, I would like to thank my family for their love and patience during these years.

Table of Contents

1 Introduction

Superconductivity is a fundamental phenomenon, which is going to play a significant role in future technology. The transmission of electrical current without losses (superconducting power lines), generation of extremely high magnetic fields (superconducting magnetic coils), the most precise magnetic field detection (SQUID, Superconducting Quantum Interference Device) are just some of the key applications of superconductors. The problems of conventional (metallic) superconductors are their relatively low values both for the critical temperature T_c and for the critical magnetic field.

The discovery of superconductivity in metal oxide ceramics took place in 1986 and stimulated intensive research in this area. High temperature superconductivity (HTSC: T_c higher than 25 K) was found in complex oxides of Cu, Bi, V, Tl and Hg, in MgB_2, and in doped fullerenes, and recently FeAs-based superconducting compounds were discovered. Cuprates of the $ReBa_2Cu_3O_x$ family (ReBCO, where Re is Y or a rare-earth element) are the most investigated HTSC materials. Thin epitaxial films of these materials show several orders of magnitude better performance in high magnetic fields than the single crystals, while keeping the same critical temperature. So-called coated conductors are the last generation of superconducting wires. In general, coated conductors consist of a textured metallic substrate, some buffer layers and superconducting layer. State-of-the-art coated conductors have high current-carrying capabilities with real prospects of applications in a number of areas such as superconducting power transmission lines, fault-current limiters, transformers, high field magnetic coils and superconducting motors/generators. High current density in magnetic fields and acceptable energy consumption for cooling allow the construction of superconducting motors/generators of a higher power and/or smaller size, in comparison with electric machines based on conventional conductors.

The HTSC materials are also attractive for fabrication of electronic devices like RF filters and Josephson junction based structures, due to lower microwave losses and a

large energy gap. For example, Nb-based structures with 2.5 meV energy gap are practically limited to frequencies below 600 GHz; the 45 meV energy gap of YBCO extends the frequency range up to 12 THz. Another important benefit of the large energy gap is a higher level of acceptable noise, so the structures can operate at higher temperatures.

Combination of HTSC layers with ferromagnetic layers in complex heterostructures opens a prospect for observing many different effects, which can be utilized for the development of new electronic devices, such as superconducting switching device, based of spin-polarized carriers injection, or π-junctions based on superconductor-ferromagnet-superconductor (SFS) structures, where oscillations of the order parameter damped depending on the thickness of the ferromagnetic layer may result in a stable phase difference across the junction equal to π. The manganates/cobaltates families of materials are a natural choice for the ferromagnetic material in FM/ReBCO heterostructures due to the similar crystal structure, closely matching lattice constants, and low chemical reactivity.

For power applications of ReBCO materials it is important to improve the pinning of the magnetic flux i.e. the critical current density in order to minimize losses. This problem demands detailed knowledge of the nature of the pinning mechanisms in cuprates and good approaches on how to increase the natural pinning. One of the approaches includes different methods of artificial pinning centers formation in the rather stable and reproducible YBCO, another approach is a growth of more complex 3-component (like (Nd,Sm,Gd)BCO) superconductor, which may show a fish-tail behavior.

The cuprate/manganate heterostructures are of interest for power applications based on the well-known magnetic shielding effect, which is capable to increase the engineering current simply by a redistribution of the magnetic field.

2 Motivation

One of the most promising applications of HTSC in the near future is their use in superconducting motor/generator constructions. The substitution of conventional conductors should allow to significantly increase the working field (up to 4-5 T or even higher) with subsequent decrease in size and mass of the machinery for a given power, or construction of more powerful machines. This factor is extremely important for such areas as wind turbines or ship motors. Application of superconductors makes it possible to invent new designs of electrical machines like multi-pole generator design, which allow us to get rid of the complex and expensive gearbox in wind turbine generator.

For the work at 4-5 T the current carrying capabilities of existing coated conductors are insufficient. The critical current density required for superconducting generator is, approximately, 30 kA/cm^2, at the working temperature and field. In order to meet this requirement, the pinning force should be further improved. Redistribution of magnetic flux by magnetic shielding may also play an important role in the overall engineering current improvement.

In addition, cuprate/manganate heterostructures are an interesting object of investigation due to a number of intriguing and unique features of these materials, but for many of experiments and possible applications a smooth homogeneous interface between layers is required. Fabrication of such high-quality heterostructures is an important step towards new progress in this area.

The aim of this work was the study of the possibilities of further improvement of current-carrying capabilities of HTS materials, which should be applicable for a transfer to the coated conductors technology. We were concentrated on the naturally existing precipitates of ReBCO films, namely yttria inclusions, thus the study of influence of deviations of stoichiometry on properties of YBCO films was required. We also studied the possibilities for a controllable segregation of excess material. NBMO manganate material, suitable for high-quality cuprate/manganate heterostructures was investigated.

3 High temperature superconductors

3.1 Magnetic field in HTSC

Most of the metallic superconductors are so-called type-I superconductors. The balance between superconducting and normal states is usually described by three critical parameters: critical temperature, critical magnetic field and critical current density. A schematic phase diagram is shown in Figure 3.1. The existence of type-II superconductors was predicted by A. Abrikosov in 1957 from solution of the Ginzburg-Landau (GL) equations in the $k > 1/(2)^{1/2}$ limit (GL parameter $k = \lambda/\xi$, where λ and ξ are penetration depth and coherence length respectively), which he interpreted as a flux line lattice (FLL) [1].

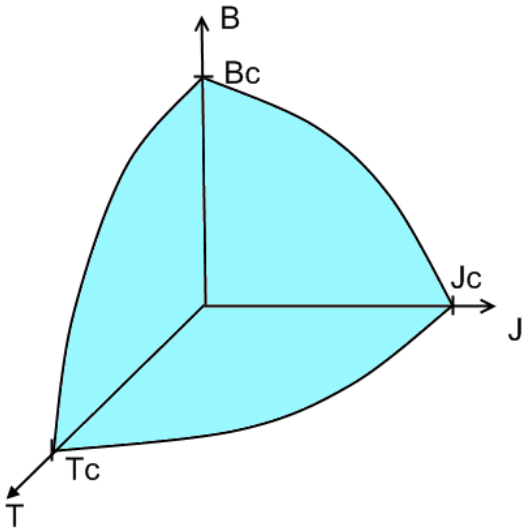

Figure 3.1. Schematic representation of mutual dependency of critical parameters of superconductors

In type-I superconductors, the Meissner state with a complete expulsion of magnetic flux collapses in a magnetic field higher than B_c. Type-II superconductors have much more complex behavior. The surface energy of a type-II superconducting phase is negative, in contrast to the positive surface energy in the case of type-I superconductors. This fact leads to intrusion of magnetic flux into type-II superconductors without collapse of the superconducting order parameter. Above the first critical field B_{c1}, magnetic flux lines, also called magnetic vortices, penetrate type-II superconductors. In the center of the vortex superconductivity is suppressed. The magnetic flux is quantized with a value $\Phi_0 = h/2e$ and screened by supercurrent around the vortex. Outside of the vortices the magnetic field decays exponentially, but with further increase of the magnetic field the density of vortices become higher, and significant interactions between them appear.

For increasing magnetic field the vortex matter goes through various phases (solid, glass-like, liquid phases). Finally, at the second critical field B_{c2} the magnetic field completely suppresses superconductivity. From the GL theory the critical fields for type-I and type-II superconductors are

$$B_c = \frac{\phi_0}{2\sqrt{2}\pi\xi\lambda}, B_{c_1} = \frac{\phi_0}{4\pi\lambda^2}(ln(k) + 0.5), B_{c_2} = \frac{\phi_0}{2\pi\xi^2} = \sqrt{2}kB_c, \quad (3.1)$$

respectively [2].

In a presence of transport current in the superconductor vortices interact with it by means of the Lorentz force. The resulting movement of magnetic vortices is a mechanism of energy dissipation, which may be prevented by pinning forces in the material. The pinning takes place on different kinds of defects and imperfections of the material, like grain boundaries or foreign material inclusions. The shape and the depth of the pinning potential U_0 depend on the properties of the pinning site, such as dimensions of the defect and the amplitude of changes induced in the order parameter and the magnetic field. The pinning force f_p is the first derivative of the pinning potential with respect to the distance between the vortex and the center of the pinning site, $\overline{f_p} = -\frac{dU_0}{d(\overline{r} - \overline{r_0})}$. An overall maximum pinning force F_p normalized by volume is given by:

$$\frac{F_p}{V} = J_c \times B, \quad (3.2)$$

where the J_c is the critical current density at the magnetic field B.

Pinning sites may be classified with respect to their geometry in point, linear and planar defects. Linear defects parallel to the direction of the magnetic field involve the whole length of the vortex into the interaction, so they obviously produce much stronger pinning forces than small point-like inclusions. The planar defects are effective only if the direction of the Lorentz force is perpendicular to the plane of the defect.

The Bose-glass model [3] gives an acceptable approximation for the behavior of linear defects. At low fields the interaction between vortices is weak and may be ignored, in

comparison with the strong interaction of the vortices with pinning sites. The overall pinning force is represented by a sum over pinning forces of sites occupied by vortices, i.e.:

$$\frac{F_p}{V} = \frac{F_p}{St} = J_c \times B = J_c \times \frac{\phi_0 n}{S}, \tag{3.3}$$

where S is the area, t is the thickness of the superconductor, and n is the number of vortices. If we introduce here the pinning force of an individual linear defect, normalized per unit of length $f_p = \Phi_p / n / t$, from (3.3) we get:

$$J_c = \frac{f_p}{\phi_0}, \tag{3.4}$$

With increasing field, the distance between neighboring vortices decreases and the vortex-vortex interaction becomes important. The vortices repel each other and tend to arrange themselves into a triangular vortex lattice. The vortex-vortex distance in the lattice is given by:

$$a = \sqrt{\frac{2}{\sqrt{3}} \frac{\phi_0}{B}}, \tag{3.5}$$

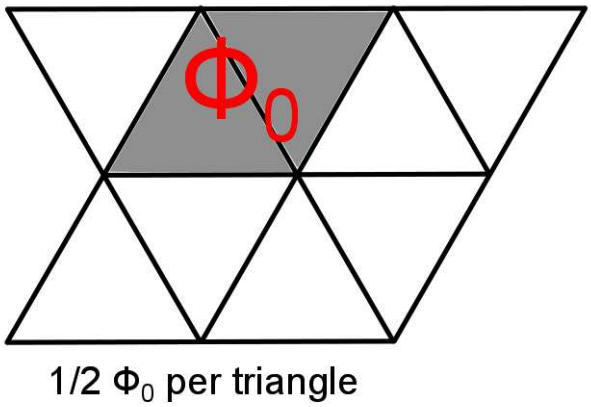

Figure 3.2. Illustration of triangular vortex lattice

that gives approximately 22 nm at 5 T. The accommodation field is the point at which the energy of interaction with the flux lattice exceeds the pinning energy. Above this field the collective pinning becomes dominant. This field range can be further subdivided into the moderate field region, where an interaction of vortices may be described in terms of a shear modulus of the flux lattice, and the high field region with multiple vortices pinning on the individual pinning center. According to [3], the field dependencies of the critical current density for these regions are $J_c \sim B^{-1/2}$ and $J_c \sim B^{-1}$, respectively.

At fields below the so-called irreversibility field the vortices are fixed on the pinning sites by individual or collective pinning. Above this field the Lorentz force overcomes the pinning forces and the vortices start to move, leading to a certain resistance for the transport current, no matter that the material is still superconducting.

3.2 High power applications

Before the discovery of high temperature superconductors (HTSC) the power applications of superconductivity were limited to fabrication of strong superconducting magnets, with almost dominant use of the low-temperature superconductors (LTS) NbTi (T_c = 9 K) and Nb_3Sn (T_c = 18 K). These magnets are still covering the needs of magnetic resonance imaging (MRI) and nuclear magnetic resonance (NMR) setups, as well as high-energy accelerators and plasma fusion devices.

Figure 3.3 illustrates phase diagrams of various superconductors, which are known nowadays. HTSC materials open new prospects for superconducting technology, enabling not only dc applications (where they have to compete with relatively cheap, well established and reliable LTS materials), but also ac power applications, which are not possible for LTS materials. AC losses (eddy current losses, hysteresis losses) cause heat release which is hard to deal with due to stiff cooling penalty at low temperatures. Thus, except for the common use of superconductors for high magnetic field dc applications, HTS are promising materials for power applications, such as transmission lines, fault-current limiters, transformers, high power compact motors and generators.

For practical applications of superconducting wires, irrespectively of the particular SC material, there are a number of requirements, which need to be fulfilled. Apart from the obvious presence of superconductivity at the working temperature and magnetic field, superconducting wires and tapes should be protected against thermal quenching, be sufficiently strong mechanically to resist the thermal stresses during cool-down and electromagnetic stresses at the payload. These problems demand addition of a matrix or a substrate/capping layer of normal metal for superconducting filaments, in order to provide good thermal conductivity and mechanical support. Usually the requested

engineering current density is 10^4-10^5A/cm^2 in the working magnetic field (for the cross section of the whole wire, including the substrates, buffer and capping layers and the superconducting filament itself).

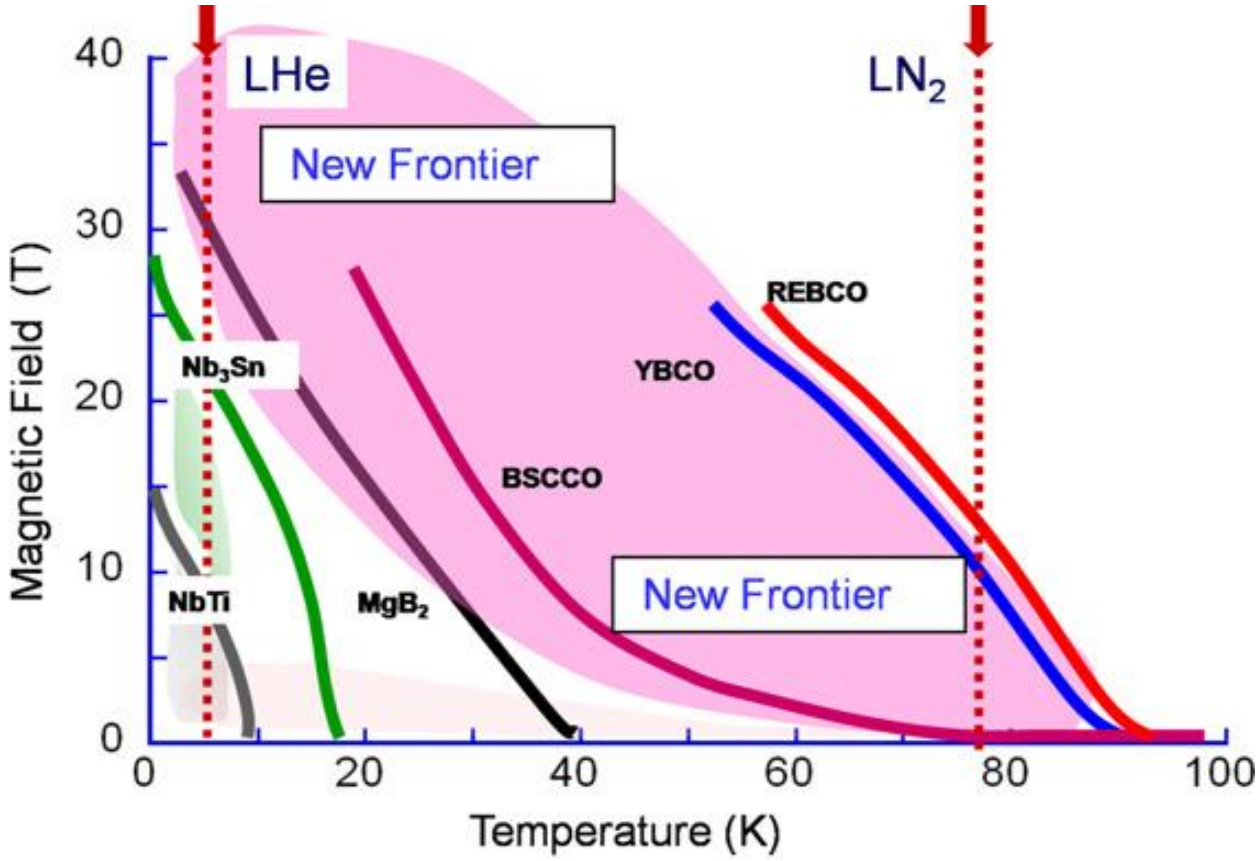

Figure 3.3. Upper critical field versus temperature dependence for different superconducting materials [4]

Another important parameter for real applications of superconductors is the price, which is normally given per kiloamp-meters (kAm). LTS are currently in use for high field dc applications, where there are no conventional alternatives to superconducting technology. New materials, such as BSCCO, ReBCO and MgB_2 are able to substitute them in this area if the large-scale production can be done with an acceptable price (while having an advantage of higher operational temperature, i.e. much lower cryogenic cooling). For ac applications, HTSC have to compete with conventional copper-based solutions. As reference points for comparison, NbTi wires are about \$1/kAm (at the liquid He temperature), and copper wires are \$15-25/kAm [5].

3.3 High-temperature superconducting cuprates

Superconducting cuprates were discovered in 1986 [6]. High critical temperature and high values of critical current density in the presence of magnetic field keep the attention of researchers and engineers on this broad family of materials.

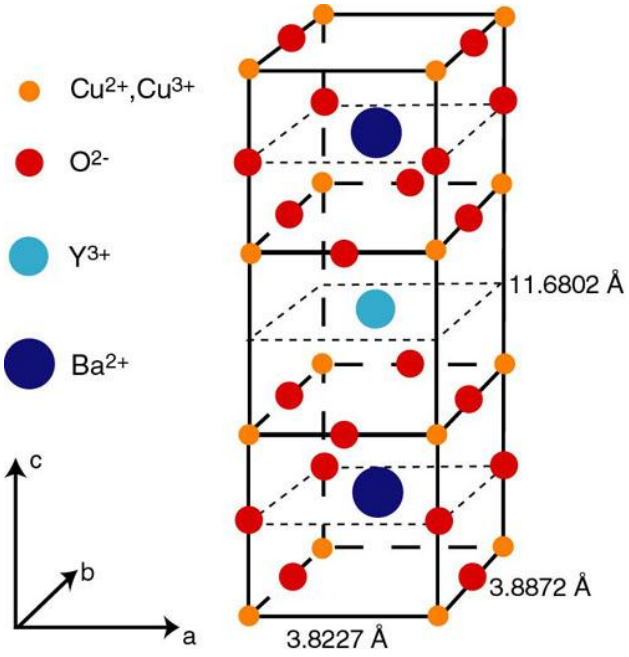

Figure 3.4. YBCO unit cell. Lattice constants are given as examples and may differ significantly, in dependency on oxygen content and its distribution on vacant positions in the structure (which are also the reasons of crystal structure distortion, from tetragonal to orthorhombic).

The structure of superconducting cuprates consists of CuO_2 layers divided by stabilizing interlayers of different metal oxides. The most simple $(Me)CuO_3$ perovskite crystal structure is not stable enough, so additional layers of different metal oxides are present in high-temperature superconducting cuprates. In general the structure of superconducting cuprates consists of four metal oxide layers:

copper oxide, Me^1 metal within a simple perovskite cell, Me^2 which acts as an additional stabilizing layer and Me^3 metal which provides connection between Me^2 and the next copper oxide layer. The general formula for superconducting cuprates may be represented as $Me^2{}_mMe^3{}_2Me^1{}_{n-1}Cu_nO_x$, where n is a number of superconducting layers and m is number of stabilizing layers, respectively. The widely used $Bi_2Sr_2CaCu_2O_8$ material is a typical example of such a structure. The conducting properties of these materials are complicated, and in the superconducting state are similar to the properties of a composite structure of superconducting (CuO_2) and non-superconducting (Me^2 oxide) layers.

Naturally, these materials are highly anisotropic, and the superconductivity is several orders of magnitude weaker in the *c*–direction, since the supercurrent is crossing the non-superconducting Me^2 oxide layers, as compared to the *(ab)* – plane, where the supercurrent is flowing along superconducting copper oxide planes.

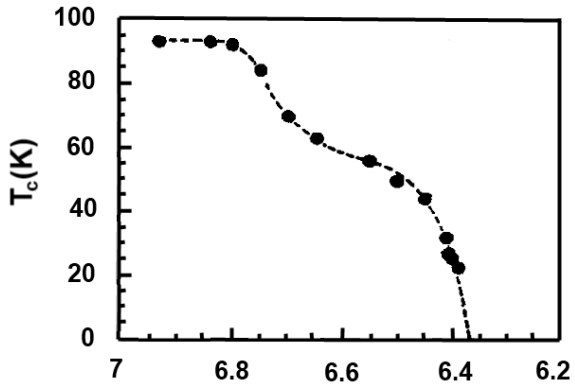

Figure 3.5. T_c of YBCO versus the oxygen content, atoms per unit cell [7]

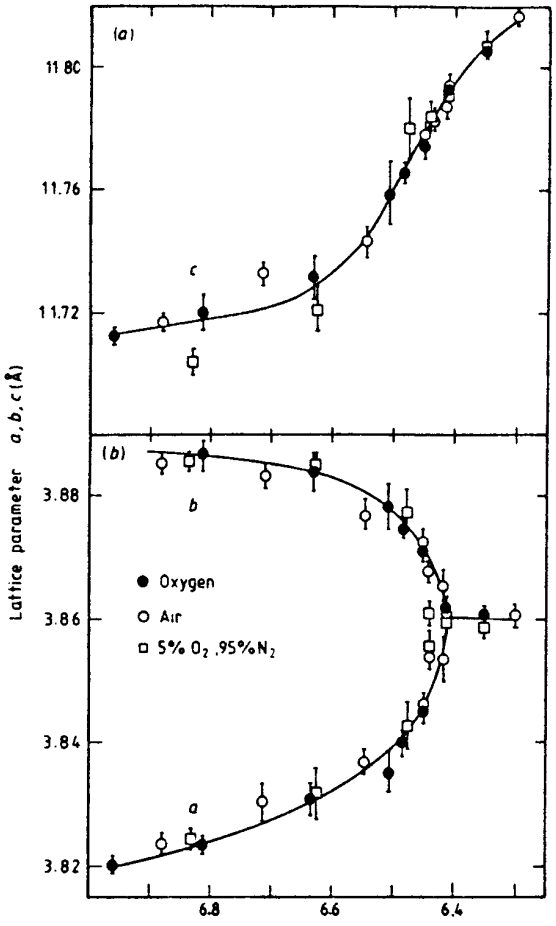

Figure 3.6. Lattice constants of YBCO versus the oxygen content, atoms per unit cell [8], for $x \geq 6.4$ $a \neq b$

In contrast to other HTS cuprates, in the $ReBa_2Cu_3O_x$ family a CuO layer represents one of the metal oxide stabilizing layers. Following the general notation, the ReBCO formula may be written as $CuBa_2(Re)Cu_2O_x$.

This oxygen disorder in the CuO stabilizing layer leads to formation of segments of CuO_2. This factor is crucial for the strong coupling between the CuO_2 superconducting planes, and a subsequent decrease of the superconducting anisotropy. Thus, the anisotropy ratio $\Gamma = \lambda_c / \lambda_{ab} = \xi_{ab} / \xi_c$ is about 5 for $YBa_2Cu_3O_x$, compared to more than 150 for $Bi_2Sr_2CaCu_2O_8$ [2].

$YBa_2Cu_3O_x$ (YBCO, Figure 3.4) is the most widely investigated material of the family, due to its good reproducibility with high T_c, high critical current density and relatively low anisotropy. The YBCO properties are very sensitive to the oxygen content. The number of oxygen atoms per unit cell x is often written as 7- δ, where δ is representing the amount of oxygen missing in the CuO stabilizing layer. At low oxygen content (δ close to 1) YBCO has tetragonal crystal structure and is not superconducting.

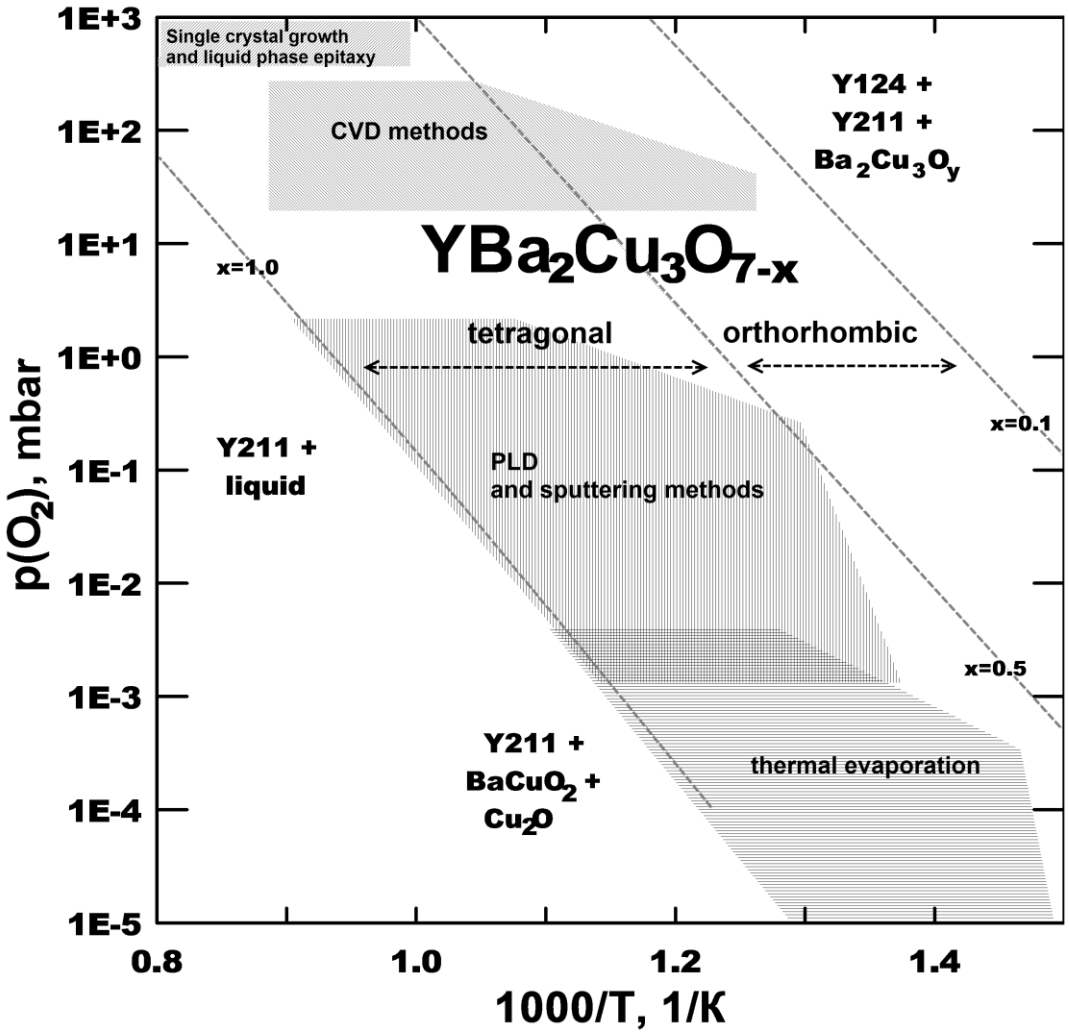

Figure 3.7. Thermodynamic phase stability limits of YBCO (schematic representation) [9]. Shaded regions correspond to deposition parameters of different techniques.

While filling the "CuO" plane with oxygen, YBCO keeps the tetragonal structure up to δ ~ 0.6. At higher oxygen content in the structure of YBCO, oxygen atoms become ordered in the CuO-chains, transforming the tetragonal phase to an orthorhombic one, which is superconducting. An additional oxygen ion in the CuO layer dopes the

superconducting CuO_2 layer with hole. The optimal doping level results in the highest T_c. The dependencies of T_c and lattice constants of YBCO on oxygen content are shown in Figure 3.5 and Figure 3.6, respectively.

The phase diagram of YBCO in Figure 3.7 shows the stability region in the oxygen partial pressure - substrate temperature coordinates during the deposition. At these parameters the YBCO (Y123) crystal structure is growing, rather than separate oxides or other possible phases. The best quality of the film may be obtained close to the lower limit (the so-called decomposition line) [9]. From another point of view, the saturation with oxygen (in YBCO the number of oxygen atoms per unit cell cannot exceed 7, which corresponds to $\delta = 0$) is necessary for good superconducting properties. In order to address this issue, most of the fabrication methods include an oxygenation stage subsequent to the growth of the crystal structure.

3.4 Pinning sites in ReBCO materials

A variety of natural pinning sites are observed in ReBCO films. Point defects in ReBCO materials are represented by vacancies and inclusions in the crystal structure, either due to local non-stoichiometry or due to foreign material contamination. Linear defects include dislocations and elongated foreign phase inclusions. Stacking faults as well as grain, twin boundaries and anti-phase boundaries are planar defects. The density of natural pinning sites varies for different fabrication techniques and fabrication routine parameters. The presence of numerous defects is the main reason for the much higher critical current densities of ReBCO films (J_c up to 3-7 MA/cm^2 at 0 T, 0.02-0.5 MA/cm^2 at 1-5 T for “pure” YBCO films at 77 K [4]), as compared with the J_c of single crystals.

To improve the critical current density in high magnetic fields, introduction of artificial pinning centers (APC) is required. In order to reach the maximum possible critical current at given magnetic field, the APCs have to be of optimal density and shape (size). Both these parameters are, in general, empirical, due to their complex influence on the properties of superconductors. It is widely accepted that efficient pinning site size is order of the coherence length ξ. Despite some theoretical predictions of the penetration

depth as an optimal size for high k-superconductors ($\lambda > \xi$) [10], the coherence length is closer to the optimum at high fields. Obviously, pinning sites are the areas of suppressed superconductivity and disturbed crystal structure, and can not substitute a big fraction of the superconducting film without deteriorating the superconducting properties of the rest of the film. That factor limits the matching field (the field at which the number of vortices and the number of pinning sites are equal, and, in case of strong pinning sites, only individual pinning is important) to very low fields, as soon as the size of the defects is too big. Thus, for YBCO (ξ ~ 3 nm, λ ~ 100 nm) and given volume fraction of columnar inclusions (2-dimensional defects) there is three orders of magnitude difference in the density of inclusions of diameter equals to ξ and λ, respectively. The corresponding difference in matching field cannot be compensated by higher pinning force of individual pinning sites of less dense and larger inclusions.

The methods of APCs production may be classified according the way they are incorporated into the superconducting medium:

1) by promoting the formation of natural defects, such as dislocations, stacking faults and grain boundaries;
2) by introducing foreign phases into the superconducting film;
3) by modifying the film after fabrication, for example, by heavy ion irradiation.

A significant part of the research on APCs is focused on the Pulsed Laser Deposition (PLD) technique (described in a separate Chapter 5). This choice is motivated by the great flexibility of the technique, which is vital for any early stage investigations. In this work the PLD is the only method, which was used for epitaxial films fabrication, so this short review will be limited to this method.

Efficient modification methods on APCs formation, like heavy ion irradiation [11] or even nanolithography [12,13] are too expensive for large-scale production. By tuning the fabrication routine parameters it is possible to increase the density of natural defects (for example, an increase of the density of dislocations from 5 to 70 μm^{-2} by tuning the deposition parameters, with a subsequent increase of the characteristic field from 20 to 100 mT was shown in [14]), but this method is not flexible enough to control the

density of natural pinning sites in the range necessary for high magnetic fields. The surface decoration is a more promising method of that kind [15]: according to *Matsumoto et al.*, Y_2O_3 nanoislands deposited on the substrate before YBCO deposition, promote formation of dense dislocations in YBCO films.

The most popular and fruitful approach is the introduction of a foreign phase into the HTSC film. A large variety of materials were utilized for this role, from metals (Au, Ag) to materials from the YBCO phase diagram (Y_2O_3, Y_2BaCuO_5) and different perovskites ($BaZrO_3$, $BaSnO_3$) [4]. Different techniques are in use: multilayer film fabrication (alternating YBCO target with second phase target during the deposition), composite targets, made by cutting a sector from a YBCO target and substituting it with a foreign phase sector, or by direct doping of the target.

The introduction of inclusions with element composition different from the superconducting phase (e.g. containing Zr, Sn, Al, etc.) suppresses the superconducting properties of the surrounding area of HTSC material. The main factors of this suppression are chemical interaction and excess strain. This problem limits the use of such materials to 2-5 % volume percentage (for different APC materials [16,17]).

This makes the "natural" inclusions, consisting of the same elements as the HTSC material, more favorable as APCs. Such inclusions are always present in HTSC thin films due to local non-stoichiometry or non-optimal deposition conditions. Different Cu-containing oxides (CuO_x, $BaCuO_x$) segregate primarily on the film surface. In contrary, the Y_2BaCuO_5 ("green phase") and Y_2O_3 (yttria) may be incorporated into the YBCO matrix, forming nano-scale inclusions in it. The Y_2BaCuO_5 nanoparticles are relatively large and have significant mismatch of lattice constants (with YBCO), so their formation may result in cracks of the superconducting matrix [18]. Y_2O_3 segregates in smaller inclusions with a coherent interface with the YBCO matrix due to a good match of the lattice constants [19]. The shape of Y_2O_3 inclusions varies from small inclusions (3-5 nm in diameter) to larger elongated rectangular particles (0.1 μm) and columnar inclusions (~10 nm in diameter).

Another promising approach is the use of multi-element composition cuprates (Re1,Re2,Re3)BCO, such as $(Nd,Sm,Gd)_1Ba_2Cu_3O_x$ [20]. Doping of NBCO with Gd in general increases the crystal structure quality, and an addition of Sm (or Eu) is necessary for the mutual solubility of the Nd and Gd fractions. Due to cation disorder in the Re/Ba (for a significant effect, the Re element should be of the light rare earth family – Nd, Sm, Eu, Gd) subsystem, the film consists of areas of different T_c. With increasing magnetic field the areas of weaker superconductivity become non-superconducting and work as pinning centers. This mechanism may result in an increase of J_c with magnetic field, which is known as the "fishtail" effect.

3.5 HTS superconducting wires and coated conductors

The first generation of HTS commercially available wires is based on $(Bi,Pb)_2Sr_2Ca_2Cu_3O_{10}$ (BSCCO-2223, T_c = 110 K) superconductor embedded into a silver matrix. In spite of the many beneficial characteristics of this type of conductors, such as established large-scale production routine and good performance in self-field, relatively low critical current densities in high magnetic fields, the strong anisotropy and the high cost (~$150/kAm) due to the use of silver as a matrix for SC filaments lead to intensive work on development of a second generation of HTS wires, so-called coated conductors, based on the ReBCO family of materials.

An illustration of a coated conductor structure is given in Figure 3.8. The superconductor in a coated conductor exists as a layer of epitaxial ReBCO film (0.2-1 μm), with only low angle misorientations between the grains, providing strong intergrain coupling, i.e. high critical current densities of the superconductor. The superconducting film is fabricated on a flexible metallic substrate of Ni or $Ni_{0.95}W_{0.05}$ alloy, or even of stainless steel with a textured buffer layer(s) of magnesium oxide MgO, yttria-stabilized zirconia (YSZ) or gadolinium zirconate $GdZrO_3$ [5]. The texture can be formed either by texturing the metal substrate (rolling assisted biaxially textured substrate, or RABiTS) or by texturing the buffer layer (by ion beam assisted deposition,

IBAD, or inclined substrate deposition, ISD). The RABiTS is a more promising approach since it does not involve expensive vacuum processes.

The required functionalities of the buffer layer (transfer of texture on the metal-oxide interface, oxygen diffusion barrier, Ni diffusion barrier, capping layer for an epitaxial ReBCO growth) lead to the use of complex multilayer buffers, often involving Y_2O_3, NiO, YSZ, MgO, CeO_2 and other materials.

A variety of physical deposition methods providing good superconducting properties of small samples of ReBCO are, in general, too expensive for large scale production, so

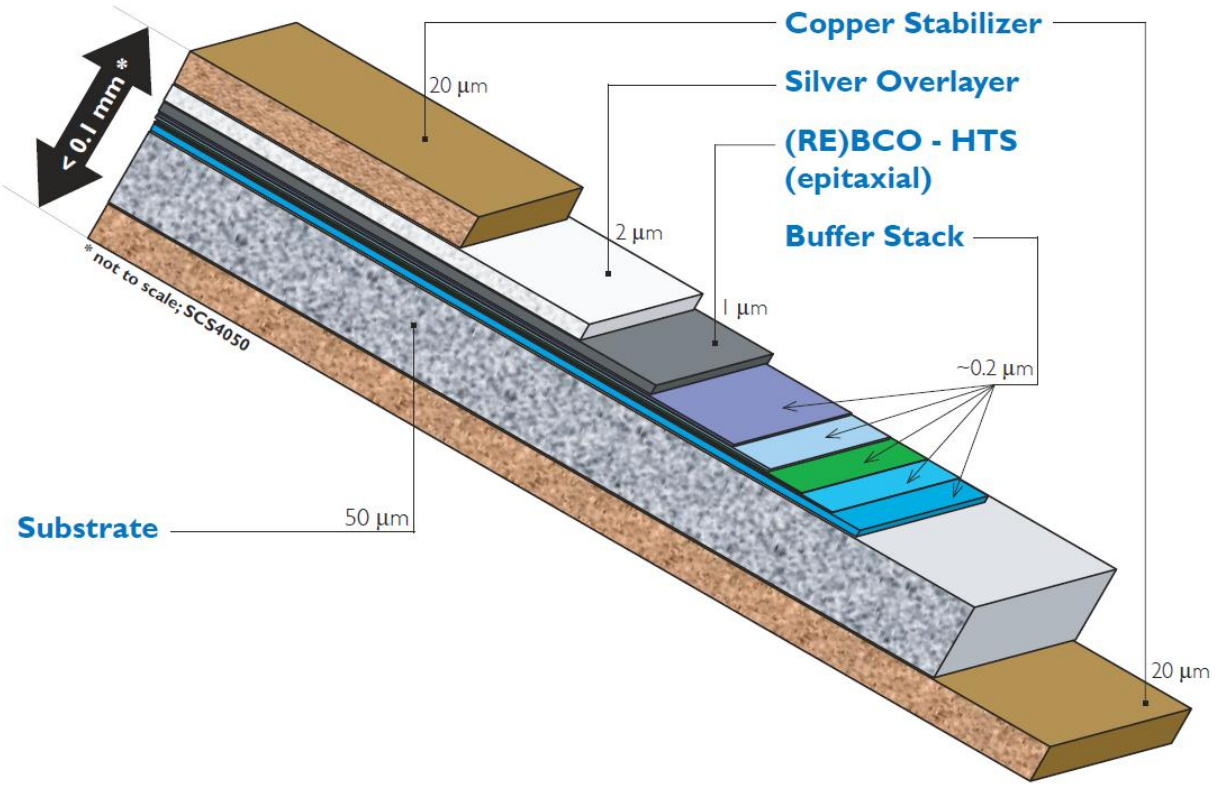

Figure 3.8. Structure of coated conductor (SuperPower inc)

the industrial deposition methods for the superconducting layer are chemical, such as liquid-phase route by metal-organic deposition (MOD) [21] or metal-organic-chemical vapor deposition (MOCVD) [22].

It is worth mentioning that one of the obstacles to increasing the engineering critical current of coated conductors by simply increasing the thickness of superconducting

layer is a significant degradation of the critical current density J_c when the layer becomes thicker than 0.5 μm. The main reasons for this behavior are substitution of *c*-oriented film by *a*-orientation and loss of epitaxy due to high levels of accumulated strain [27].

All the steps of the fabrication of coated conductors, including substrate preparation, texture formation, buffer layers, and ReBCO fabrication methods are undergoing active development. The expected progress in these areas is likely to reduce the price down to $10/kAm (0 T, 77 K), a price, which is below the level of copper wires, thereby opening wide possibilities for HTSC applications in the power industry.

4 Cuprate-manganate heterostructures

4.1 Motivation and choice of materials

Cuprate/manganate heterostructures are investigated in a number of recent publications [23-25], these structures are interesting from the scientific point of view as well as taking into account possible applications. Colossal magnetoresistance in manganate films, injection of spin-polarized carriers from FM to SC (might be used for superconducting switching devices), proximity effect, influence of magnetic screening on current-carrying capabilities of SC films, mixture of two antipodal types of ordering in the interlayer area, the study of which can give an important piece of information about the nature of superconductivity in HTSC – all these and a number of not mentioned effects and interesting configurations of FM/SC thin film layered structures make this field so attractive. Most of the work in this area was done with the (La,M)MnO_3 (M – Ca, Sr, Ba, Pb) [26] group of materials, and $YBa_2Cu_3O_x$ as a superconductor.

For many possible applications fine homogeneous interfaces between ferromagnetic and superconducting layers are required, that demands smooth surfaces, low level of lattice mismatch and full epitaxial growth and high crystal quality of every layer. The problem of mutual element diffusion and the consequent degradation of SC/FM interlayers should also be kept in mind. The last demand seems to be a weak point of the most widely used (La,Sr)MnO_3 and (La,Ca)MnO_3 compounds, due to the relatively high probability of substitution of Ba ions in the ReBCO lattice by Ca and Sr ions, which leads to suppression of both superconductivity and ferromagnetic order in the interlayer.

Due to suppression of local stoichiometry deviations by disorder in the cation system of Nd/Ba ions, $NdBa_2Cu_3O_7$ superconducting thin films grow in a pseudo cubic mode (NdBa)CuO_x. This leads to layer-by-layer growth with formation of smooth surfaces (R_a ~ 1-3 nm), in contrast to the spiral growth of $YBa_2Cu_3O_x$ (R_a ~ 5-15 nm). The deposition rate for $NdBa_2Cu_3O_7$ has to be much lower than the typical values for other

ReBCO materials, otherwise the pseudocubic phase would recrystallize into a mixture of *a*- and *c*- oriented grains [27].

$(NdBa)MnO_3$ is an interesting but not a very well studied member of the manganate family. We consider it as a promising candidate for the ferromagnetic material in SC(ReBCO)/FM bi-layers. The use of identical cations in cuprate and manganate films should reduce the problem of interdiffusion. At the same time, this material has relatively high T_{Curie} and magnetic moment (~135 K and 3.0 μ_B/cell in the cubic phase, ~300 K and 0.7 μ_B/cell in the Nd-Ba ordered orthorhombic phase), perovskite crystal structure and small lattice mismatch with ReBCO (lattice constant in bulk ~ 3.89 Å).

On the other hand, taking into account the published influence of internal strain on the magnetic properties of materials of $(RBa)MnO_3$ family and the lowest level of internal strain in the case of the $(NdBa)MnO_3$ ([28]) we could expect significant dependence of its magnetic behavior on the deposition conditions and the substrate properties (Figure 4.3).

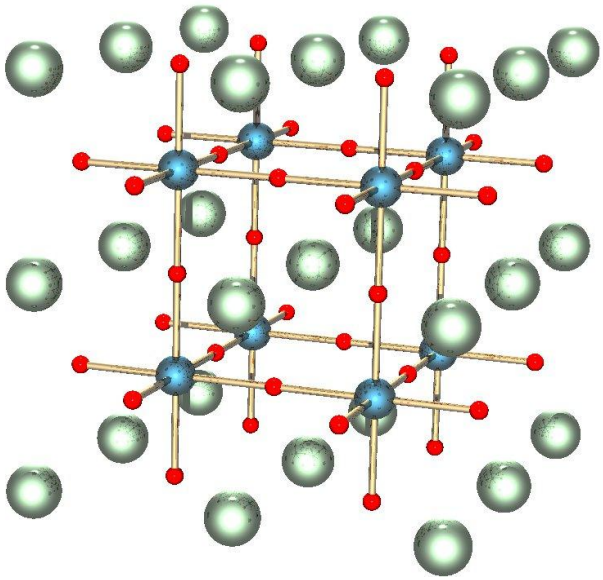

Figure 4.1. Perovskite structure (for manganates, small red balls are oxygen atoms, big green balls are rare-earth elements and blue balls are manganese atoms)

4.2 Manganates

The main interest in rare-earth manganates started with the discovery of the colossal magnetoresistance effect (CMR). The magnetism in these compounds has a complicated nature, and the ferromagnetic-paramagnetic and metal-insulator transitions are coupled. The rare-earth manganates have a general formula $R_{1-x}A_xMnO_3$ (R = La, Nd, Pr, Sm, etc., and A = Ca, Sr, Ba, Pb) and the perovskite crystal structure (Figure 4.1).

As an example, let us consider $LaMnO_3$, which is one of the parent compounds. It is an antiferromagnetic insulator, Mn^{3+} ions are ordered in the same direction in planes and the planes are antiparallel [29]. The situation can be changed by doping. In a presence of Mn^{4+} ions these compounds may become ferromagnetic with Curie temperatures ranging from 100 K up to 400 K, depending on the concentration of Mn^{4+} ions and the dopant. At some levels of doping the compounds may behave as charge-ordered insulators (COI) or as antiferromagnets.

The ferromagnetic transition is followed by a rise of conductivity (a transition to a metallic state). Typical R(T), M(T) are presented in Figure 4.2. Colossal magnetoresistance (CMR) is an impressive effect of a huge decrease in resistance in an applied magnetic field.

In general, an interplay between magnetic, Coulomb, and lattice interactions takes place. This is the so-called the double exchange interaction, proposed by De Gennes, and extended to manganese ions by Anderson and Hasegawa [30,31].

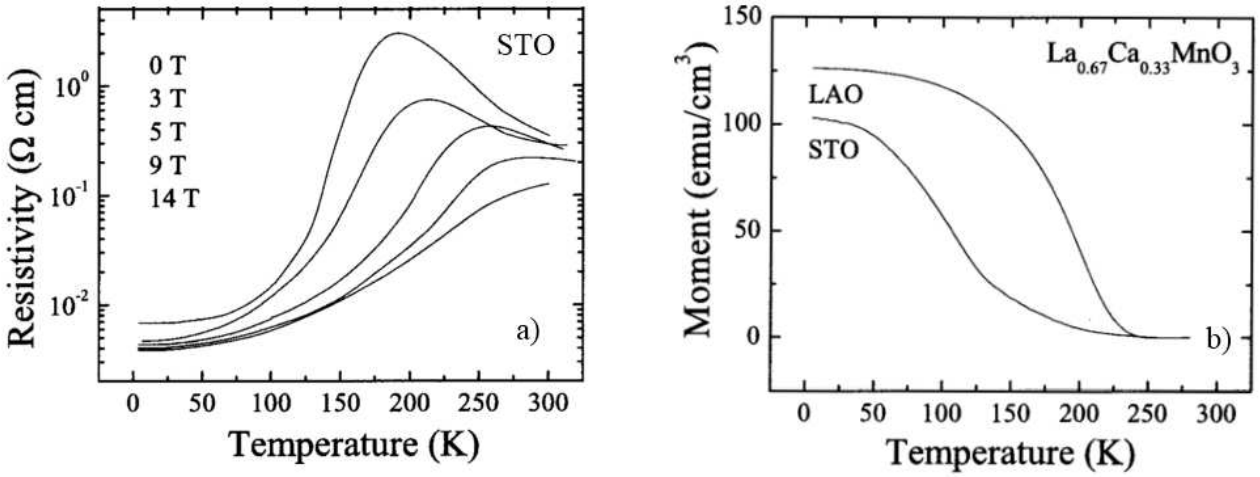

Figure 4.2. Typical magnetoresistance, magnetization versus temperature dependences, $La_{0.67}Ca_{0.33}MnO_3$ [32]

The basic idea is that a local exchange interaction exists for magnetic ions and spin-polarized carriers (so-called magnetic polarons), when the alignment of ionic spins below the Curie temperature gives rise to a global spin-polarization of the carriers. The

polarization of the charge carriers can be probed by several techniques such as tunneling studies, Andreev reflection measurements and photoemission measurements.

Substrate	Effective lattice constant, Å	Mismatch with NBMO, %
r-cut Al_2O_3, sapphire, 4.78×5.14 Å	3.51	- 10.8
YSZ, yttria-stabilized zirconia	3.65	- 6.6
CeO_2, cerium oxide	3.84	- 1.3
NGO (110), $NdGaO_3$ - neodymium gallate, a = 5.426 Å, b = 5.502 Å	3.862	- 0.8
LSAT (100), $(LaAlO_3)_{.3}$-$(Sr_2AlTaO_8)_{.7}$	3.867	- 0.6
(NdBa)MnO_3, investigated material (for a comparison)	3.89	0.0
STO (100), SrTiO3 - strontium titanium oxide	3.905	+ 0.4
PMN-PT, $Pb_{1-x}[(Mg_{1/3}Nb_{2/3})O_3]_xPbTiO_3$	4.02	+ 3.3 +/- 0.2
MgO, magnesium oxide	4.212	+ 7.4

Table 4.1 Effective lattice constants of some suitable single crystal substrates/buffer layers

Lattice effects can strongly affect the carrier mobility and the magnetism in these materials due to electron-lattice interaction induced by a Jahn-Teller (JT) distortion around the Mn^{3+} ions. An orthorhombic distortion tends to localize the carriers, i.e. the ferromagnetic metallic state is suppressed. In manganates with small A-site cations (r_A < 1.25 Å) and x near 0.5, the Coulomb interaction at sufficiently low temperature (T_{CO}) becomes stronger than the kinetic energy of the electrons leading to an ordered arrangement of the Mn^{3+} and Mn^{4+} cations. Increasing r_A increases the ferromagnetic T_c in the manganates exhibiting CMR [33].

It is now evident that external in-plane strain, induced by the substrate in the case of epitaxial cube-on-cube growth may dramatically change the properties of manganate films. One of the possible approaches for the investigation of the strain effect is depositions on a number of substrates with different lattice mismatch [32,34], another

one is the use of piezoelectric substrates like $Pb_{1-x}[(Mg_{1/3}Nb_{2/3})O_3]_xPbTiO_3$ (PMN-PT) [35-38]. There are some benefits and drawbacks for both approaches.

The first method allows us to obtain discrete data for a number of lattice mismatch values covering a wide range (see Table 4.1), the use of high-quality single crystal substrates usually results in a good epitaxial growth. But, on the other hand, films deposited on the different substrates may vary in oxygen content, local non-stoichiometry, crystalline size and quality, even the formation of a dead layer. Apart from the induced strain there could be many other factors, which are important during the growth of the film (initial adhesion levels for different elements, density of active sites for film growth, chemical reactivity, diffusion of the compounds of the substrate into the film, thermal expansion effects), so lattice strain effects should be distinguished from these factors.

The second method is a much more clear experiment, in some sense: all the changes are applied after the deposition, and a direct comparison between different strain levels is possible. However, the use of a ferroelectric substrate makes it hard to examine the magnetic properties of the film. The range of applied strain is also limited to a narrow tensile region (PMN-PT has the lattice constant ~ 4.02 Å, and only small changes of the lattice constant are possible [36]).

The changes in charge/magnetic ordering may be examined by magnetoresistance measurements, accompanied by magnetic measurements. The effects of external strain on the crystal structure of the film can be quantified by X-ray diffractometry methods (XRD). Substrate-induced strain may usually be considered as isotropic in-plane strain ($\varepsilon_{xx} = \varepsilon_{yy}$), which is related to out-of-plane strain ε_{zz} by the following expression:

$$\varepsilon_{zz} = \frac{2\nu}{\nu - 1}\varepsilon_{xx}, \tag{4.1}$$

where ν is the Poisson's ratio, which is material-dependent. There is no clear agreement in the literature on Poisson's ratio of manganates, the values which are utilized are from $\nu = 0.3$ [39], which is typical for oxides, up to $\nu = 0.5$, which corresponds to volume-

preserving dilation [40]. The strain values may be expressed from the film and the bulk lattice constants:

$$\varepsilon_{xx} = \frac{a_{bulk} - a_{film}}{a_{bulk}}, \quad \varepsilon_{yy} = \frac{b_{bulk} - b_{film}}{b_{bulk}}, \quad \varepsilon_{zz} = \frac{c_{bulk} - c_{film}}{c_{bulk}}, \tag{4.2}$$

The overall induced strain may be described as a combination of uniform compression (expansion) and bi-axial dilation. The bi-axial distortion increases the JT interaction, which tends to localize the electrons, and uniform strain (3D, or bulk strain) changes the Mn-O bond length and affects the electron-lattice coupling. In this simple model, the behavior of T_p (the metal-insulator transition temperature) may be described by the following expression [39,41]:

$$\begin{aligned} &\mathrm{T}_{\ p}(\varepsilon) = T_p(0) \cdot (1 - \alpha \cdot \varepsilon_{bulk} - \frac{\Delta}{2} \cdot {\varepsilon_{JT}}^2), \\ &\text{where} \quad \alpha = \frac{1}{T_p} \cdot \frac{dT_p}{d\varepsilon_{bulk}}, \quad \Delta = \frac{1}{T_p} \cdot \frac{d^2T_p}{d{\varepsilon_{JT}}^2}, \end{aligned} \tag{4.3}$$

$\varepsilon_{bulk} = \varepsilon_{zz} + 2\varepsilon_{xx}$ and $\varepsilon_{JT} = (\varepsilon_{zz} - \varepsilon_{xx})/2$ represent bulk and bi-axial (Jahn-Teller) strain. The bulk part depends on sign of the strain, but the JT contribution is always negative, and suppresses magnetic ordering. The actual T_p variation may be positive or negative, depending on the sign and the magnitude of the stain.

The general trend for most studied manganates with doping level $0.2 < x < 0.5$ is a suppression of FM ordering and stabilization of CO (charge-ordered) state by tensile strain, and increase of T_c, T_p by compressive strain. This tendency was confirmed for $La_{1-x}Ca_xMnO_3$ (x = 0.25, 0.3, 0.5) [3,8,9], $La_{0.7}Sr_{0.3}MnO_3$ [36,37], $Pr_{0.5}Ca_{0.5}MnO_3$ [38], $La_{0.7}Ba_{0.3}MnO_3$ [40], but for instance for low levels of doping of $La_{1-x}Ba_xMnO_3$ ($0.05 < x < 0.2$) it was reported that the behavior is opposite [42]. At the same time, in some works [43,44] suppression of the FM ordering in $La_{0.67}M_{0.33}MnO_3$ (M = Ba, Ca) films by substrate-induced compressive strain was reported.

The oxygen content of the CMR materials is an important factor, which strongly affects the magnetic and transport properties [45]. The depletion of Mn^{4+} ions due to

insufficient oxygenation leads to weakening of the double exchange interaction i.e. a rise of the resistivity and a suppression of the FM ordering.

Differences in thermal expansion coefficients between the film and the substrate may in principle affect the induced strain value, but for the perovskites these coefficients are similar, and do not play any significant role. The thickness of the films is another important parameter for strain effects. The typical critical thickness for strain relaxation is about 50-100 nm, for thicker films we should expect increasing strain inhomogeneity. However, it is a factor, which depends on the quality of the film: in a paper of Xiong at al. [32] conservation of lattice distortion for manganate films as thick as 200 nm was reported.

4.3 (NdBa)MnO_3.

The $R_{1-x}A_xMnO_3$ manganate sub-family with Ba on the A position is much less studied than compositions with Ca, Sr. The main attention was attracted to the $La_{1-x}Ba_xMnO_3$ system, which exhibits very high T_c, due to the large ionic radius of La. However, a few works on $R_{1-x}Ba_xMnO_3$ materials can be found in the literature.

A series of papers on the bulk properties of ordered (in cation sub-system) and disordered Ba-based 50%-doped manganates were published by T. Nakajima, et al [28]. A complicated phase diagram (Figure 4.3, [28]) demonstrates the main features of ordered $RBaMn_2O_6$ compounds. An orthorhombic distortion of the lattice depends on the mismatch between the MnO_2 and RO sub-lattices and may be described by the tolerance factor $f = (\langle r_A \rangle + r_O)/[\sqrt{2}(r_{Mn} + r_O)]$, where $\langle r_A \rangle$, r_{Mn} and r_O are averaged ionic radii of the elements. In $R_{0.5}Ba_{0.5}MnO_3$, the f is in the range from 1.026 (La/Ba) to 0.995 (Y/Ba), and the closest to 1 is f (Nd). In a vicinity of f = 1 ferromagnetic ordering by the double-exchange interaction becomes dominant, and in the lower range of f values the CO states become more stable.

$NdBaMn_2O_6$ has the lowest level of internal strain, a high Curie temperature (300 K), and a relatively small magnetic moment – about 0.7 μ_B/cell. In the disordered phase of (NdBa)MnO_3 a magnetic transition was observed at 120-160 K, but the magnetic

moment is much higher – up to 3.0 μ_B/cell, and at temperatures below 50 K a magnetic glass-like behavior was registered.

In a paper [46] electromagnetic properties of $R_{0.6}Ba_{0.4}MbO_3$ (R = La, Pr, Nd, Gd) thin films were investigated. So far this is the only publication on $Nd_{1-x}Ba_xMnO_3$ films we could find in the literature. The films were produced by MOCVD (chemical vapour deposition), 300-400 nm thick. Great attention was paid to the magnetic properties of the films; the obtained results give an evidence of a two-phase state of the films, where FM and AFM phases are comparable in volume. This work provides us with a valuable piece of information on $R_{1-x}Ba_xMnO_3$ thin films, for the later comparison with films produced by physical methods.

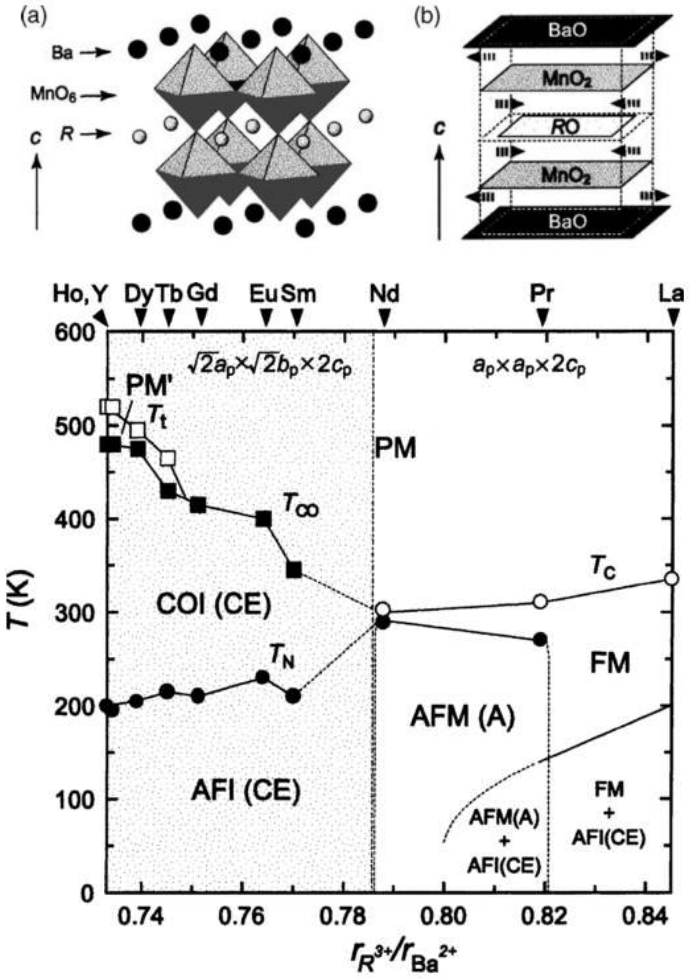

Figure 4.3. Crystal structure and structural concept, phase diagram of the A-site ordered manganate $RBaMn_2O_6$ family.

For our investigation a $Nd_{0.67}Ba_{0.33}MnO_3$ manganate composition was used. It supports Nd-Ba cation ordering with segregation of non-ferromagnetic NMO oxide. At the same time, at the optimized conditions it should be possible to get the disordered cubic phase as well. Besides that, 0.33 doping level provides optimal ferromagnetic properties in the well-studied $(LaSr)MnO_3$, $(LaCa)MnO_3$.

4.4 Cuprate-manganate heterostructures.

One of the most interesting areas of applications of cuprate-manganate heterostructures is the injection of spin-polarized carriers into the superconductor. Due to the half-metallic behavior of CMR compounds they may act as a source of spin-polarized carriers [26]. Such an injection leads to a strong suppression of superconducting order and may thereby be utilized as an active element for superconducting switching devices, promising larger changes in the supercurrent in comparison with unpolarized carriers injection from a normal metal.

The study of cuprate-manganate heterostructures is also important for fundamental science. It may provide some information on the electronic band structure of the normal and superconducting states of the superconducting layers, which would be valuable for the understanding of the interlayer magnetic coupling through an oxide superconductor. For conventional metals and metallic superconductors the Ruderman-Kittel-Kasuya-Yosida (RKKY) interaction model may be employed, but the situation is very different for cuprate-manganate multilayers. The electronic properties of cuprates are different even in the normal state, and furthermore, in the superconducting state an anisotropic order parameter and gap are involved. It is not clear whether the RKKY interaction is relevant or not for such a case. Manganates also differ from metallic ferromagnetic materials. The competition of superconducting and ferromagnetic order in the interlayer areas makes the picture even more complex, involving ferromagnetic-superconducting proximity effects.

At the same time with the considerable interest for the cuprate-manganate heterostructures, there is a number of issues that make this area difficult for accurate experiments with clear results. As was already mentioned in the beginning of this chapter, the problem of mutual interdiffusion, and, as a consequence, “dead” layer formation may play a significant role. Strain induced by lattice constants mismatch may affect the properties of the manganate layer. The interface roughness is also an important parameter to minimize; this requirement is much harder to fulfill, as opposed to metallic superconductor-ferromagnetic structures.

5 Fabrication of samples

5.1 ReBCO thin films deposition, general aspects in the context of pulsed laser deposition (PLD)

A number of very different deposition methods may be used for ReBCO thin film fabrication. Physical methods, while being slow layer-by-layer deposition techniques, in general are bad choices for coated conductors production. But for investigation purposes, where small samples are sufficient, these methods are beneficial - due to a more flexible routine it is possible to tune many deposition parameters independently, and precise control of them allow to achieve reproducible results of a high quality. The most commonly used techniques are molecular beam epitaxy (MBE), different sputtering methods (RF, cathode, magnetron) and laser ablation (or pulsed laser deposition, PLD). MBE has more strict and complex requirements for the equipment and, while providing the best control of the stoichiometry of the material, is less often utilized for ReBCO films fabrication due to low deposition rates.

In general, all the methods consist of three main steps:

1) sputtering of the material to be deposited;
2) material transport to the surface of the substrate;
3) formation of the film.

There are different parameters which have to be controlled at each step. From now on focus will be on PLD specific details, while most of the problems are common for all physical methods.

The sputtering of the material during the laser ablation is performed by focused laser light. The irradiated surface layer of a solid target is almost instantly ablated (transformed from the solid to the plasma phase), if the power density is sufficiently high. This limit is material-specific and ranging from 10^7 to 10^9 W/cm^2. Such power densities (intensities) can be obtained by use of high power pulsed lasers with energies exceeding 100 mJ per pulse and pulse duration about 5-100 nanoseconds. Typically

used lasers are in the near UV range (190–300 nm), since most of materials are not transparent at these wavelengths (while MgO, for example, is transparent). A complete absorption of the pulse energy by the surface layer of the target and the very high intensities utilized lead to the instant sputtering of ablated material with only modest heating of the surroundings of the laser spot. The amount of ablated material does not depend on the actual energy density – as far as it is above the so-called ablation threshold, the plasma of ablated material is screening the target surface, and the excess energy is spent on heating the plasma cloud.

The subsequent transport of the material to the substrate for the growing film is a result of pseudo-adiabatic expansion of this plasma cloud, with a preferential direction normal to the target surface. The higher the starting temperature, the more narrow is the plume of ablated material. Furthermore, in the presence of a background gas both elastic scattering and reactive interactions affect the spreading of ablated material.

During the next stage the incoming atoms are adsorbed on the substrate surface. The adsorbed atoms may re-evaporate or diffuse on the surface, colliding and nucleating into clusters. Small clusters may dissociate, but above a certain critical size they become stable. The higher the substrate temperature, the larger the critical size. At the same time, a higher substrate temperature increases the re-evaporation probability, and therefore slows down the growth rate. Big, stable clusters continue the growth until a complete coverage is reached. These macro-clusters become grains of a polycrystalline film, or just form an amorphous film, depending on the deposition conditions.

To promote epitaxial film growth it is necessary to have a single crystal substrate of a lattice constant matching the film orientation to be grown. The substrate smoothness is usually achieved by chemical-mechanical polishing. The substrate should be inert to the growing material, be stable at deposition temperatures and have close thermal expansion coefficients.

For multi-element compounds, and, particularly, for ReBCO films, the questions of stoichiometry and phase stability have to be considered. The correct stoichiometry composition of incoming material is necessary for crystallization of epitaxial, high

quality *c*-oriented ReBCO films with no additional phases. This is the reason why for PLD of ReBCO, ceramic polycrystalline targets sintered with a stoichiometric composition are in use. Another critical aspect is the density of the target – in the presence of pores the laser irradiation may hit underlying layers of the target through them, leading to an explosive emission of micrometer size particles. These particles melt down during their flight and condense on the surface of the substrate as droplets. This problem can be minimized by use of single crystal targets or high-density polycrystalline targets (more than 90% of single crystal density).

While the ablation itself is not element-selective and provides an exact transfer of element composition of the target into the plasma cloud, the subsequent expansion in a background gas mixture is different for various elements. Typically the working gases are argon (Ar, 39.5 A_r) and molecular oxygen (O_2, 32 A_r). The strongest elastic scattering should be for atoms of a similar atomic weight, in the YBCO (Y - 89 A_r, Ba – 137.3 A_r, Cu – 63.5 A_r) case it should be copper. But inelastic reactive scattering of Ba on O_2 molecules completely changes this picture, making it the most widely scattered element of these three. A typical element composition in the substrate plane as a function of off-axis position is given in Figure 5.1 [47,48]. The stoichiometric composition (±5%) is achieved within a 5-10 mm radius ring around the center. Moreover, this distribution depends on the oxygen partial pressure, the total pressure, the energy density on the target (even slightly on pulse duration), the laser spot size and shape, and the target-substrate distance. The problem may be overcome by scanning the beam over a certain target area, providing an average element composition very close to the stoichiometric. This also prevents the potential melting of the target surface.

With the right choice of single crystal substrate (providing close match of lattice constants), close to stoichiometric depositing material, and thermodynamic parameters (substrate temperature and oxygen partial pressure) in the stability region (Figure 3.7) close to the decomposition line it is possible to produce epitaxial ReBCO films. Due to the fact that the lattice constant *c* is nearly equal to three times the lattice constant *a*, the probabilities of growth of both *a* and *c* orientations are sizeable, when the substrate has

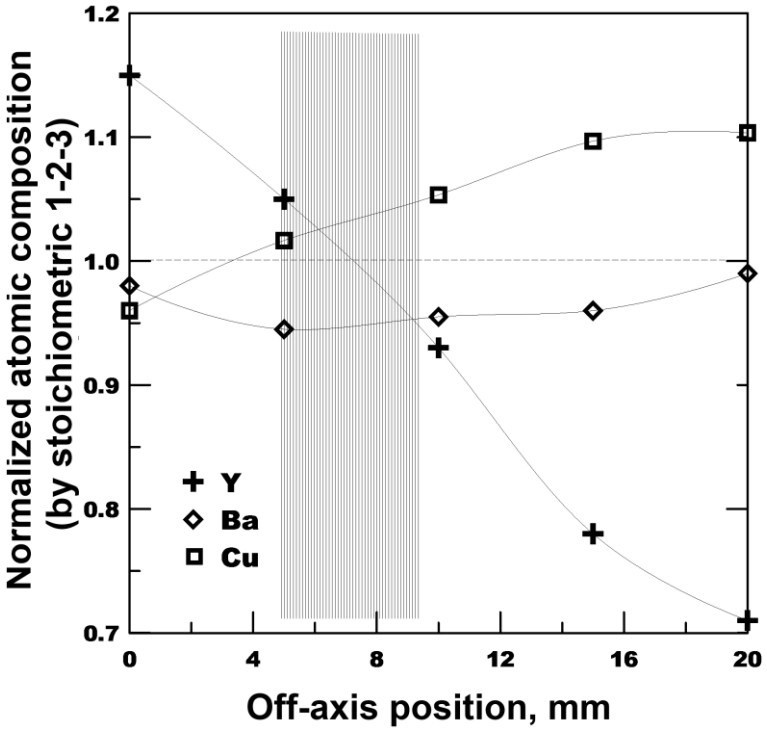

Figure 5.1. Normalized element composition of YBCO films, deposited by PLD on different off-axis positions, at 1 mbar O_2 pressure, 50 mm target-substrate distance. 1 represents stoichiometric values.

a good match in lattice constants with both orientations. This often leads to formation of films with both orientations. Due to the large anisotropy of ReBCO films, *a*-oriented films have suppressed superconducting properties. Fortunately, the deposition temperature affects the probability of *c*-orientation growth: at temperatures above 700 °C the deposited films are mainly *c*-oriented (high temperature shifts the balance to the thermodynamically preferable *c*-orientation). At the same time, the possible chemical interactions with the substrate at the elevated temperatures should be controlled.

The last important parameter of the PLD process, which is important for the film quality, is the laser repetition rate, which is directly ruling the deposition speed. For high quality film formation a quasi-thermodynamic regime of film growth rather than a kinetic one is essential. Since the thermodynamic parameters of the process are determined by other requirements, the maximum deposition speed of the quasi-thermodynamic process is limited by the relaxation time of the adsorbed material. It is worth mentioning that due to the pulsed mode of deposition the process can not be considered as purely thermodynamic.

Due to the similar perovskite crystal structure pulsed laser deposition of the manganate films has the same problems and solutions as the superconducting cuprates. Summarizing, PLD is a very complex process with many parameters to be optimized, which surely are not completely independent: these are laser pulse energy and spot size, repetition rate, scanning speed and scan size, total pressure and oxygen partial pressure, target-substrate distance and substrate temperature.

5.2 The deposition setup

A schematic representation of the PLD setup is given in Figure 5.2 and Figure 5.3.
An excimer laser Coherent COMPexPro 205 (1) filled with KrF as active medium is utilized as the source of radiation. The irradiation parameters are: the main wavelength λ = 248 nm, the maximum energy E_{max} = 700 mJ and the pulse duration τ = 25 ns. In order to get a homogeneous energy distribution across the spot, the central part of the laser beam is cut by a rectangular diaphragm (2), also providing a square beam spot on the target. One of two mirrors, which are guiding the laser beam towards to the chamber (7), is mounted on a two-axis motorized mount (3). This is used for XY meander-shaped scanning across the target while running the laser with a constant repetition rate. This method of ablation has several significant benefits: (i) compensation of element composition deviations, (ii) more even target use, (iii) good control of potential melting of the surface, by varying the scanning speed (in comparison with a rotating target design, the laser less often fires on the same area, and only in-line overlapping has to be taken into account). Before the entering the vacuum chamber through a quartz window (6) (quartz is transparent for UV-light) the laser beam is focused by a spherical lens of 300 mm focal length (5), in order to reach the necessary energy density (of 1-2 J/cm^2). The center of the target is situated in the image plane of the lens. The spot size may be measured directly on the target after deposition, and, while varying from close to far ends of the target, in average is about 2.5x2.5 mm^2 (the variation is about 10%). Since the quartz window may become contaminated by some ablated material, the pulse energy inside the chamber has to be measured before each deposition.

The four-position target holder (8) allows us to fabricate multi-layers of different materials *in-situ*. It has water cooling inside of the stage, which is helpful for long depositions. With a manually operated shutter (9) it is possible to make pre-ablation right before the deposition.

The substrate heating plate (11) is made of Inconel steel, which is sustainable at high temperatures in the chemically active background gas of oxygen and which has a high thermal conductivity. It is heated by a halogen lamp through a light guide made of quartz (12); the power supply is controlled by a Eurotherm PID controller (13). With a soldered Pt-Pt/Rh thermocouple and proper thermal insulation this small pellet provides a reliable and sensitive control of the substrate temperature. The substrates are mounted on the heating plate by silver paint with a reproducible baking procedure, which is providing good thermal contact between the substrate and the heating plate. The size of the pellet and the homogeneity of the deposition allow fabrication of a 10x10 mm^2 area or up to four 5x5 mm^2 samples a time.

The process gas mixture is supplied by two mass flow controllers (14) operated by a control unit (MKS corp.) (15). Two gases are supplied, Ar and O_2. The use of the argon is motivated by the need to control two different functions of the background gas, i.e. a scattering medium and an oxygenation environment, independently. The typically used total flow is 5-10 sccm. The pressure in the chamber is controlled by a down-stream regulating valve (19) using a capacitance manometer (23), which can operate at pressures below 1 torr (1.33 mbar).

The two-stage pumping system consists of a diffusion pump with a LN_2 filled cold trap and a forevacuum mechanical pump and has a base pressure of 10^{-9} bar, providing sufficiently clean environment for epitaxial film fabrication.

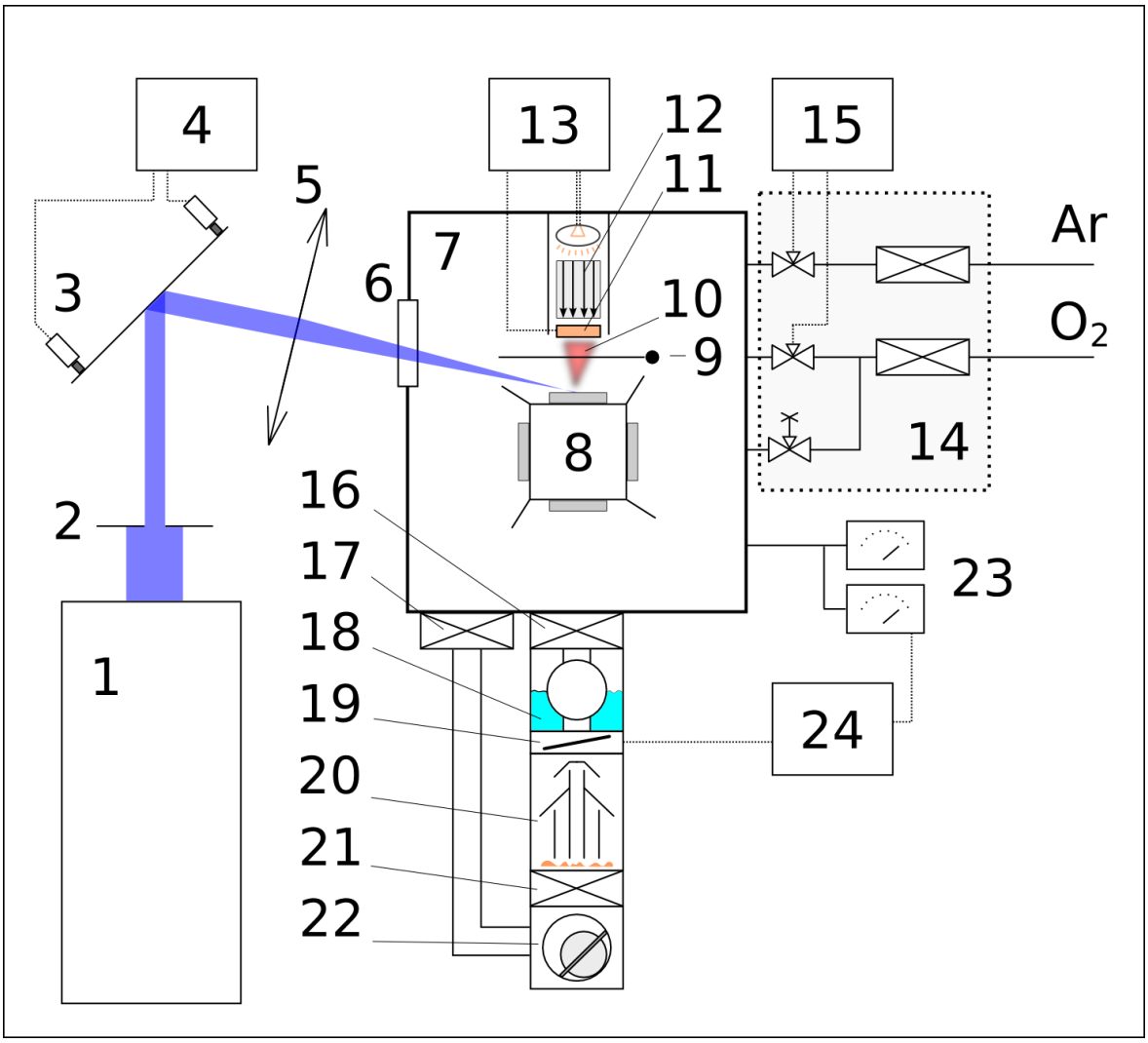

Figure 5.2. The PLD setup.

Optical system: 1)Coherent COMPexPro 205 KrF excimer laser, □ = 248 nm, Emax = 700 mJ, □ = 25 ns; 2) diaphragm; 3)Zaber T-MM2 motorized mirror; 4)scanner control (PC); 5)lens; 6)quartz window.

Chamber: 7)vacuum chamber; 8)four-position water-cooled target holder; 9)shutter; 10)plume of ablated material; 11)substrate heating plate; 12)heater: halogen lamp with quartz rod as a light guide; 13)Eurotherm PID controller;

Gas system: 14)process gases subsystem (Ar, O2 mass flow controllers, manual inlet valve), 15)MKS controller;

Pumping system: 16)baffle valve; 17)roughing valve; 18)cold trap; 19)regulation valve; 20) diffusion pump; 21)backing valve; 22)roughing pump; 23)capacitance manometer; 24)pressure controller.

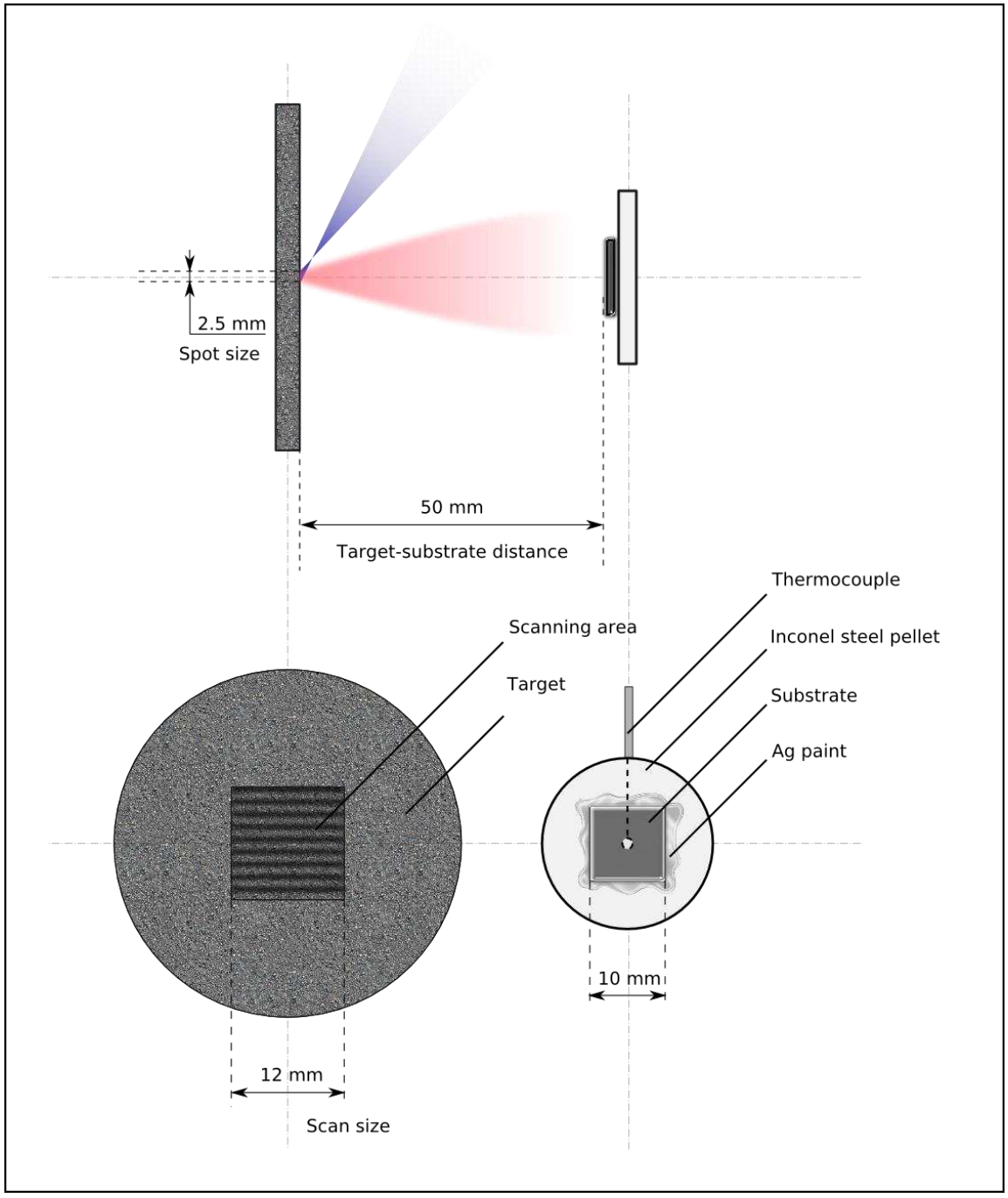

Figure 5.3. Geometry of the deposition process. A focused laser beam is scanning over the target surface with a meander trajectory, covering 12x12 mm^2 area. This procedure allows us to neglect the off-axis changes in composition, due to an effective averaging (the variation in is less than 2%). The substrate heating plate is a 20 mm diameter, 5 mm thick metallic pellet (Inconel steel) with a soldered Pt-Pt/Rh thermocouple. It is mounted on ceramic sticks, which provide a negligible heat sink to the chamber, and receives light from a halogen lamp from the back side (through a quartz light guide). Substrates are glued with a silver paint on the front polished side of the pellet. The substrate may reach up to 850 °C (limited by the power supply).

5.3 Characterization methods

Magnetic properties

The superconducting properties of the samples were examined by fast and easily available AC-susceptibility measurements on a home-made setup (T_c determination, with the transition width as an additional information), and externally with a VSM magnetometer (cryogenic magnetization measurements) by Niels Hessel Andersen at Risø DTU (Denmark). The magnetic properties of NBMO films were investigated with a SQUID magnetometer from Quantum Design (Magnetic Property Measurement System) by Vitaliy V. Yurchenko at University of Wollongong (Australia), and Oleksandr Stupakov at Institute of Physics of the AS CR (Czech Republic).

Crystal structure and morphology

The structural parameters were determined by X-ray diffraction (XRD) measurements in Bragg geometry using an X'Pert PRO two-axis diffractometer with a CuK_α radiation source at DTU CEN.

The surface morphology of the films was observed with atomic force microscopy (AFM) using a Nanosurf EasyScan microscope, and a Philips scanning electron microscope (SEM) at DTU Nanotech.

Chemical composition

The elemental composition of the films was studied using an EDAX analysis attachment to the SEM and inductively coupled plasma (ICP) analysis based on quantitative optical emission spectroscopy by Risø DTU.

6 Improvement of the critical current density of YBCO films

In this chapter the results of our studies of APC formation by decoration of the substrate with yttria before deposition, by direct change of target element composition and by combination of these methods are reported.

All the YBCO films were fabricated at the deposition conditions optimized for formation of high crystal quality and high critical temperature thin YBCO films on $LaAlO_3/SrTiO_3$ perovskite substrates (substrate temperature 770 ˚C, 0.8 mbar total pressure, Ar/O_2 flow ratio 8/2, laser energy density on target 1.5 J/cm^2, repetition rate 2 Hz, deposition rate 0.165 nm/s, post-deposition oxygenation in 500 mbar O_2 at 450 ˚C for 1 hour). Both yttria and YBCO layers were ablated from commercially available high-density targets (MTI Corp.).

The films were deposited on (100) $(LaAlO_3)_{0.3}$-$(Sr_2AlTaO_8)_{0.7}$ (LSAT) perovskite substrates. These substrates provide excellent conditions for YBCO growth: lattice constant with a small mismatch (3.867 Å, less than 0.3% mismatch with the (*ab*) plane of YBCO), close coefficients of thermal expansion, no twinning or lattice phase transitions in the deposition temperature range. (001) $SrTiO_3$ (STO) and (110) $NdGaO_3$ (NGO) perovskite substrates were used as reference samples. We note that the temperature of the film growing on NGO substrate is 20-25 ˚C lower than that on LSAT or STO due to the IR transparency of the NGO substrate, so when deposition on these substrates was done simultaneously, the film on NGO grew in non-optimal conditions, especially during the early stages of growth.

6.1 YBCO films on yttria layers

6.1.1 Deposition of yttria seeding layer

As was reported in the literature [15] decoration of the substrate with Y_2O_3 nanoparticles promote formation of dislocations in the YBCO film. Under certain conditions (excess of Y during the deposition) we may also expect segregation of yttria on top of the nanoparticles of the seeding layer.

For formation of yttria nanoparticles on the substrate surface the PLD may be employed in three possible ways:

- Droplets of the molten target surface,
- Aggregation of the deposited material on the substrate surface,
- Condensation of ablated material during travel from target to substrate.

The first method produces too big particles (of 100-3000 nm size) and cannot be used for the formation of APCs. The second method is good for metallic particles on oxide or non-metal substrates, but it does not work well for our combination of deposited material and substrate, due to the relatively high mutual sticking coefficients for oxides. Condensation from the gas phase is the most commonly used method for fabrication of nanoparticles by laser ablation. In general, the process is a competition between the cooling of the expanding plasma, and the decreasing density of ablated material. When the temperature of the material decreases to the condensation point the density should be high enough for the formation of nanoparticles.

All the deposition parameters influence the growth of the nanoparticles. We fabricated a set of Y_2O_3 thin layers, where the effects of substrate temperature, total background pressure, oxygen partial pressure and energy density on the target were studied.

All the deposited films were composed of a uniform yttria film (due to direct condensation on the substrate surface) and nanoparticles embedded into it. A series of depositions revealed significant difference of the film properties originating from the pre-history of the target. This effect can be explained by a surface modification of the target during the laser ablation. The Y_2O_3 target might get the surface layers depleted with oxygen; as a result the ablation threshold decreases from 1.3 J/cm^2 for yttria to just 0.9 J/cm^2 for yttrium [49], the temperature of the ablated material increases and the balance between the temperature and the density of the plume which is needed for nanoparticles formation is destroyed.

A freshly polished target gives results close to an initial one, thus we can operate with a polished target of, presumably, yttria, or get a metallized surface (yttrium) of the target by a pre-ablation procedure.

The best results were obtained at 800 ºC, 0.2 mbar, pure Ar, 1.1 J/cm^2. Dense (4×10^9 cm^{-2}) *c*-oriented nanoparticles of a 50-80 nm diameter and 20-45 nm height were observed by AFM.

Temperature effect

No significant changes can be seen when the temperature is decreased from 800 to 700 or 600 ºC. A decrease of the substrate temperature to room temperature results in the formation of very dense and small particles, but they can hardly be observed using AFM: the particles are not bound to the substrate surface and are easily moved by the AFM tip. No preferential orientation is seen on the XRD scans for the room-temperature deposited film.

Effect of pressure

The pressure during the deposition strongly affects particle density and size (see Figure 6.2 and Figure 6.1). The size of the particles increases with pressure due to the longer flight time and, hence, longer growth time. The density of particles decreases with particle size, while an optimal pressure is about 0.1-0.2 mbar (this pressure range allows to obtain the smallest particles with a high density).

Effect of oxygen

The effect of oxygen addition into the working atmosphere may be illustrated by AFM micrographs in Figure 6.2a, b: the particles become more round (Figure 6.1b) while in pure argon they clearly show facets. This effect was observed with other materials also [50]. No effect of oxygen addition on particle size could be detected, while a small decrease of the size in pure argon was expected.

Laser fluence effect

An increase of the energy density on the target surface (from 1.1 J/cm^2 to 1.5 J/cm^2) results in a decrease of the particle density and an increase of the particle size. The overheated plume travels faster, so a greater part of the ablated material comes to the

substrate before it condenses into nanoparticles; but the seeds are growing faster also, resulting in bigger particles.

Structural properties

All films of a preferable orientation showed the same (001) orientation and lattice constant in a narrow range 10.608 – 10.618 Å (very close to the bulk value of 10.605 Å). The presence of two peaks (004) and (008) allows an evaluation of strain and thickness of the oriented part of the film [51]. The strain usually was 0.5 – 0.8%, increasing to 1.24% for the sample deposited at high laser fluence and decreasing to 0.2% for the sample deposited at low pressure; for the samples deposited one after another the strain increased with an increase of nanoparticle density.

In conclusion, we investigated different growth conditions of yttria nanoparticles. Our AFM equipment does not allow us to observe nanoparticles of less than 10 nm in diameter. For moderate particles sizes (tens of nanometers) optimal conditions were found. An effect of target modification should be taken into account (substitution of the yttria target by metallic yttrium is probably a proper solution in order to achieve a reproducible process).

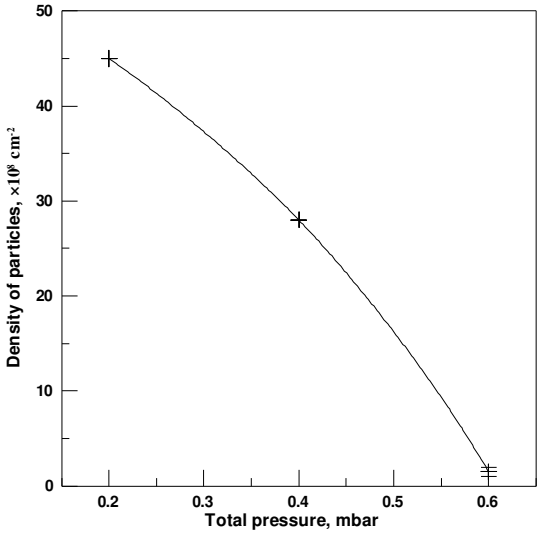

Figure 6.1. Density of yttria nanoparticles vs total pressure (oxygen part 0-6%).

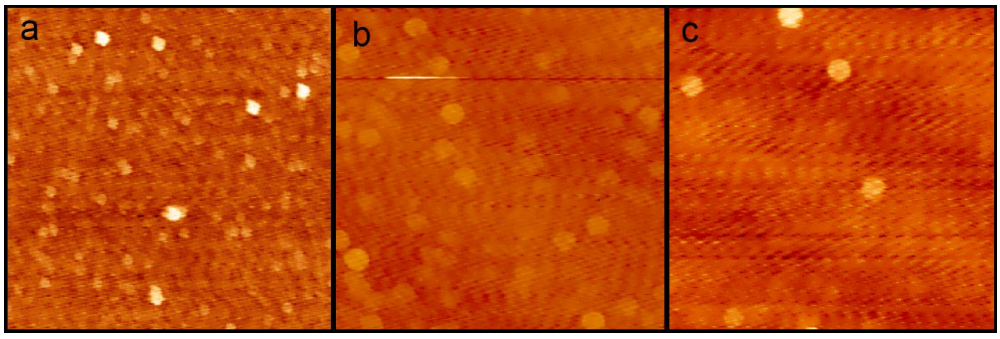

Figure 6.2. AFM micrographs (2x2 μm^2) of yttria layers on LSAT substrates. Laser fluence 1.1 J/cm^2, pressure, from left to right: 0.2 mbar (Ar), 0.4 mbar (Ar/O_2), 0.6 mbar (Ar)

6.1.2 YBCO films depositions on yttria decorated substrates

YBCO films were deposited in one cycle on two different yttria nano-layers on LSAT substrate and on a bare LSAT substrate as a reference. A stoichiometric $Y_1Ba_2Cu_3O_{7-x}$ target was utilized. Two different kinds of yttria layers were fabricated using metallized pre-ablated (HLP25) and virgin fresh-polished (HLP29) target surface, resulting in a uniform "seeding" layer (YO_x) and "template" layer (Y_2O_3) of individual nanoparticles, respectively. Both layers are oriented (only (100) orientation peaks can be distinguished on the XRD θ/2θ-scans), with the lattice constants equal to 11.609 Å (close to the bulk value of 11.605 Å). Nominal thicknesses are 0.9-0.8 nm, based on a crystallite thickness estimation from the XRD data and a deposition rate calibration.

Morphology and crystal structure

The estimated thickness of the YBCO films is 240 nm. The morphology of the fabricated samples was investigated by AFM (Figure 6.3). The structure of the main part of the film is similar for all the samples: *c*-oriented YBCO grains with an average size of 0.3 μm form a dense film with shallow (~10 nm deep) pores at the points where several grains are connecting to each other. Large (up to 1 μm long) and high (more than 100 nm high) elongated particles of unclear nature are present on the surface of the films deposited on yttria layers, with densities $\geq 10^7$ cm^{-2}. These particles are oriented along two orthogonal directions on the film surfaces. This kind of growth is typical for *a*-oriented particles, but this assumption is not proved by the XRD measurements, since no diffraction peaks from *a*-oriented phase have been found for the YBCO film on the template layer (Figure 6.5). A weak peak of *a*-oriented YBCO is observed only for the film on the seeding YO_x layer (top curve, Figure 6.5), and it probably corresponds to the small (height less than 50 nm, typical length about 150 nm) elongated particles on the film surface (Figure 6.3, HLP25), which are numerous on the surface of this sample, but rare on AFM micrographs of other films.

A clear splitting of the $K_{\alpha1}/K_{\alpha2}$ peaks observed by XRD indicates a higher quality of the crystal structure of the films which were grown on yttria layers, as compared to the

YBCO film on a bare LSAT substrate, where no splitting can be seen. The strain evaluation gives $\delta d/d = 0.5\%$ for the sample on a bare LSAT substrate, and even lower values for the films on yttria layers; nearly the same *c* lattice constant was measured for all the three films (11.673 ±0.005 Å).

Superconducting properties

The results of AC-susceptibility measurements of these three samples are given in Figure 6.4. While all the films have very high superconducting transition temperature (T_c = 91.4-91.8 K), the reference sample on a bare substrate has the lowest T_c and the widest superconducting transition of all three.

The critical current density data were extracted from magnetization measurements performed in a wide range of magnetic fields and temperatures. The YBCO films on the yttria seeding layers show significant improvement of the critical current density at high magnetic fields, comparing with the film on a bare substrate (Figure 6.6). At 77 K, the critical current density of YBCO films on the yttria layers exceeds that of the standard film for all magnetic fields over 0.3 T; in the 3-4 T field range the J_c values of the films on yttria layers are respectively, 3 (HLP29, nanoparticles) and 10 (HLP25, uniform yttria layer) times higher than the corresponding values for the standard film. The YBCO film on the uniform yttria layer has the highest J_c at 77 K, presumably due to higher defect density. However, at lower temperatures the behavior is opposite, and the film on the yttria nanoparticles template layer exhibits the highest critical current density.

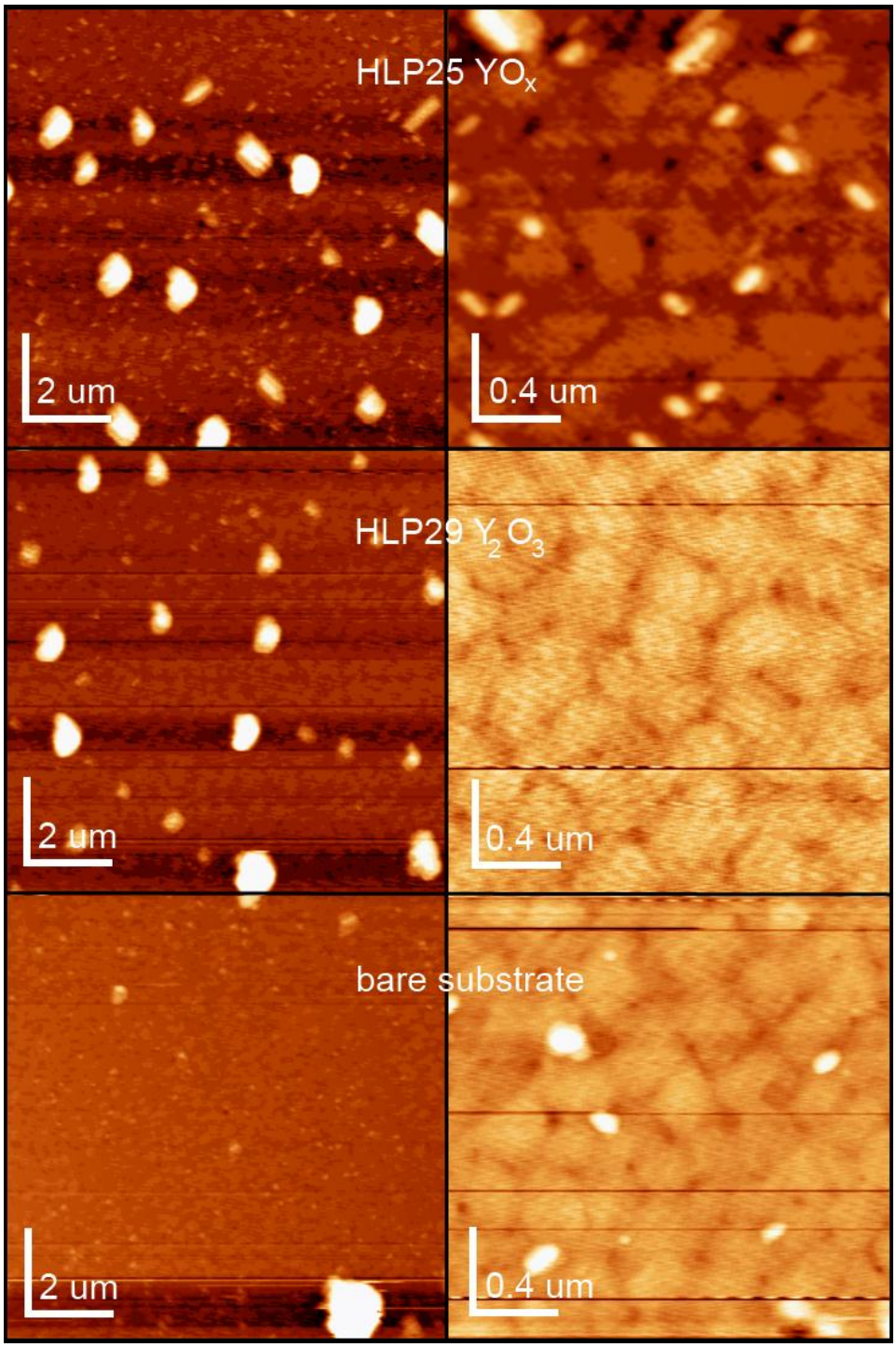

Figure 6.3. AFM micrographs of YBCO films deposited from a stoichiometric target on two kinds of yttria decoration on LSAT (100) and on a bare LSAT substrate. Vertical scale 100 nm for all scans.

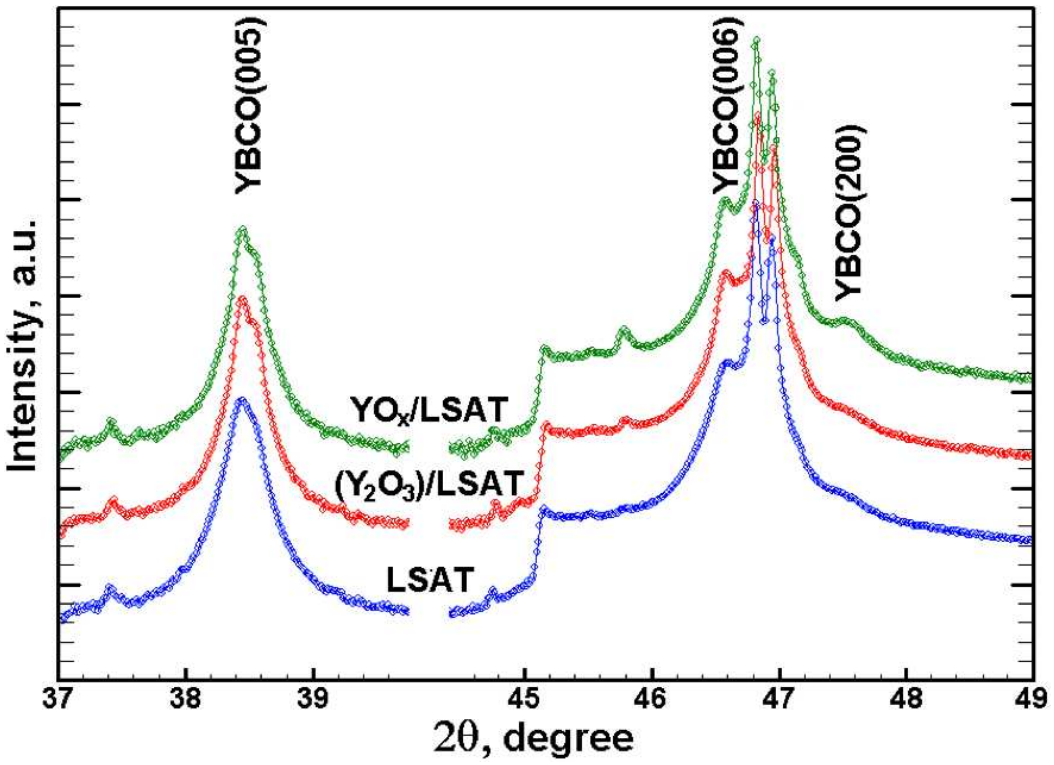

Figure 6.5. Fragments of XRD θ/2θ-scans of the YBCO films deposited on LSAT (100) substrates with two kinds of yttria decoration and on a bare substrate. Bottom curve: bare LSAT substrate; middle curve: template yttria layer of nanoparticles over LSAT substrate; top curve: uniform yttria seeding layer over LSAT substrate. Left: YBCO (005) peak. Splitting of the XRD peaks for the YBCO films over yttria layers indicates higher crystal quality of these films compared with the films on bare substrates. Right: a-oriented peaks are present for the YBCO film on yttria seeding layer.

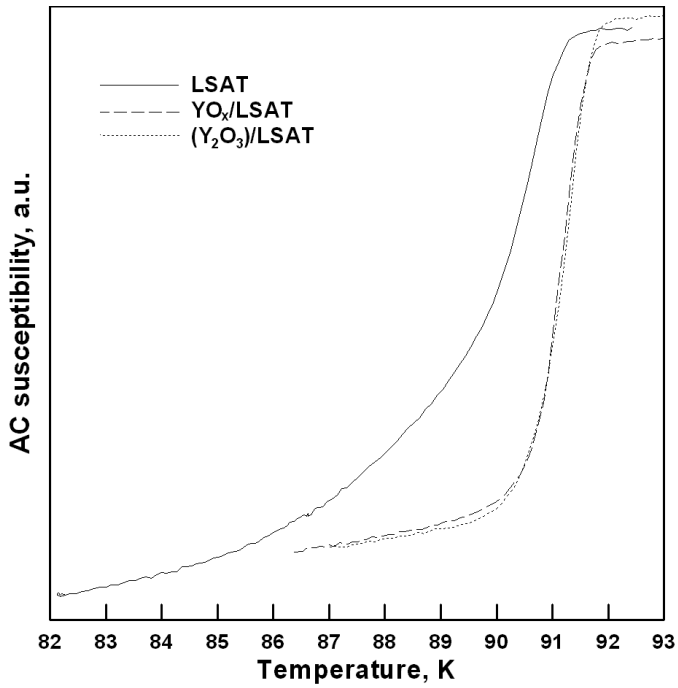

Figure 6.4. AC susceptibility curves for YBCO films deposited from a stoichiometric target on LSAT (100) substrates with yttria decoration and on a bare substrate. Solid line: bare LSAT substrate; dashed line: uniform yttria layer on LSAT substrate from "metallized" surface of yttria target; dotted line: template yttria layer of nanoparicles on LSAT substrate.

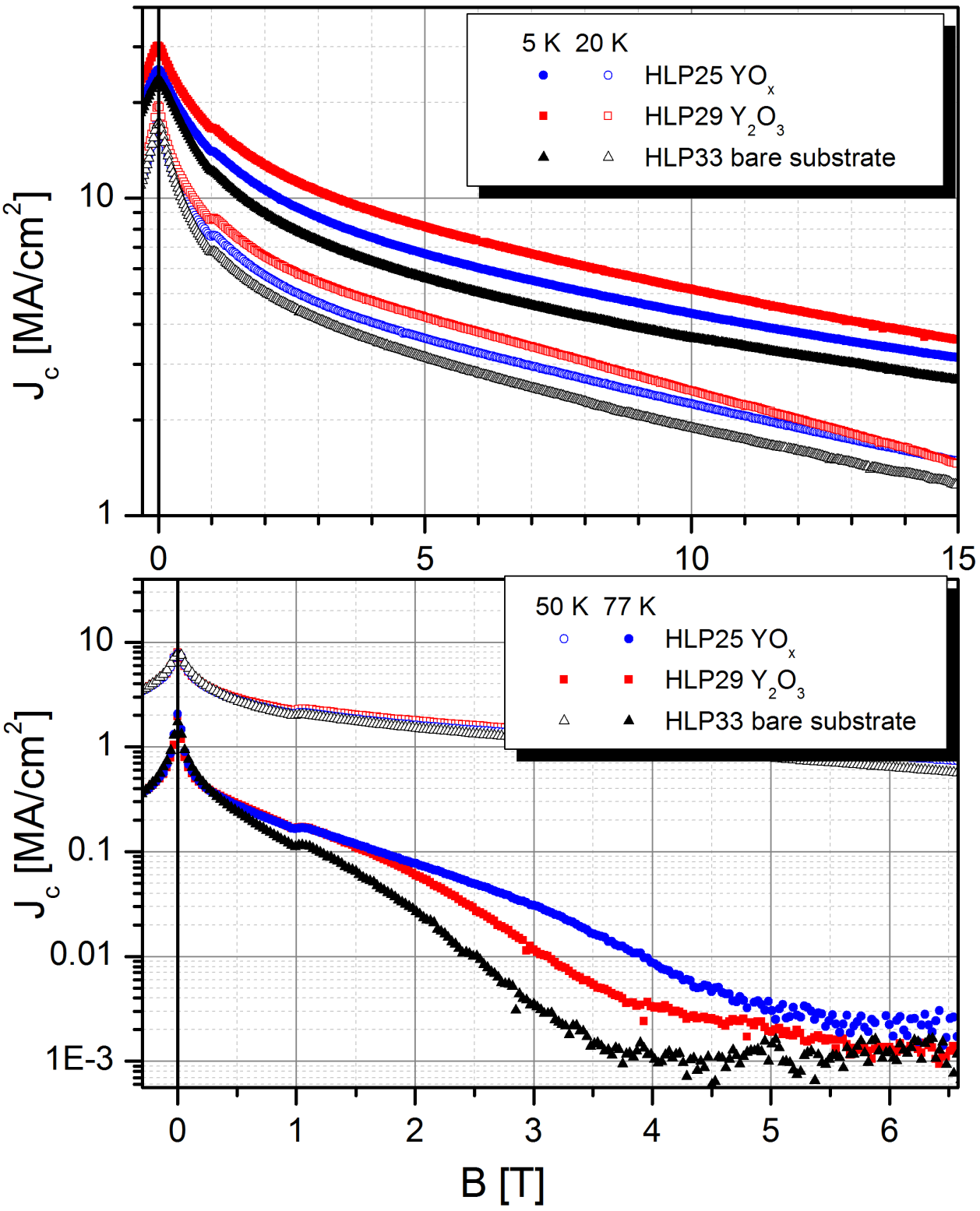

Figure 6.6. Critical current density vs magnetic field curves for YBCO films deposited from a stoichiometric target on LSAT (100) substrates with yttria decoration and on a bare substrate. Black triangle: bare LSAT substrate; blue circles: uniform yttria layer on LSAT substrate from "metallized" surface of yttria target; red squares: template yttria layer of nanoparicles on LSAT substrate. Upper plot: open symbols for 20 K, filled for 5 K. Bottom plot: open symbols for 77 K, filled for 50 K.

6.2 Y-doped Films

6.2.1 A study of element composition

As was discussed in chapter 5, the transfer of ablated material to the surface of growing film is dependent on the deposition parameters and the resulting film composition might be quite different from the composition of the target. For the given deposition conditions (mentioned in the beginning of this chapter) we performed a study of composition transfer using several targets of different element content.

ICP (inductively coupled plasma analysis based on quantitative optical emission spectroscopy) and EDAX (energy-dispersive X-ray spectroscopy) methods were employed for this study. The first method is destructive, non-local, complicated and could not be done using available equipment, so it had to be done externally. The sample of interest is dissolved in acid and the composition of the sample can be analyzed by means of a calibrated spectroscopic method. From another point of view, it is a direct method of composition measurement and thus allows reaching an acceptable accuracy level (typically ±1%, relatively, for 100 μg material). In contrast, EDAX is performed on a SEM (scanning electron microscope) and may provide valuable information on the local composition, but for the thin film geometry the accuracy of this

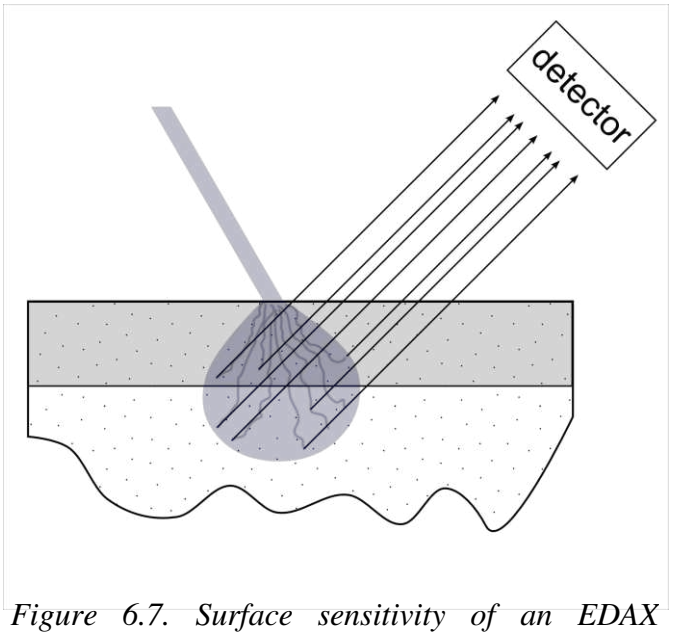

Figure 6.7. Surface sensitivity of an EDAX method is determined by scattering cross section of electrons of the electron beam. Electrons scatter elastically distributing through a cone under the beam spot, inelastically inducing excitations of atoms of the material. The energy of the beam determines the balance between two scattering mechanisms, making the cone deeper and narrower with increasing beam energy.
The depth of propagation of the electrons determines the film fraction of the spectra, the width is responsible for the spatial resolution.

method is rather limited, see Figure 6.7. For a quantitative analysis a calibration of this method by direct measurement (i.e. ICP, in our study) is necessary, since for each chosen accelerating voltage (i.e. beam energy) the cross section for the atom excitation is different and element dependent.

The use of LSAT substrates leads to an overlapping (and subsequent deconvolution) of the X-ray spectral peaks of substrate and film elements. Thus, for the EDAX measurements reference samples deposited on NGO substrates were used. The morphology and crystal structure of the samples deposited on these two substrates were similar, thus we consider the extrapolation of EDAX results to the samples on LSAT substrates to be correct.

For the calibration of the EDAX measurements we fabricated relatively thick (480 nm) samples using three targets of different composition. Two low-density targets (Ba-rich $YBa_{2.3}Cu_3O_x$ and Cu-deficient $YBa_2Cu_{2.85}O_x$) were combined with a commercially available high-density stoichiometric $YBa_2Cu_3O_x$ target. XRD spectra, AFM, SEM scans and EDAX spectra of different areas of the films (in particular, clean film areas, film grains, particles, droplets on the surface, pores) were taken before dissolving the samples in acid for the ICP measurements. In addition to these three samples, the composition of the stoichiometric target was examined by ICP analysis, in order to prove the reliability of the method. The results of the target measurement are in agreement with the nominal Y/Ba/Cu = 1/2/3 element ratio (the difference is less than 1% for each element). Compositions of the targets and the results of the measurements are summarized in Table 6.1.

All three films are Ba-rich, with almost the same relative contents of Ba. As the heaviest element, Ba is least scattered by the Ar/O_2 atmosphere with a dominant fraction of Ar (while inelastic scattering on oxygen is the strongest for Ba, and films grown in pure oxygen are Ba-deficient [52]).

The Ba content of the films is clearly limited by a certain factor, and it does not depend directly on the Ba content of the target. Instead, the excess of Ba in the film seems to be linked to an additional Y content.

According to the ICP results, the highest Ba content is found in the sample deposited from the Cu-deficient target, where the amount of Y is maximal, while the film deposited from the Ba-rich target (and the smallest part of Y) has the lowest Ba content. The film composition dependence on Y content of the target is represented in Figure 6.9. This behavior may be explained by re-evaporation of the Ba, which is not bound to some yttrium-based oxide. Such a mechanism could be an effective limiting factor for the concentration of Ba in the growing film.

The calibration of the EDAX method by these ICP results was performed using the least squares technique (for normalization of the data of different samples). The resulting numbers (Table 6.1) are in a generally good correlation with the original ICP data, so the EDAX can be further used for investigation of new samples and for quantitative analysis of different film areas. The difference between these data sets is probably related to a non-uniform distribution of elements through the film thickness, with a higher concentration of excess material on the surface of the growing film. The electrons of the SEM beam are passing this thin layer with the highest energy and with the least probability of interaction, thus the contribution from the surface layer of the film is somewhat suppressed in the EDAX results.

For the fabrication of Y-rich films we utilized high-density commercially available targets of $Y_{1.25}Ba_2Cu_3O_x$ and $Y_{1.5}Ba_2Cu_3O_x$ nominal compositions (MTI Corp.).

The surface morphology of the films deposited from targets of different element composition (including the film deposited from Y-rich target) is seen on SEM scans (Figure 6.8) and AFM scans (Figure 6.11). XRD spectra are given in Figure 6.10, Figure 6.12.

Morphology

The films deposited from the Ba-rich target (upper left corners) have smooth surfaces, with almost no pores or outgrowths. When the yttrium content of the films increases (see Table 6.1, Figure 6.8, Figure 6.11) deep pores appear, together with particles on the film surface. The pores are present only in the films with excess of Y. The density of

pores is over 10^8 cm^{-2} for the films deposited from Y-rich targets, and is about 3×10^7 cm^{-2} for the films deposited from the Cu-deficient target. The average diameter of the pores increases with an increase of the yttrium content.

Big perfectly rectangular grains of *a*-oriented YBCO are clearly visible on the SEM scan of the film deposited from the Cu-deficient film (bottom left corner, Figure 6.8). Bright spots on the SEM scan of the film deposited from the Y-rich target (bottom right corner, Figure 6.8) are yttria particles, charged by the electron beam.

Crystal structure

The XRD θ/2θ-scans reveal the presence of yttria in the films deposited both from the Cu-deficient and from the Y-rich targets (Figure 6.10). The yttria is mainly (100) oriented, with some minor part in the (111) orientation. The lattice constant of (100)-oriented yttria in the films grown from the Cu-deficient and the Y-rich targets is very close to the bulk value 10.601 Å, and the strain $\delta d/d$ in the particles is low, ~0.4%. The crystallite size evaluation gives values 11-14 nm, implying that the nanoparticles of yttria are incorporated into the YBCO matrix. Careful analysis of XRD θ/2θ-scans reveals other tiny peaks of non-superconducting oxides, which may be interpreted as reflections from Cu_2O (in the film from the Ba-rich target) and Y_2BaCuO_x (Ba-rich and Y-rich targets).

Another important feature of the Y-enriched films is the preservation of *c*-orientation even for the thick films (420 nm, see Figure 6.12). The appearance of *a*-oriented YBCO is typical for films deposited by physical vapor deposition techniques. The film orientation tends to change from *c*- to *a*-orientation between 300 and 500 nm of thickness due to a secondary seeding process, caused by an increase of strain in the film. A higher growth rate of *a*-oriented phase results in a gradual overgrowth of *c*-oriented grains with the *a*-oriented ones. Films deposited from the stoichiometric and Ba-rich targets follow this rule: the part of *a*-oriented film, evaluated using standard (006) and (200) peak intensities, increased with thickness from nearly zero at 140 nm to 70% (stoichiometric target) and 27% (Ba-rich target) at 420 nm.

The situation is totally different for the Y-enriched films. A high density of pores provides the possibility of strain relaxation, so that seeding of the *a*-oriented grains becomes much less probable, and for the $Y_{1.5}Ba_2Cu_3O_x$ target the part of *a*-oriented film does not exceed 3%.

EDAX local composition analysis

The results of the EDAX measurements provide some valuable information on local composition of the films. For the beam of electrons focused on the film grain we obtain composition data close to the area measurements, which are averaging the elemental composition over the whole film. The difference is that for Y-rich, Ba-rich and stoichiometric targets the grains, according to the EDAX measurements, contain only one excess element: Y and Ba, respectively. The Cu-deficient target provided films with both excess Y and Ba present in the YBCO grains (with a 1:3 ratio). The amount of excess yttria in the main part of the Y-rich film deposited from $Y_{1.5}Ba_2Cu_3O_x$ target is about 6.5 mol% ($Y_{1.375}Ba_2Cu_3O_x$). This value exceeds the solubility limit for yttrium in YBCO, thus some yttria must be introduced into the YBCO matrix as nano-inclusions.

The big particles on the surface of the films mainly consist of oxides of Y and Cu (5:1, Y-rich) or Ba and Y (17:1 for Ba-rich, 5:1 for stoichiometric and Cu-deficient targets). These values were determined by subtracting the background signal from the underlying YBCO film, which is presumably stoichiometric.

The pores in the Y-enriched films might be formed by seeding of some Y-containing particles in the very beginning of the film growth. If these particles are not wetted by the YBCO, such pores may appear. The composition of excess material inside the film pores is Y:Ba ≈ 2:1, and the signal amplitude is about 7.5% of the overall signal. These particles inside of the pores might consist of the green phase (Y211), or some other complex oxides.

6.2.2 Y-doped films, superconducting properties

For the study of superconducting properties of Y-doped films we fabricated a set of samples from targets of different compositions ($Y_{1.25}Ba_2Cu_3O_x$, $Y_{1.5}Ba_2Cu_3O_x$ and

reference stoichiometric $Y_1Ba_2Cu_3O_x$) and with different thicknesses on LSAT substrates. The thickness is of interest since the preservation of *c*-orientation in Y-doped films was discovered. This is a promising fact for fabrication of thick high J_c YBCO films, and, eventually, for the improvement of the critical current in coated conductors.
All the deposition parameters were kept fixed for all the thicknesses and targets.
The films deposited from the stoichiometric $Y_1Ba_2Cu_3O_x$ target are called stoichiometric (or standard), from $Y_{1.25}Ba_2Cu_3O_x$, $Y_{1.5}Ba_2Cu_3O_x$ – 25% Y-doped and 50% Y-doped respectively (while keeping in mind that these definitions do not represent the actual composition of the films).

AC-susceptibility

The results of the critical temperature measurements are given in *Figure 6.13*.
Thin (140 nm) films all have good superconducting properties (narrow transitions, high transition temperatures), T_c of the Y-doped films are about 1 K lower than that of the stoichiometric film. With the thick (420 nm) films the situation is opposite: the T_c of the Y-doped films is even higher than the one of the thin doped films, while for the stoichiometric thick film T_c is lower, and the superconducting transition is broad. Two possible reasons can be suggested, one is the following: a better oxygenation of the Y-doped films through the deep pores during post-deposition oxygenation takes place, while the more dense stoichiometric film remains oxygen-deficient. Another possible reason may be a significant *a*-oriented part of the thick stoichiometric film. Usually the *a*-oriented films have T_c lowered by 2-3 K, and wider transition, exactly as we see on .
Both for thin and thick films the smallest width of the superconducting transition is for the 25% Y-doped film, implying a better uniformity of the film and or a faster increase of the critical current density with decreasing temperature.

Crystal structure

The XRD θ/2θ-scans of thick films are given in Figure 6.14, Figure 6.15. Yttria segregates in an oriented phase, the intensities of the corresponding XRD peaks clearly depend on the target doping level (Figure 6.14). Most of the film deposited from the

stoichiometric target is *a*-oriented, while no signature of *a*-orientation for Y-doped films can be found (Figure 6.15). XRD spectra of the film deposited from the $Y_{1.25}Ba_2Cu_3O_x$ target demonstrate splitting of the $K_{\alpha 1}$/ $K_{\alpha 1}$ peaks, which prove a high quality of the crystal structure of the film.

An evaluation of the *c*-lattice constants does not support the assumption of insufficient oxygenation of the stoichiometric thick film: the Y-doped film has $c = 11.696 \pm 0.009$ Å, while the film grown of stoichiometric target shows $c = 11.697 \pm 0.003$ Å. Equal values in general mean the same oxygenation level (see Chapter 3, Figure 3.6), though the Y-doped film can have some yttrium dissolved in the YBCO matrix, resulting in an increase of lattice constants. For the thin films the typical T_c versus *c*-lattice constant dependence is observed: 11.699 ± 0.010 Å and 90.1 K for the Y-doped film and 11.680 ± 0.004 Å and 91.1 K for the film deposited from the stoichiometric target.

Critical current densities: thin films

The critical current densities of 25% Y-doped, 50% Y-doped and stoichiometric thin (140 nm) films at different temperatures are given in Figure 6.16. The 25% Y-doped film has the highest critical current density at all measured temperatures and magnetic fields, exceeding the stoichiometric film values by 3-7 times. J_c of this film at 20 K is higher than J_c of the stoichiometric film at 5 K, in the whole range of magnetic fields! The 50% Y-doped film has the lowest J_c at 77 K, while at lower temperatures it shows some improvement comparing with the standard stoichiometric film.

Thick films, ageing

The three times thicker (420 nm) 25% Y-doped film has close high Jc values, which are 1.5 – 2 times lower comparing with those of the thin films (Figure 6.17). They still exceed the current density of the standard stoichiometric thin film even at 77 K, while at 50 K they are 2-3 times higher. A year after fabrication, an additional measurement of the critical current density of this thick sample was performed, in order to study possible ageing effects. Only minor signs of ageing were found at 77 K and high magnetic fields.

Thick films grown with low deposition rate

Thick 25% Y-doped films (400 nm and 600 nm) were deposited at half the deposition rate, 0.7 Å/s instead of 1.4 Å/s (with a lower energy density on the target). The J_c data of these samples are also given in Figure 6.17. These samples improve the results of our previous champion (thin 25%-doped film), having 30-100 kA/cm^2 at 77 K, and 3-4 MA/cm^2 at 50 K in a range of fields form 3 to 5 T. In addition, we may conclude that almost no reduction of J_c is found on going from a 400 nm to a 600 nm thickness. The results (especially at 50 K, with an over 1 MA/cm^2 critical current density up to 8.5 Tesla magnetic field) are promising for the fabrication of coated conductors with high J_c in high magnetic fields.

6.3 Combination of Y_2O_3 template layers and doped films

In order to study the combined effect of an yttria template layer and Y-doping of the target we fabricated a complete set of samples with and without yttria nano-particles, and three different levels of Y content in the YBCO target. The nano-particles were deposited on three substrates in one cycle, depositions of YBCO were performed simultaneously on bare and yttria decorated substrates.

AFM scans of these films and thick Y-doped films are given in Figure 6.18. Deep pores, typical for Y-doped films on bare substrates, become less dense but bigger in size with increasing thickness. A higher doping level results in an increase of size with almost no change in density of these pores. This picture is very different for the films deposited on yttria template layers. One of the possibilities, which were considered while planning this experiment, is a segregation of excess yttria during the YBCO film deposition on top of the yttria nanoparticles. This could be a way of controlling the size and density of yttria inclusions in the superconducting matrix. Instead, numerous pores in Y-doped films on template layers are seen, often connected with each other, breaking the superconducting film to partly separated clusters of YBCO grains. This is probably a result of too high Y concentration on the surface of the film at the early stages of the film growth, when the YBCO formation was competing with the continuous yttria

particles growth. As a result, the epitaxial conditions were spoiled for a large part of the film.

Due to some technical difficulties with the PLD equipment, the superconducting properties of films of this set are generally worse than the properties of the previous films, deposited in the same conditions. Thus, we can compare these results only within this set. The $J_c(B)$ curves for 77 and 50 K of 6 samples of the set are given in Figure 6.19. Both "simple" cases, the template layer or Y-doping, work as expected, resulting in an increase of J_c as compared with a standard stoichiometric film on a bare substrate. The combination of these effects gives non-satisfactory results. Surprisingly enough, the 25%-doped film on the yttria template layer is inferior to the 50%-doped film.

Sample	Target composition	Film composition by ICP	Film composition by EDAX	Excess material
HLP09	1.00:2.30:3.00 (0.95:2.19:2.86)	1.00:2.44:3.25 (0.90:2.19:2.92)	1.02:2.44:3.00 (0.95:2.27:2.79)	0.00:0.44:0.25 (ICP)
HLP08	1.00:2.00:3.00 (1.00:2.00:3.00)	1.06:2.48:3.00 (0.97:2.28:2.75)	1.02:2.43:3.00 (0.95:2.26:2.79)	0.06:0.48:0.00 (ICP)
HLP10	1.00:2.00:2.85 (1.03:2.05:2.92)	1.19:2.62:3.00 (1.05:2.31:2.64)	1.12:2.48:3.00 (1.02:2.26:2.73)	0.19:0.62:0.00 (ICP)
HLP07	1.50:2.00:3.00 (1.39:1.85:2.77)		1.49:2.13:3,00 (1.35:1.93:2.72)	0.49:0.13:0.00 (EDAX)

Table 6.1.Cation compositions of YBCO targets and corresponding films. In parentheses cation compositions normalized to 6 are given.

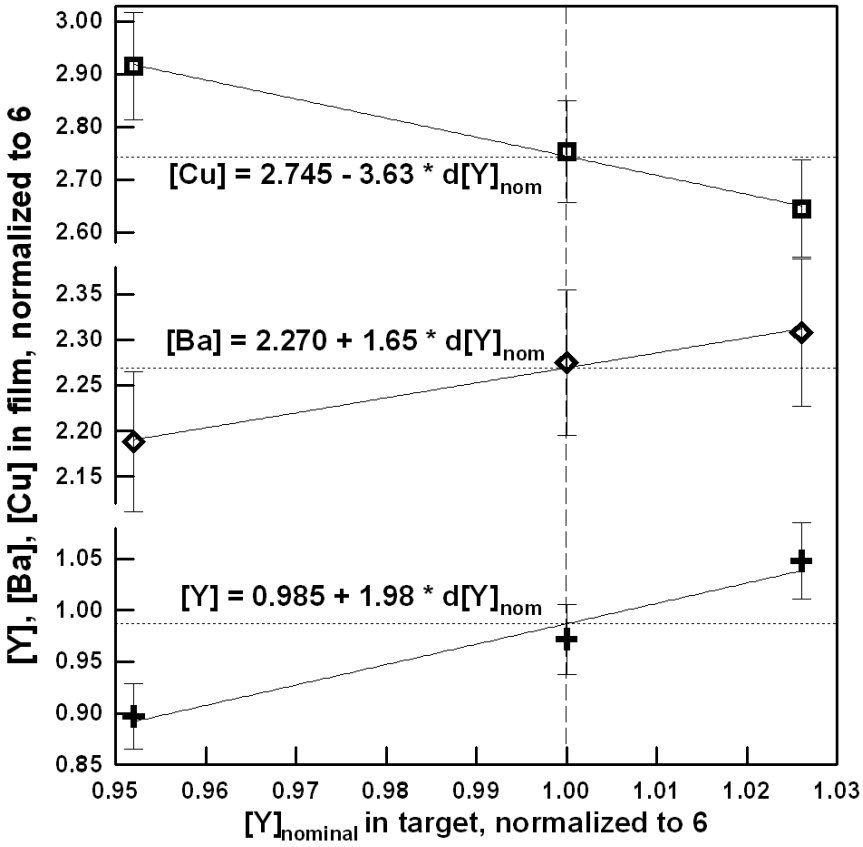

Figure 6.9. Contents of cations in the YBCO film measured with ICP technique for different yttrium contents in the target.

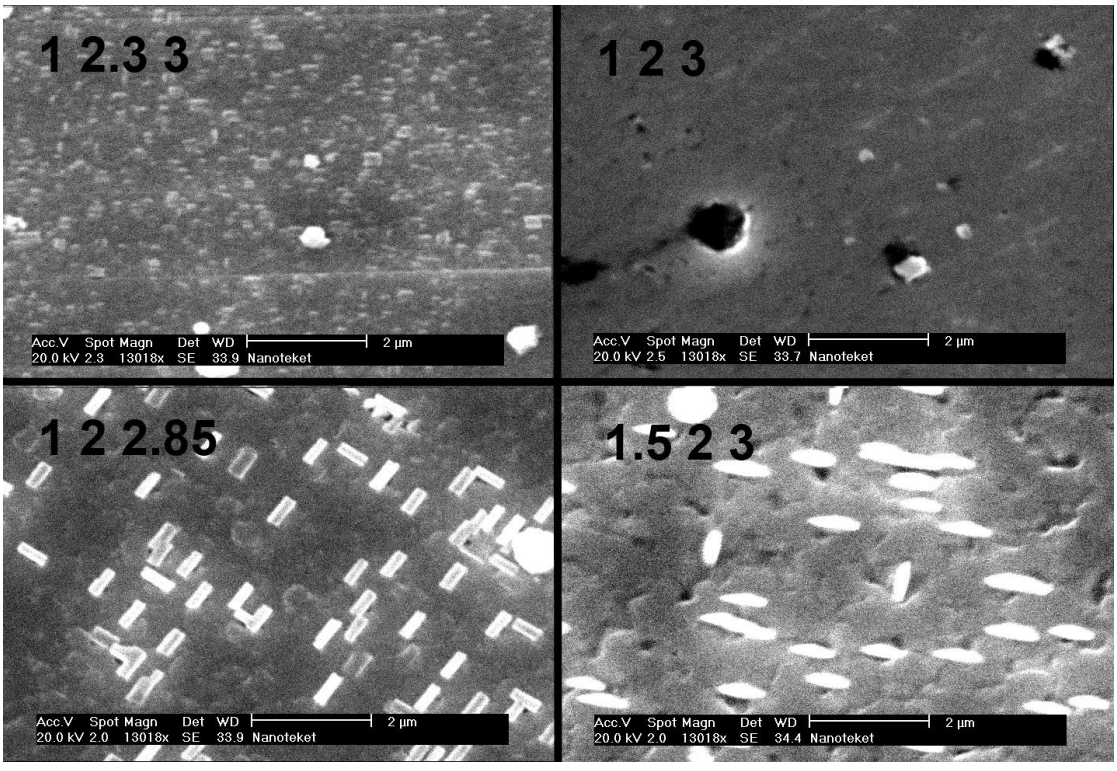

Figure 6.8. SEM micrographs of the YBCO thin films on NGO substrates deposited from different targets: Ba-rich target ($YBa_{2.3}Cu_3O_x$), stoichiometric target ($YBa_2Cu_3O_x$), Cu-deficient target ($YBa_2Cu_{2.85}O_x$), Y-rich target ($Y_{1.5}Ba_2Cu_3O_x$).

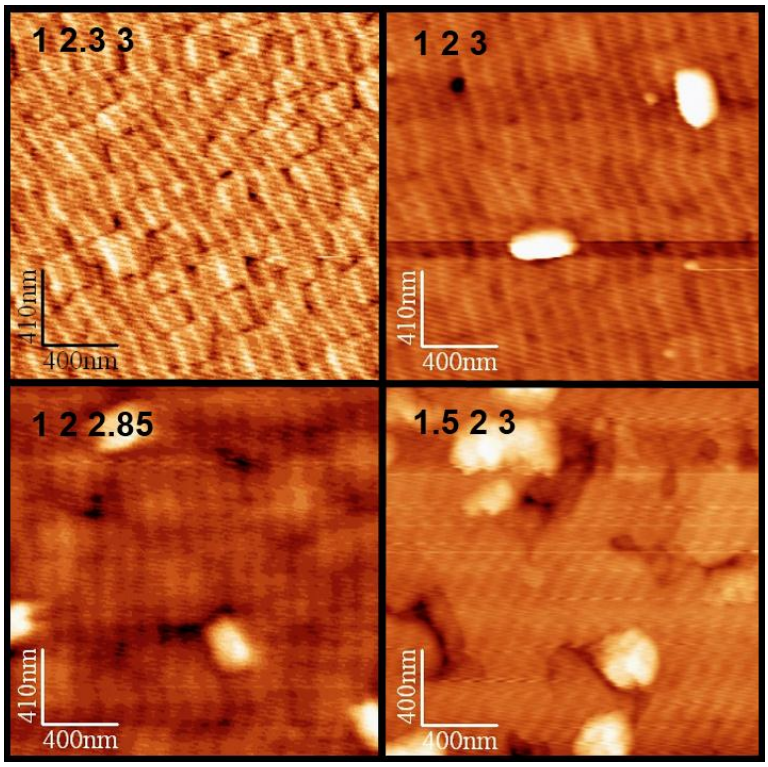

Figure 6.11. AFM micrographs of the YBCO thin films on LSAT substrates deposited from different targets: Ba-rich target ($YBa_{2.3}Cu_3O_x$), stoichiometric target ($YBa_2Cu_3O_x$), Cu-deficient target ($YBa_2Cu_{2.85}O_x$), Y-rich target ($Y_{1.5}Ba_2Cu_3O_x$).

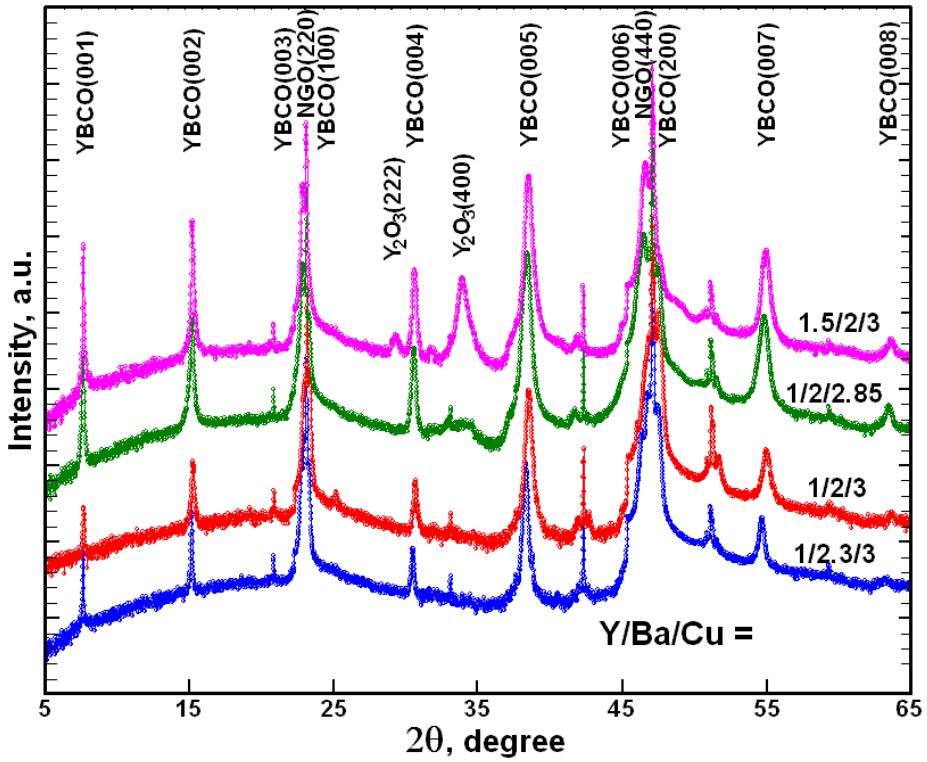

Figure 6.10. XRD θ/2θ-scans of YBCO films deposited from different targets on the $NdGaO_3$ substrates

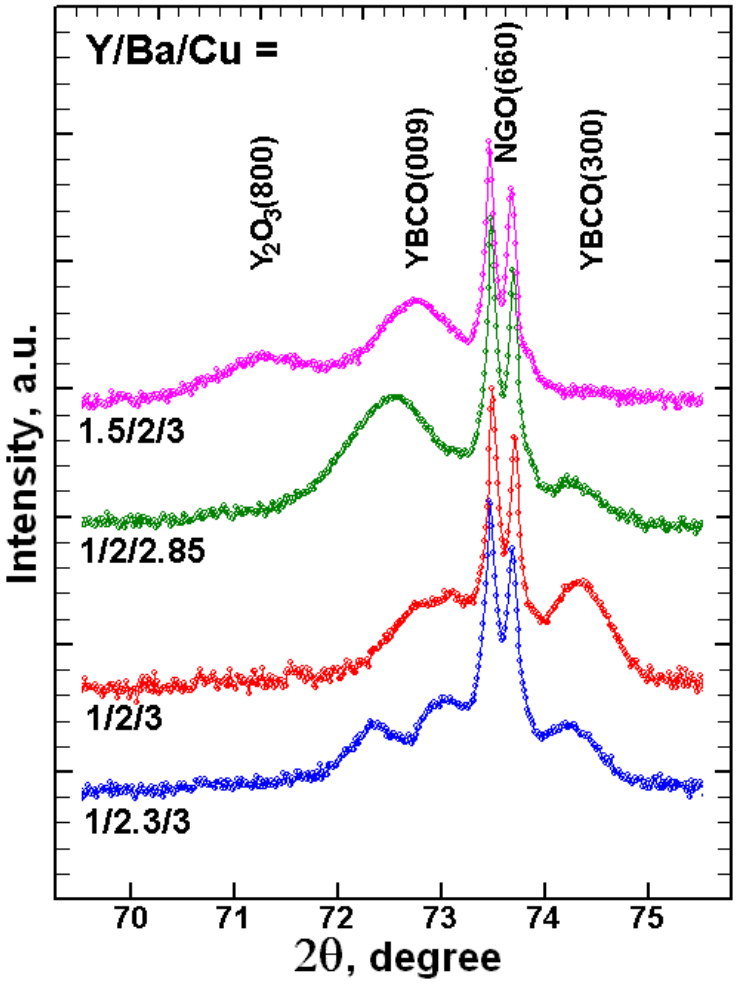

Figure 6.12. XRD θ/2θ-scans of YBCO films deposited from different targets in vicinity of the $NdGaO_3$(660) peak. The films are 0.42 μm thick. a-orientation is dominant in films deposited from stoichiometric and Ba-rich targets and is almost absent for the Y-enriched films.

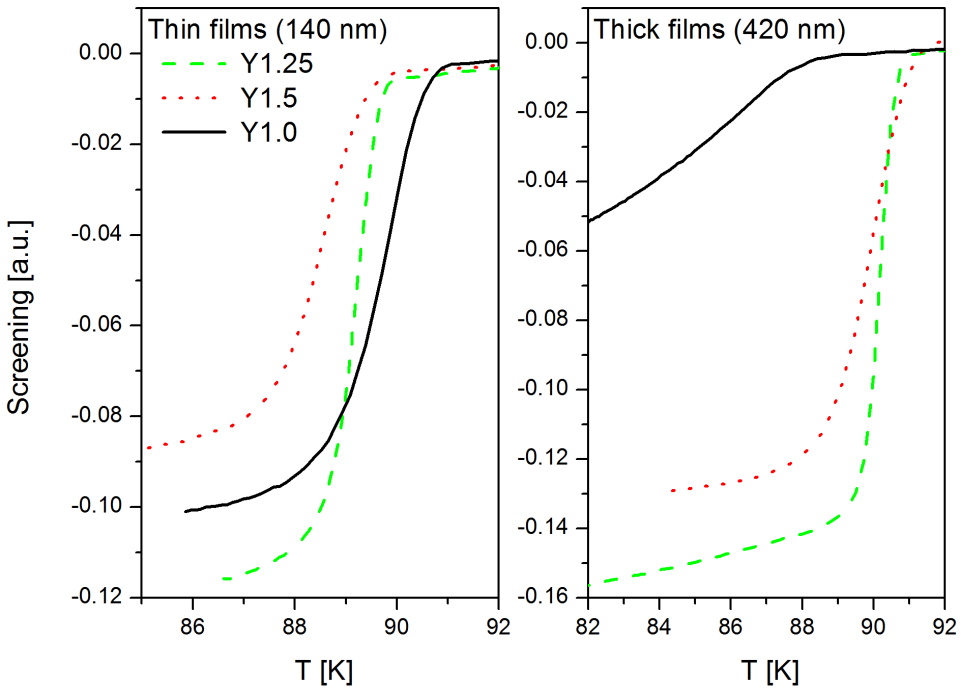

Figure 6.13. AC-susceptibility dependences on temperature for YBCO films deposited on LSAT substrates by pulsed laser ablation from targets with different amount of yttrium: solid line – stoichiometric target, dashed line – $Y_{1.25}Ba_2Cu_3O_x$, dotted line - $Y_{1.5}Ba_2Cu_3O_x$

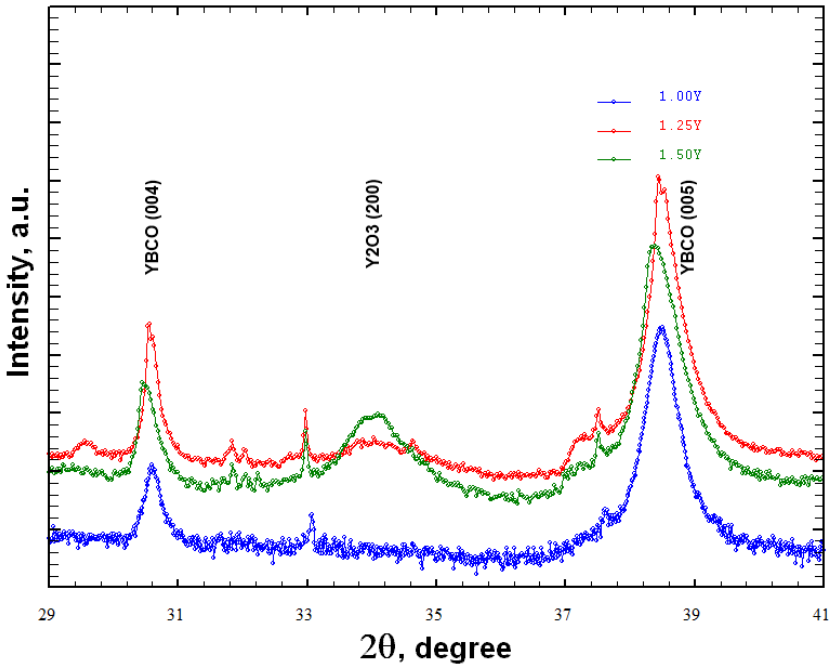

Figure 6.14. XRD θ/2θ-scans of YBCO films from targets of different Y contents on LSAT substrates. The yttria segregates in oriented inclusions.

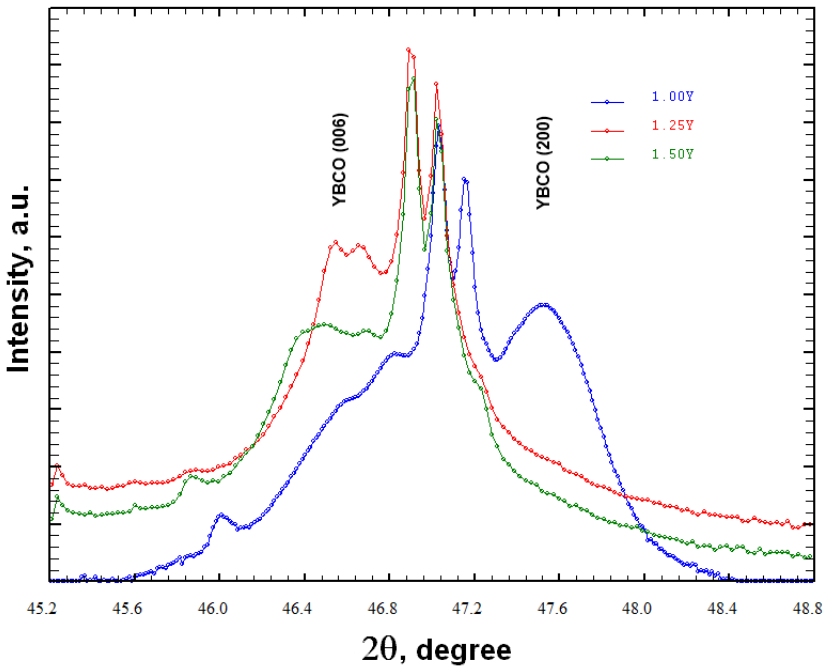

Figure 6.15. XRD θ/2θ-scans of YBCO films from targets of different Y contents on LSAT substrates. a-orientation is dominant in the film deposited from stoichiometric target and is absent for the Y-rich films.

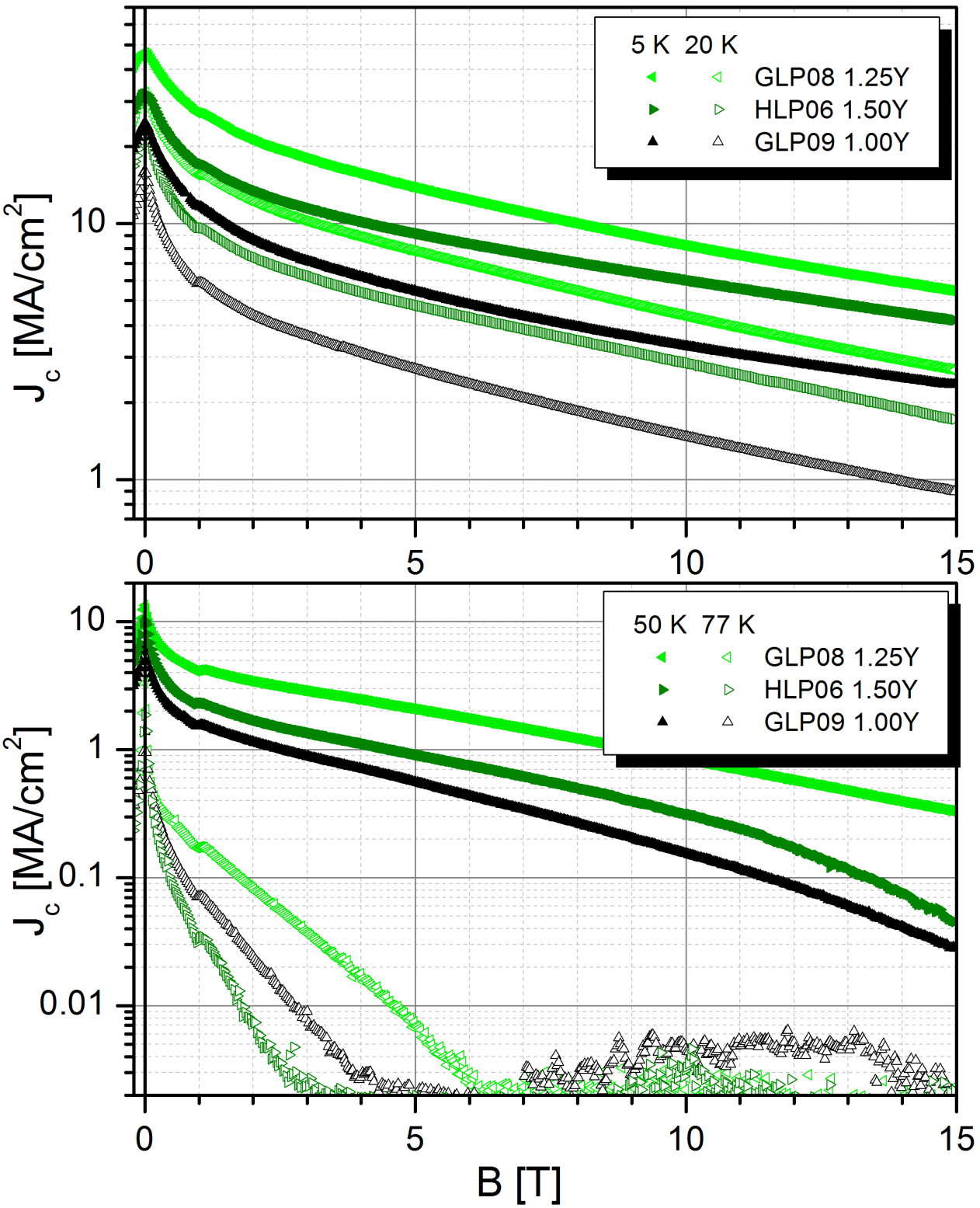

Figure 6.16. Critical current density vs magnetic field curves for 140 nm YBCO films deposited from targets of different Y contents on LSAT (100) substrates. Black triangle up: stoichiometric target; green (light) triangle left: $Y_{1.25}Ba_2Cu_3O_x$; olive (dark) triangle right - $Y_{1.5}Ba_2Cu_3O_x$. Upper plot: open symbols for 20 K, filled for 5 K. Bottom plot: open symbols for 77 K, filled for 50 K.

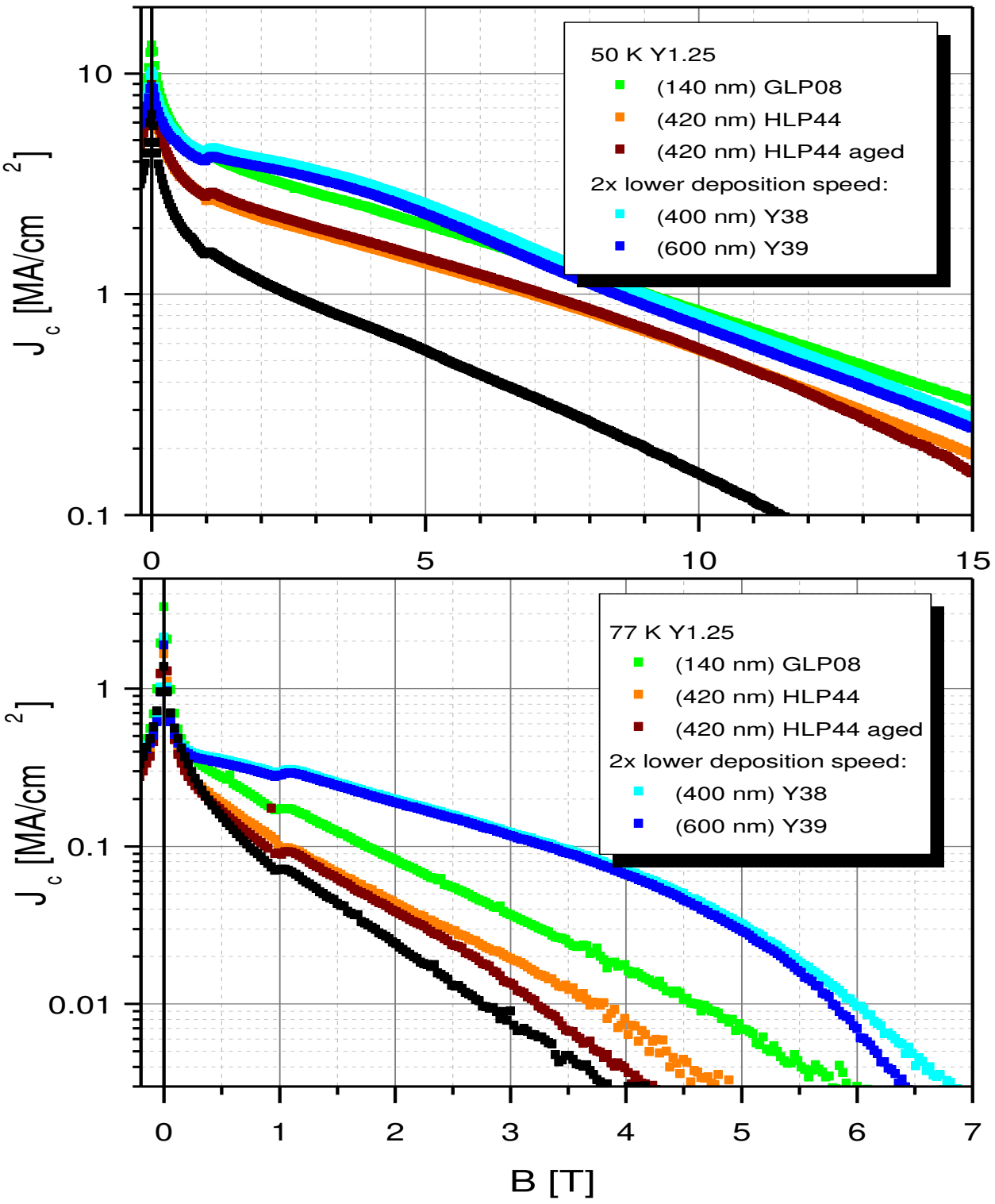

Figure 6.17. Critical current density vs magnetic field curves for YBCO films of different thicknesses deposited from the $Y_{1.25}Ba_2Cu_3O_x$ target on LSAT (100) substrates. Green – 140 nm GLP08, orange – 420 nm HLP44, brown – HLP44 aged (a year after fabrication). Blue squares represent films deposited with a lower deposition speed, 400 nm and 600 nm thick. Black squares are from the reference 140 nm thick GLP09 film deposited from the stoichiometric target

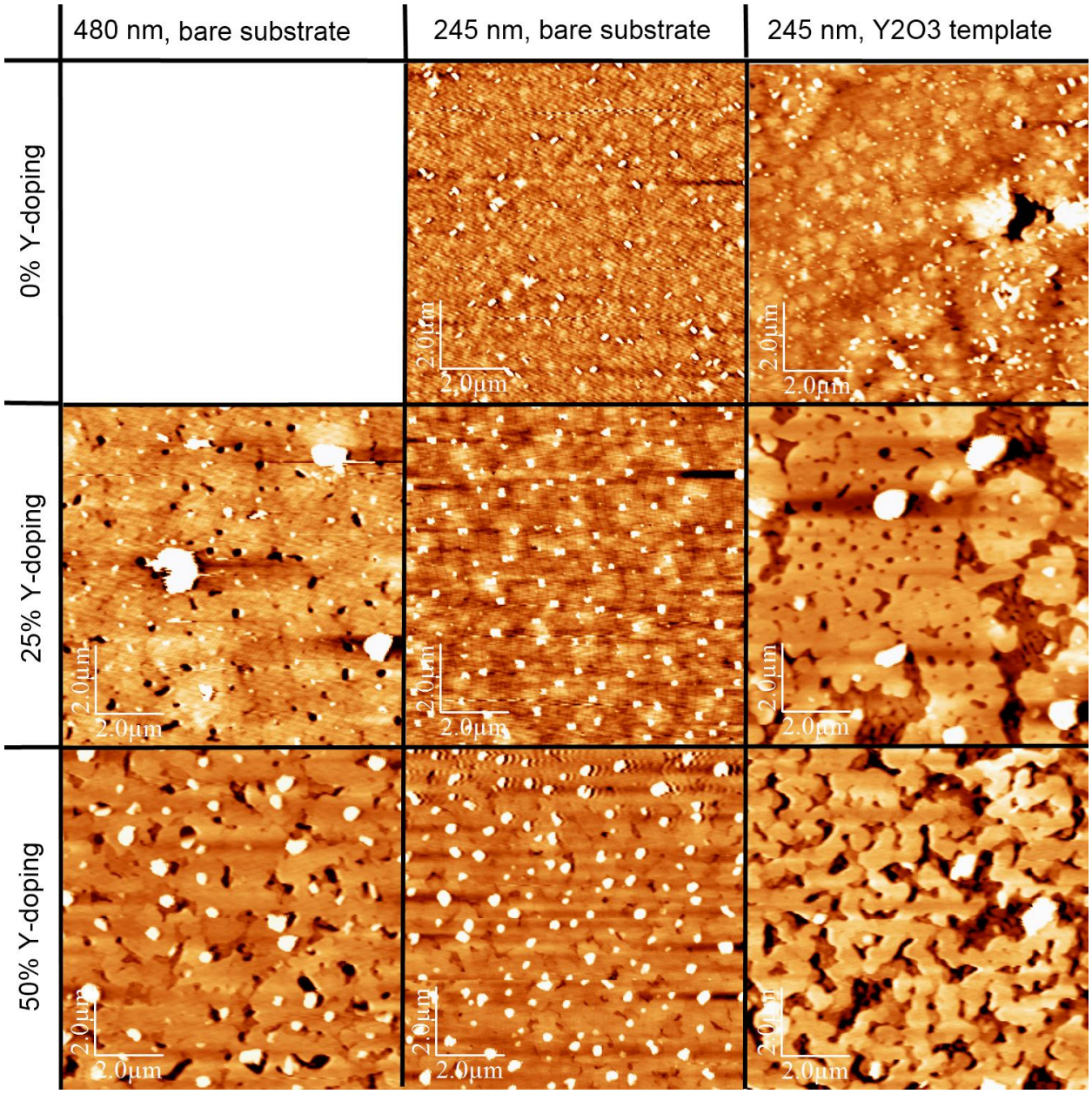

Figure 6.18. AFM micrographs of YBCO films deposited from targets of different Y contents on LSAT substrates. 480 nm, 245 nm, 245 nm on yttria template layer.

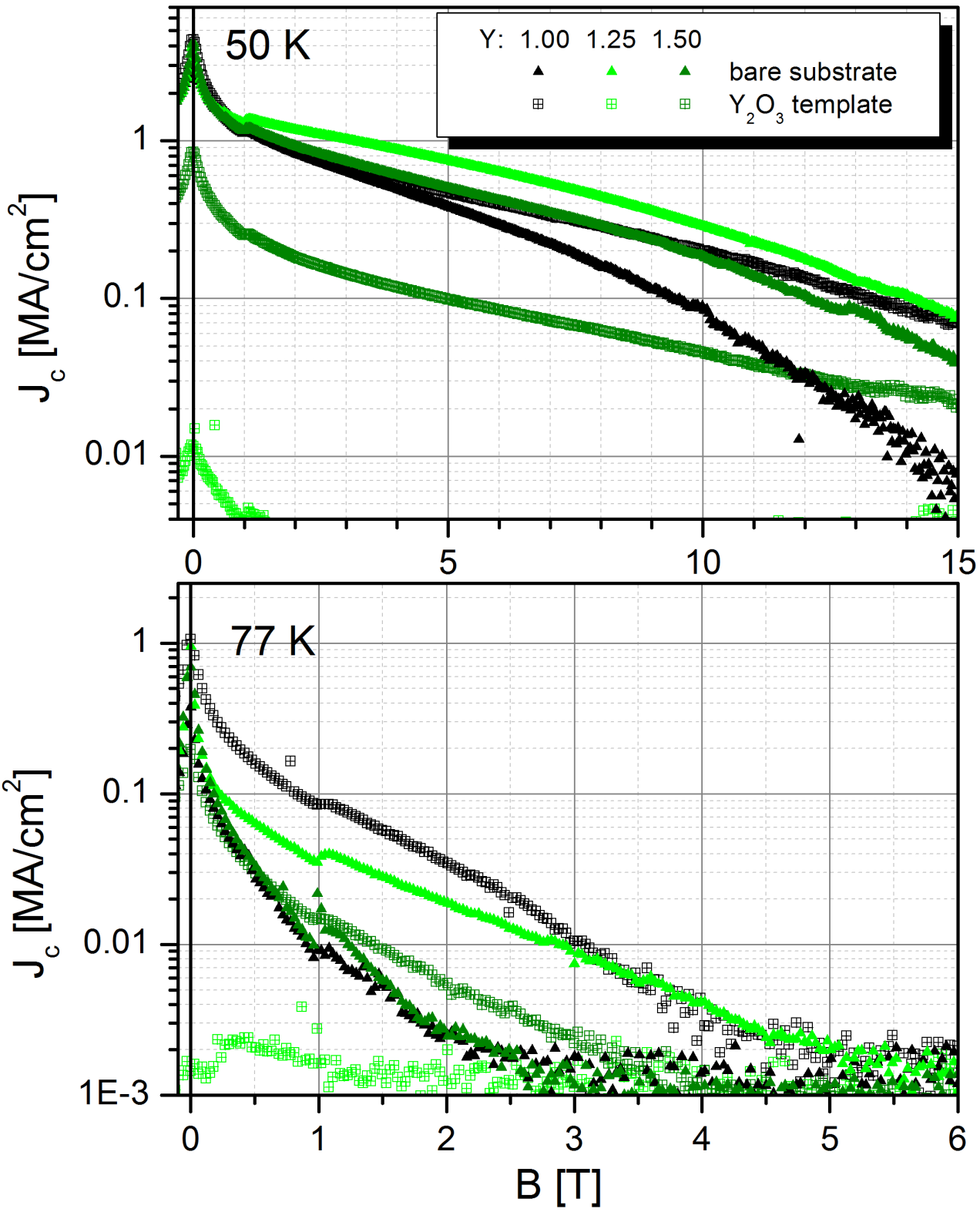

Figure 6.19. Critical current density vs magnetic field curves for YBCO films deposited from targets of different Y contents on LSAT (100) substrates with and without yttria decoration, 77 K. Triangles: LSAT; squares: yttria decorated LSAT; black: stoichiometric target; green (light): $Y_{1.25}Ba_2Cu_3O_x$; olive (dark): $Y_{1.5}Ba_2Cu_3O_x$.

7 (NdBa)MnO_3 thin films

As was discussed in chapter 4, lattice distortions have a significant impact on the carrier mobility and the magnetic properties of manganates. The internal orthorhombic distortion of the lattice depends on the mismatch between the MnO_2 and RO sub-lattices which may be described by the tolerance factor $f = (\langle r_A \rangle + r_O)/[\sqrt{2}(r_{Mn} + r_O)]$, where r_{Mn} and r_O are ionic radii of Mn and O, and $\langle r_A \rangle$ is the averaged radius of the elements on the A-site of the perovskite lattice. For NBMO with the tolerance factor f = 1.011 very close to 1 and a small difference between Nd-O and Ba-O bond lengths, an external strain driven by lattice mismatch between the substrate and the growing film might be the dominant effect.

All the NBMO films were deposited on perovskite substrates by pulsed laser deposition using a commercially available ceramic target with nominal element composition $Nd_{0.67}Ba_{0.33}MnO_3$.

In the first sub-chapter the results of our study of NBMO films on different substrates are reported, the second sub-chapter is dedicated to an investigation of thickness effects on the magnetic and structural properties of the films deposited on LSAT ((100) $(LaAlO_3)_{.3}$-$(Sr_2AlTaO_8)_{.7}$) substrates. The film growth on different substrates results in different strain direction and amplitude, and the film thickness might be an important parameter due to the strain relaxation process.

7.1 Bi-axial strain effects

7.1.1 Experiment

Two perovskite substrates, (001) $SrTiO_3$ (STO) and (110) $NdGaO_3$ (NGO), with good match of lattice constants with the bulk value for NBMO were chosen in order to study the effect of small substrate-induced strain on the film properties. The thermal expansion coefficients of the substrates are both close to that of NBMO, therefore the influence of thermal expansion on the external strain value may be neglected. A comparison of the effective lattice constants of the substrates and NBMO is given in

Table 4.1. The lattice mismatches lead to a small tensile strain on STO and a small compressive strain on NGO respectively.

The deposition conditions were varied to study the effect of different parameters on the structural and magnetic properties of the NBMO films. The standard deposition conditions were: energy density on target 1.5 J/cm^2, pulse repetition rate 2 Hz, deposition temperature 650 °C, total pressure of argon/oxygen mixture in the chamber during deposition 0.2 mbar, oxygen partial pressure 0.012 mbar. This low oxygen pressure was chosen in order promote the formation of high quality crystal structure. We used the lowest temperature (650 °C) of the substrate during the deposition still providing epitaxial growth of manganates films. 2 Hz (500 ms) pulse repetition rate provides a deposition rate of 0.6 Å/s which is sufficiently low in comparison with the typical relaxation time of the deposited material on the substrate surface at the given deposition conditions (average relaxation time 0.3-0.5 s, determined by RHEED [53]), thus the film may be considered as grown under thermodynamic equilibrium conditions.

It is well known that the properties and the structure of manganate films strongly depend on oxygen contents of the films, so in addition to the standard conditions we fabricated films:

- at high oxygen pressure (0.8 mbar total pressure, Ar/O2 = 1/1);
- with increased deposition rate (the deposition rate per pulse remained the same, while the overall deposition rate increased 10 times with an increase of repetition rate from 2 Hz to 20 Hz);
- with increased deposition rate and subsequent oxygenation (the oxygenation was performed at 450 °C for 1 hour in 500 mbar of oxygen immediately after the deposition).

At 20 Hz (50 ms) pulse repetition rate the deposition process is essentially kinetic, the deposition rate leaves for the upcoming material a shorter time than the relaxation time for incorporation into crystal structure.

The films are 90 (2 Hz) and 120 nm (20 Hz) thick, with small variations due to the change of deposition conditions.

7.1.2 Results

Structural properties.

XRD studies of all NBMO films showed single (001)-orientation along the substrate normal. The deposition parameters of the samples with corresponding structural information are summarized in Table 7.1.

NBMO/NGO: compressive strain

Deposition at low rate (0.6 Å/s) results in smooth films (Figure 7.1a) with rare particulates on the surface. The XRD θ/2θ-scans showed narrow peaks with satellite peaks (Figure 7.2, bottom curves). The thickness evaluation using the distance between satellite peaks, and using the main peak width and the Scherrer formula [51] both are in good agreement with the thickness estimation using the pre-determined deposition rate. The lattice constant variations of the films are small; the lattice constant of the film deposited at "standard" conditions is 3.966 Å, decreasing to 3.937 Å for the film grown at high oxygen partial pressure. Both numbers are much higher than the standard bulk value (3.886 Å).

High deposition rate results in rough films (Figure 7.1b), the θ/2θ-scans show peaks of two different phases (Figure 7.2, sample GN09), with corresponding to out-of-plane lattice constants 3.952 and 3.936 Å. The evaluated lattice constant variations are higher than for the films grown at low deposition rate. Oxygenation after deposition does not change the structural parameters of the films.

NBMO/STO: tensile strain

All films deposited on STO substrates have a smooth surface with roughness $R_a < 2$ nm (Figure 7.1c). The film peaks on the XRD θ/2θ-scans are in close vicinity of the $SrTiO_3$ (00*l*) peaks that makes the diffraction data hard to interpret and for some films it is impossible to determine the structural parameters.

An increase of oxygen partial pressure during the deposition results in a decrease of the out-of-plane lattice constant of the NBMO film on STO substrate to the bulk value,

3.886 Å. The peaks are rather pronounced, with full width at half maximum about 0.11-0.13°, but possible thickness oscillations are masked by noise after removal of the $K_{\alpha 2}$ line. Lattice constant variation and thickness evaluation by the Scherrer formula give numbers similar to those of the film deposited simultaneously on NGO.

To our surprise, oxygenation after deposition at high rate resulted in an increased out-of-plane lattice constant, 3.922 Å (Figure 7.2, top curve). The lattice constant variation is still very low (0.14%, Table 7.1), and the thickness evaluation is in good agreement with the thickness estimated from the deposition rate.

Sample	Substrate	p_{O2}, mbar	Pulse repetition rate, Hz	Lattice constant *c*, Å	Film-to-bulk cell volume ratio[#]	Lattice constant variation, %
GN05	$NdGaO_3$	0.012	2	3.966	1.007	0.22
GS06	$SrTiO_3$			~3.905[x]		n/a
GN07	$NdGaO_3$	0.4	2	3.937	1.000	0.07
GS08	$SrTiO_3$			3.886		0.02
GN09	$NdGaO_3$	0.012	20	3.952 3.936	1.004 1.000	0.35 1.86
GS10	$SrTiO_3$			~3.905[x]		n/a
GN11	$NdGaO_3$	0.012[*]	20	3.955 3.927	1.005 0.998	0.44 1.75
GS12	$SrTiO_3$			3.922		0.14

Table 7.1. Deposition parameters and structural properties of the NBMO films [*] oxygenation after deposition, 1 hour at 450 °C in 500 mbar of oxygen.

[x] the film peak is masked by the strong substrate peak

[#] calculated assuming $a_{film} = a_{substrate}$

Magnetic properties.

The magnetic properties of the films are summarized in Table 7.2.

The magnetization versus temperature plots for the samples on STO substrates are shown in Figure 7.3. The films exhibit a typical behavior of cubic NBMO: a ferromagnetic transition takes place around 110 K, followed by an antiferromagnetic transition at temperatures around 30 K. T_{Curie} values were obtained by extrapolation of linear fits of $M^2(T)$ to 0. The standard deposition conditions lead to the smallest magnetization values without significant anisotropy between in-plane and out-of-plane film orientations. Both increasing oxygen partial pressure during deposition and high deposition rate resulted in an increase of the magnetic moment of the film. These samples are essentially anisotropic and have different orientations of the easy-axis: out-of-plane for the sample annealed after deposition and in-plane for the sample grown at high oxygen pressure.

A huge paramagnetic signal from the NGO substrate (four orders of magnitude higher than the expected film signal) makes it difficult to examine any FM properties of the samples on NGO substrates. It is not possible to measure the T_{Curie} directly. However, a subtraction of the linear signal of the NGO on M(B) plot allows us to extract a hysteresis curve for the film (Figure 7.4, bottom inset).

To study the magnetic properties of NBMO films grown under compressive strain we prepared additional samples on non-magnetic $(LaAlO_3)_{.3}$-$(Sr_2AlTaO_8)_{.7}$ (LSAT) substrates with almost the same effective lattice constant as NGO (see Table 4.1). 40 nm thick NBMO films were grown at "standard" deposition conditions simultaneously on a 20 nm NGO buffer layer and on a bare LSAT substrate as a reference. We consider NGO buffer layer to be low distorted and providing surface for an epitaxial growth close to that of NGO substrate. The M(T) dependence of the NBMO film on the buffer NGO layer showed both ferromagnetic and paramagnetic features (Figure 7.4, top inset). Fitting the paramagnetic signal of NGO layer allows extraction of the M(T) of the NBMO part, which looks similar to that of films on STO substrates.

The M(B) curve obtained for the NBMO/NGO/LSAT sample (Figure 7.4, main picture) shows a magnetic moment in saturation close to the value extracted from the data for the NBMO/NGO sample (Figure 7.4, bottom inset), 0.81 μ_B per unit cell, and ~1.4 μ_B

per unit cell, respectively. The hysteresis curve of the reference NBMO/LSAT sample is also given in Figure 7.4.

Sample	Substrate	T_{Curie}, K	M_c/M_{ab} (500 Oe, 10 K), μ_B/unit cell	Anisotropy, M_c/M_{ab}	M_c/M_{ab} (10 K) in saturation, μ_B/unit cell	Anisotropy, M_c/M_{ab}
GS06	$SrTiO_3$	110	0.128 / 0.135	0.95	0.21 / 0.20	1.05
GS08	$SrTiO_3$	105	0.174 / 0.209	0.83	0.29 / 0.32	0.91
GS10	$SrTiO_3$	105	- / 0.177	-	- / 0.42	-
GS12	$SrTiO_3$	115	0.207 / 0.164	1.26	0.41 / 0.35	1.17

Table 7.2.Magnetic properties of the NBMO films.

7.1.3 Discussion

Both surface observations and XRD studies show high perfection of the structure of the NBMO films grown at low deposition rate. The observed thickness oscillations on the XRD θ/2θ-scans can be seen if both the surface of the film and the film-substrate interface are smooth, and the lattice constant does not change significantly through the film. The thickness oscillations were observed previously for manganate films, but for thinner films (for example, 40 nm in [54,55]). This implies that the structure of the film is formed in the very beginning of deposition, and remains almost unchanged throughout the whole film.

The structural properties of all NBMO films are summarized in Table 7.1. We can clearly see that the out-of-substrate plane lattice constant of the NBMO films on NGO substrates is greater than that on STO substrates in every pair of simultaneously deposited samples. This effect is explained by bi-axial strain, introduced into the film lattice by the substrate (as was discussed in Chapter 4).

Structural properties: NGO substrates

Assuming pseudomorphic growth (cube-on-cube growth with inheritance of translation distances on the substrate surface $a_{\text{film}} = b_{\text{film}} = a_{\text{substrate}}$ in case of (100)-oriented substrate with cubic lattice), we may calculate the film-to-bulk cell volume ratio as (see Table 7.1, $a_{\text{bulk}} = 3.886$ Å):

$$VR = \frac{V_{film}}{V_{bulk}} = \frac{{a_{substrate}}^2 \cdot c_{film}}{{a_{bulk}}^3}. \qquad (7.1)$$

In general the NBMO films experiencing compressive strain on NGO substrates follow the volume-preserving dilation: the film-to-bulk cell volume ratio is 1 or slightly higher for all deposition parameters and phases. The small (~0.5%) increase of volume is often observed for thin films due to generation of defects in the film during growth. Oxygen vacancies are known to be one of the most usual defects in the oxide thin films, resulting in expansion of the lattice with increasing density. The behavior of the out-of-plane lattice constant in NBMO films support this assumption: an increase of the oxygen partial pressure during film growth results in a decrease of the lattice constant both on NGO and STO substrates. The unit cell volume of the NBMO film on NGO substrate prepared at high oxygen partial pressure is equal to the cell volume of a bulk sample, implying complete oxygenation of the manganate during growth.

These observations allow an assumption of the growth of completely strained pseudomorphic NBMO film on NGO substrates up to a thickness of 90 nm. The lattice constant does not change much through the whole film thickness, as confirmed by the observation of Laue oscillations and by the small lattice constant variations calculated from the width of the X-ray diffraction peaks (Table 7.1). The tetragonal distortion of the lattice follows the volume-preserving dilation with a Poisson ratio $\nu = 0.5$ (see (4.1)). Pseudomorphic growth for LSMO/LCMO thin films in [56] was observed up to a critical thickness t_c that could be calculated as 86 [nm]/ε_{xx}^2 [%]. Estimation of the pseudomorphic growth limit for NBMO films gives t_c of 210 and 360 nm on NGO and STO, respectively.

An increase of the deposition rate results in formation of a secondary phase with much smaller out-of-plane lattice constant (Table 7.1). This secondary NBMO phase appears together with the formation of particles on the surface of the film. The primary phase has a lattice constant similar to that of the film deposited at low rate, and probably relates to the smooth part of the film, while the secondary phase seems to segregate in particles on the surface of this smooth film, formed as a result of secondary seeding. Three possible mechanisms of the secondary phase formation may be suggested: partial relaxation of the strained film after secondary seeding, different oxygen content in the secondary phase, and different Nd/Ba ratio. The negligible effect of post-deposition oxygenation probably excludes a difference in oxygen contents of the two phases. Segregation of a phase with a lower level of Ba was commonly observed for bulk samples prepared in a reduced atmosphere or with insufficient oxygen pressure during sintering [57]. The simplest explanation is the strain relaxation: a decrease of the out-of-plane lattice constant of the secondary phase as compared with the primary and a high level of lattice constant variation in the secondary phase support this assumption.

Structural properties: STO substrates

The growth of NBMO film on STO substrates seems to be quite different. The out-of-plane lattice constant of the sample grown at the high oxygen pressure is precisely equal to the bulk value 3.886 Å. For any in-plane strain ε_{xx} it gives a non-feasible Poisson ratio $\nu = 0$. This means that the growth of NBMO on STO is not pseudomorphic, and in-plane lattice constants do not follow the substrate, and probably are of a bulk value as well.

Still, the sample grown at the high oxygen pressure has the lowest out-of-plane lattice constant, comparing with the film deposited at standard conditions and at high deposition rate. No signs of a secondary phase formation were observed for the NBMO films on STO substrates, neither on the AFM micrographs, nor on the XRD scans, even for high deposition rate. An oxygenation of the film fabricated at high deposition rate results in an unexpected increase of the out-of-plane lattice constant. The integral peak

intensity correlates to the total volume of the NBMO film, making the presence of a peak of secondary phase at higher θ angle (corresponding to smaller lattice constant) below the substrate peak improbable. The increase of the lattice constant may be a result of generation of R, A cation vacancies, as was observed in [58] with an increase of oxygen pressure during deposition.

In conclusion, we observe that the effects of compressive and tensile strain on the formation of the NBMO film are totally different. The compressive strain seems to result in a pseudomorphic growth forming a completely strained film with tetragonal-distorted lattice following the volume-preserving dilation ($\nu = 0.5$). The volume of the unit cell depends on oxygen contents of the film and changes the out-of-plane lattice constant from 3.93 Å for almost completely oxygenated film to 3.96 Å for the films with lower oxygen contents. The strain results in the segregation of a secondary phase when deposition conditions become non-optimal for the film growth.

On the substrate providing tensile strain the film grows independently of the substrate lattice. The lattice constant variation along the film thickness is much smaller than for NBMO films under compressive strain, and the surface remains smooth even for non-optimal deposition conditions. Post-deposition oxygenation of such a film results in an increase of the cell volume, probably due to generation of R, A vacancies.

Magnetic properties

The magnetic properties of the NBMO films show strong dependence both on the deposition conditions and on the substrate material, in good agreement with the structural parameters.

The T_{Curie} for all films on STO ranged from 105 to 115 K, somewhat lower than the bulk values for the cubic Nd/Ba disordered NBMO (120-160 K). The saturation magnetic moment for the films on STO (Table 7.2) is also lower than the bulk value of 3.0 μ_B/cell. The suppression of the measured values compared to the bulk properties may be attributed to an increased density of defects in the films compared with the ceramic samples.

One possible reason for weaker ferromagnetic properties is the presence of oxygen vacancies in the manganate, effectively suppressing the double exchange interaction. Indeed, the sample GS06, fabricated at low oxygen partial pressure and presumably containing some oxygen vacancies in the lattice, shows significantly lower magnetic moment as compared to the sample GS08, fabricated at high oxygen partial pressure and completely oxygenated, as far as can be judged from the out-of-plane lattice constant. Other samples cannot be compared directly with the first two due to changes in the deposition conditions and possible deviations from stoichiometry in the lattice. Adding data from the sample on LSAT (T_{curie}= 100 K), deposited in "standard" conditions, we could estimate the parameters of the model (4.3): $\alpha \sim 11$, $\Delta \sim 2100$, $T_p(0)$ ~ 105 K. The results are in good agreement both with theoretical evaluations [41] and experimental data [56].

The anisotropy of the magnetic properties shows a clear correlation with the structure of the film (see Figure 7.5, Table 7.1 and Table 7.2). The easy axis of the film on STO changes its orientation from the in-plane for the completely oxygenated film to the out-of-plane for the film with a high out-of-plane lattice constant (Figure 7.5).

For the films grown on different substrates we can see another correlation between the structural and magnetic properties (Figure 7.5, right-bottom curve). The in-plane saturation magnetic moment M_{ab} of the NBMO film grown at the "standard" deposition conditions is 0.20 μ_B/cell for the STO substrate with out-of-plane lattice constant about 3.905 Å (Table 7.2), smaller than that of the NBMO film on a LSAT substrate (0.41 μ_B/cell and 3.961 Å, Figure 7.4) The hysteresis curve of the NBMO film on a NGO substrate recovered after subtraction of the paramagnetic background (see bottom inset Figure 7.4), shows even higher M_c, ~1.4 μ_B/cell, with corresponding lattice constant 3.966 Å. This evaluation should be used with caution, due to the high probability of error when subtracting a background which is much larger than the signal. The NBMO film on a NGO buffer layer on a LSAT substrate shows an intermediate magnetization 0.81 μ_B/cell between the measured value of the film on

LSAT and the evaluated value for the film on NGO substrate. The M_{ab} value increases extremely rapidly with an increase of the out-of-plane lattice constant.

7.1.4 Conclusions

In order to investigate the structural and magnetic properties of (NdBa)MnO_3 thin films we fabricated a set of samples by pulsed laser deposition on several perovskite substrates at different deposition conditions. The NBMO films were *c*-oriented for all deposition parameters. At low deposition rate and low oxygen partial pressure the films show smooth surfaces and sharp XRD peaks with clear Laue oscillations on the $\theta/2\theta$ scans. The NBMO unit cell volume depends on deposition conditions, likely as a result of different oxygen contents in the films.

For deposition on the NGO substrates providing compressive strain into the film the induced in-plane distortion results in a change of the out-of-plane lattice constant, following a volume-preserving dilation. An increase of deposition rate results in segregation of a secondary NBMO phase either as a result of partial strain relaxation, or due to formation of a phase with different Nd/Ba ratio.

The samples on STO substrates that provide tensile strain do not show the pseudomorphic growth and the film seems to grow relaxed from the very beginning of deposition. Post-deposition oxygenation of such films results in an increase of the out-of-plane lattice constant, probably due to R, A cation vacancies formation.

All the films deposited on STO substrates have ferromagnetic transitions at temperatures 105-115 K. Their magnetic properties are essentially anisotropic, and strongly correlated with the crystal structure distortions: the easy axis changes its orientation from the in-plane to the out-of-plane with an increase of the out-of-plane lattice parameter. An increase of magnetization with a decrease of the substrate lattice parameter can be seen for various substrates introducing compressive strain in the films.

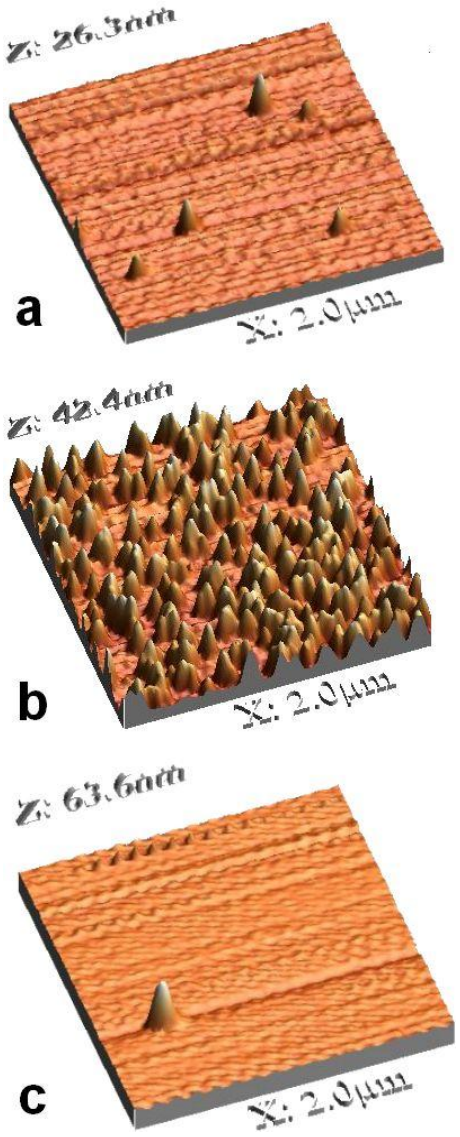

Figure 7.1. AFM scans for the NBMO thin films: (a) NGO substrate, low deposition rate, (b) NGO substrate, high deposition rate, (c) STO substrate

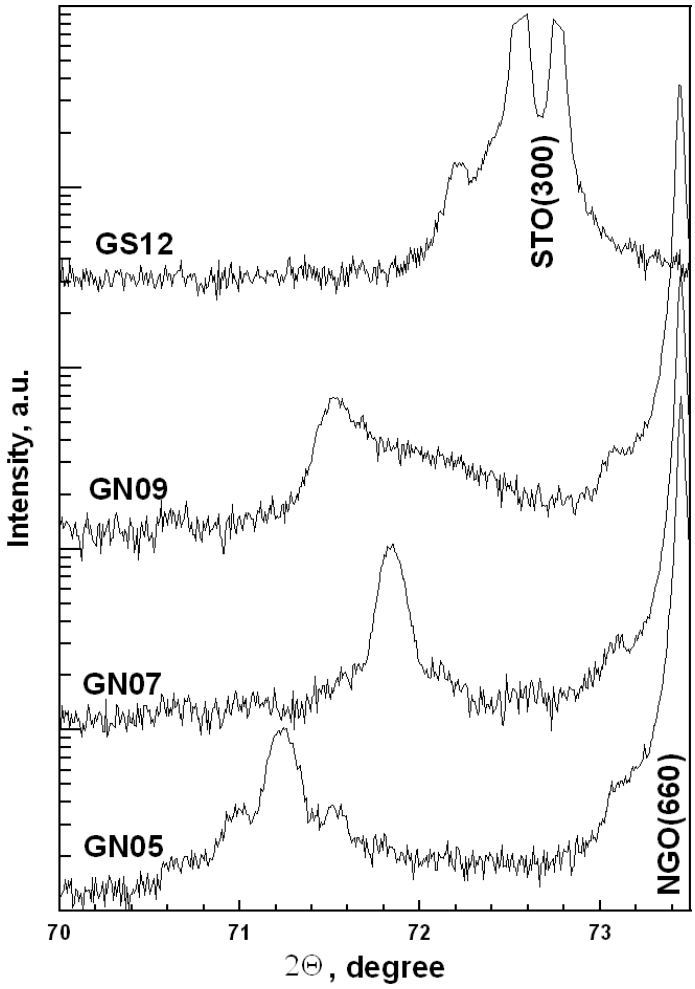

Figure 7.2. X-ray diffraction θ/2θ-scans of the NBMO thin films on perovskite substrates. Deposition parameters: see Table 7.1. $K_{\alpha 2}$ signal removed numerically except for the top curve

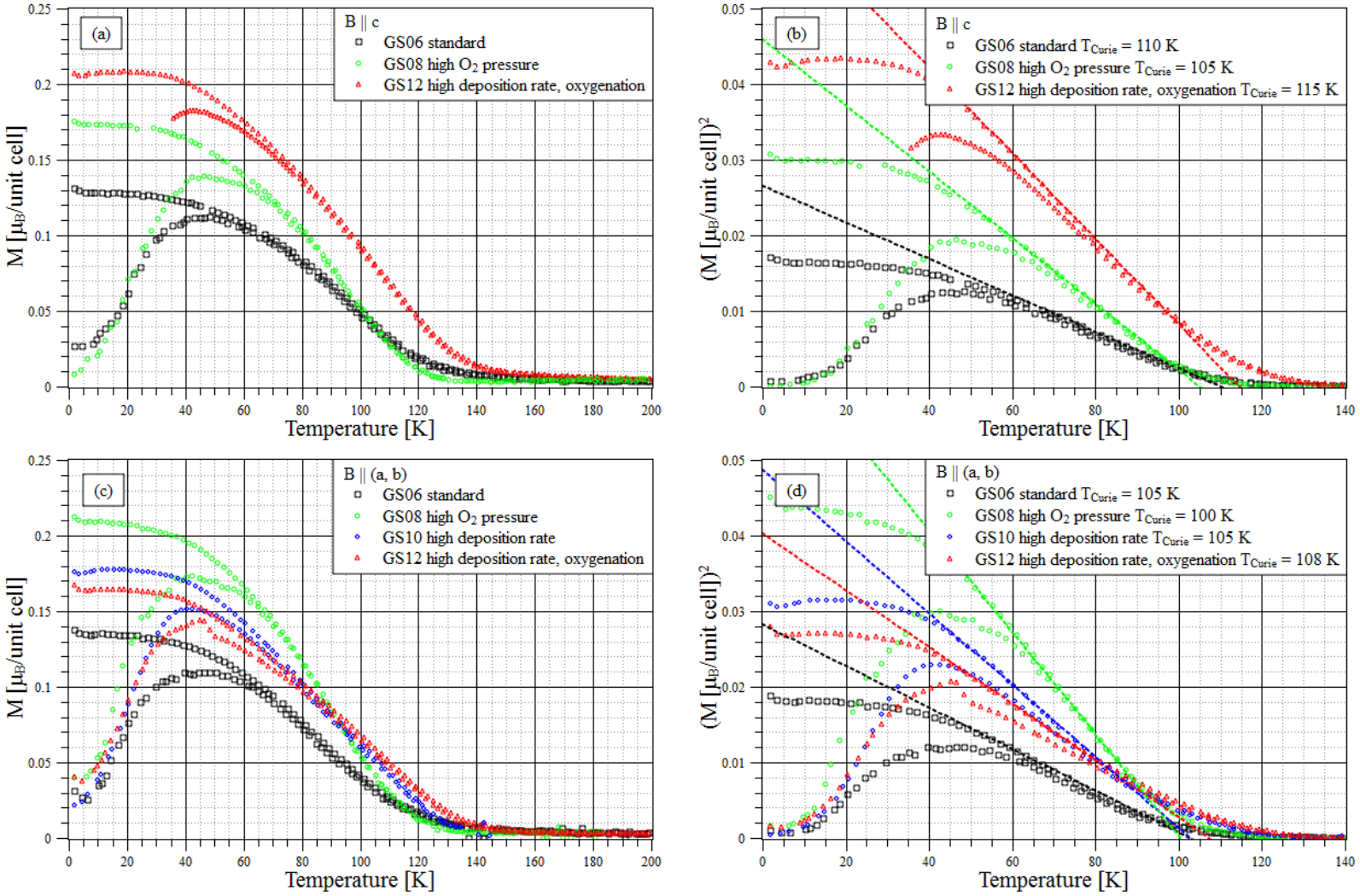

Figure 7.3. M(T) and $M^2(T)$ curves for out-of-plane (a, b) and in-plane (c, d) magnetic field orientations, 500 Oe. $M^2(T)$ curves are given with fits extrapolating linear part of the curves, crosses of the fits with $M^2(T) = 0$ axis correspond to T_{Curie} values.

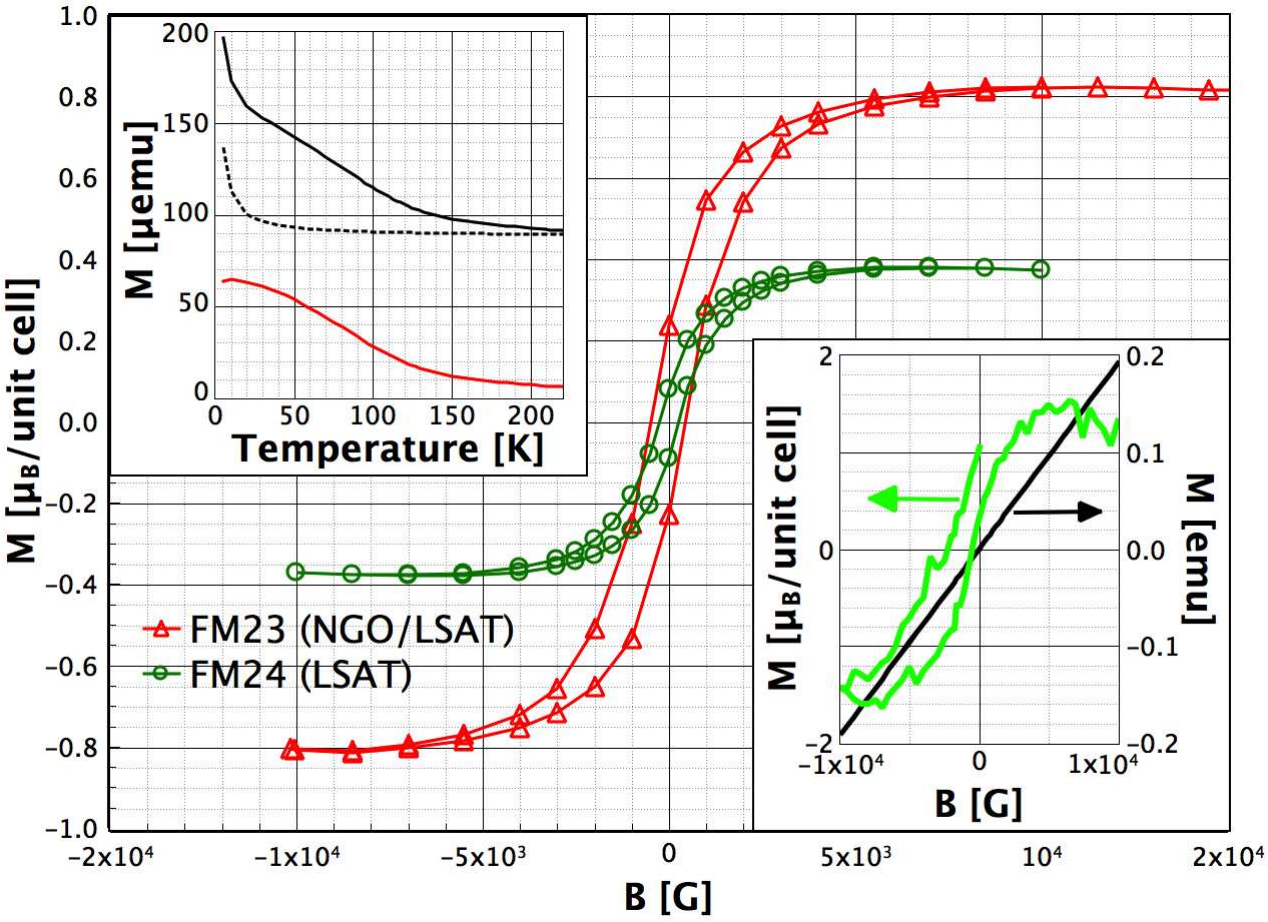

Figure 7.4. M(B) curves of the NBMO films on LSAT substrates with and without NGO buffer layer (5 K). Bottom inset: M(B) curves of the NBMO film on the NGO substrate, the film signal is masked by paramagnetic background of the substrate (straight line). Subtraction of background reveals a hysteresis curve (10 K). Top inset: M(T) dependence of the NBMO film on NGO/LSAT, paramagnetic part is fitted (dashed line) and subtracted, the curves are shifted for clarity. The magnetic field is parallel to the substrate plane for all measurements.

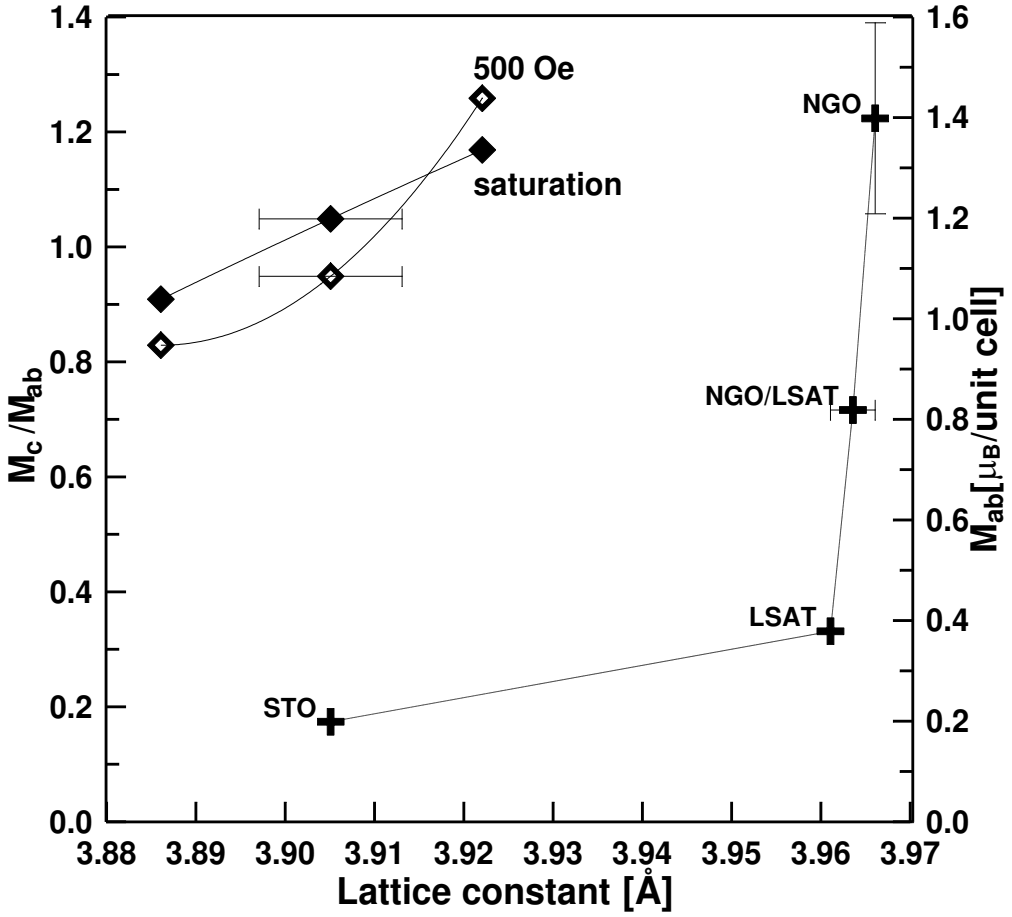

Figure 7.5. Correlation of structural and magnetic properties of the NBMO films. Crosses: dependence of in-plane magnetization in saturation on the NBMO out-of-plane lattice constant. Diamonds: magnetic anisotropy dependence on out-of-plane lattice constant of the NBMO films on STO substrates, open – at magnetic field of 500 Oe, closed – in saturation. All measurements made at 10 K. The lines are guides for the eye.

7.2 (NdBa)MnO_3 thin films on LSAT substrates: influence of thickness on magnetic and structural properties.

7.2.1 Experimental

The thin NBMO films of varying thickness (ranging from 100 to 1200 Å) were deposited on LSAT single crystal substrates. "Standard" deposition conditions for NBMO films were in use.

7.2.2 Results

The properties of the crystal structure of the films are summarized in Figure 7.6.

The lattice mismatch of LSAT (3.867 Å) and NBMO (3.886 Å) leads to in-plane compressive strain of - 0.5%, but for a reference sample on r-cut sapphire (effective lattice constant 3.51 Å), where due to too high mismatch of - 10.8% the film grows with no substrate influence, the measured *c*-lattice constant is 3.896 Å (for both (001) and (110) presented orientations). This value might be more relevant for the films rather than the bulk value, representing typical increase of lattice constants of films, comparing single crystals, due to defects incorporation.

In good agreement with in-plane compressive strain (and the structural results for our films on NGO substrates, where in compressive strain conditions a pseudomorphic growth with c-lattice constant increase was observed), all the films have *c*-lattice constants much larger than the bulk value. Using volume conservation of the unit cell ($(3.896\ Å)^3$) and the lattice constant of LSAT, we obtain c = 3.9547 Å, which matches exactly the values obtained for the thinnest films. With increasing thickness we observe some further increase of the lattice constant followed by a typical expected increase of the lattice constant variation (which is still showing very low values, < 0.6%). The thickness estimations are in good agreement with a constant deposition rate of 0.2 Å/pulse, except for the thickest sample.

All magnetization measurements were done with the magnetic field direction in the plane of the substrates. FC and ZFC measurements of magnetization versus temperature were performed at 1000 Oe. The significant paramagnetic background

of the LSAT substrate was extrapolated and removed, T_{Curie} were evaluated from the linear part of $M^2(T)$ curves (Figure 7.7, Figure 7.8). The dependence of T_{Curie} on the thickness is typical: with increase of the thickness the transition temperature increases as well:

100 Å – 70-75 K, 200 Å – 80 K, 600 Å – 100 K.

The saturated magnetic moment was examined by hysteresis curve measurements at several temperatures (Figure 7.9, several curves at 5 K). The data obtained for all the samples at 5 and 50 K are collected in Figure 7.10.

The saturated magnetic moments of the films show very interesting behavior: the normalized magnetic moment (in μ_B per unit cell) decreases rapidly with thickness. At 5 K this decay is clearly exponential. The thinnest sample reaches about 3.5 μ_B / unit cell, which is in a good agreement with the maximum moment possible for NBMO (3.5 μ_B/unit cell). The large uncertainty in the normalized magnetic moment for the thinnest samples is due to the uncertainty of the thickness estimation, which is used for normalization.

7.2.3 Discussion

An expansion of unit cell with thickness cannot be explained by the external strain effect – on the contrary we should expect strain relaxation as the film grows, resulting in some decrease of the lattice constant in the *c* direction [59]. Another possible explanation could be oxygen depletion of the film. If we have insufficient oxygen partial pressure during the deposition, the average oxygen content of the film would decrease with thickness, resulting in some expansion of the unit cell and deterioration of the magnetic properties of the film, due to lowering of the content of Mn^{4+} ions. Also, a decrease of the magnetic moment in the plane of the film with increase of the out-of-plane *c*-constant is in agreement with the previous results, where such distortion was followed by a rise in anisotropy of the magnetic properties, with the easy axis directed along the longest lattice constant.

In order to get some additional information on the role of oxygen, we checked the magnetic properties of the film of intermediate thickness (300 Å) after annealing in

air at 450 C for 2 hours. The resulting decrease of magnetic moment (about 14%) does not support our hypothesis, but it might be related to some other changes in the film during annealing, like the generation of defects on the A-site of the perovskite lattice.

7.2.4 Conclusions

A set of NBMO films of varying thickness was deposited by PLD on LSAT substrates, and the magnetic and structural properties of the films were investigated. Under bi-axial compressive strain conditions, the film grows with an increased *c*-lattice constant, as compared both with the bulk value and with that of the reference film on r-cut sapphire. The observed expansion of the *c*-lattice constant with thickness might be related to an oxygen deficiency during the deposition, and, as a consequence, a decrease of the average oxygen content of the film for thicker films. The dependence of the in-plane magnetic moment on the thickness shows an exponential decay, which might be driven both by an increased anisotropy and by an overall suppression of the magnetic properties, due to insufficient oxygenation.

7.3 The Use of NBMO for SC/FM bi-layers

The study of NBMO thin film depositions has shown that this material can be used for ferromagnetic layer in FM/HTS heterostructures. High quality of crystal structure, surface smoothness and chemical compatibility with ReBCO materials are the positive aspects of this material. The induced compressive strain, typical for ReBCO/NBMO heterostructures, enhances magnetic properties. The strong thickness effect on the magnetic properties is considered to be a negative aspect.

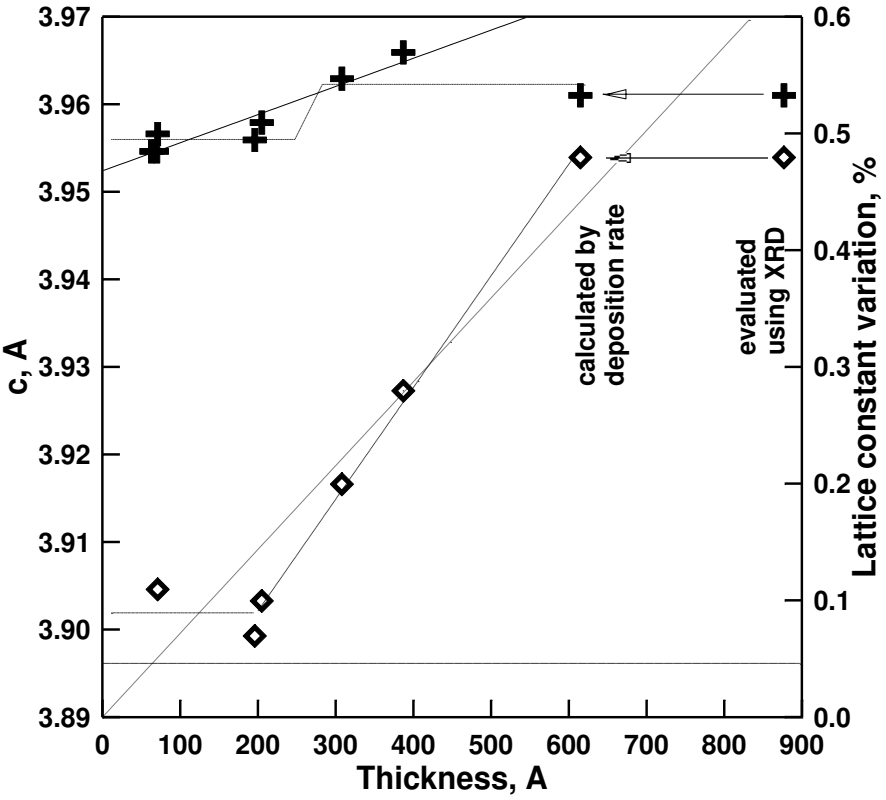

Figure 7.6. Structural properties of NBMO thin films, estimated from theta-2theta XRD measurements. Crosses correspond to lattice constant, diamonds to lattice constant variation respectively.

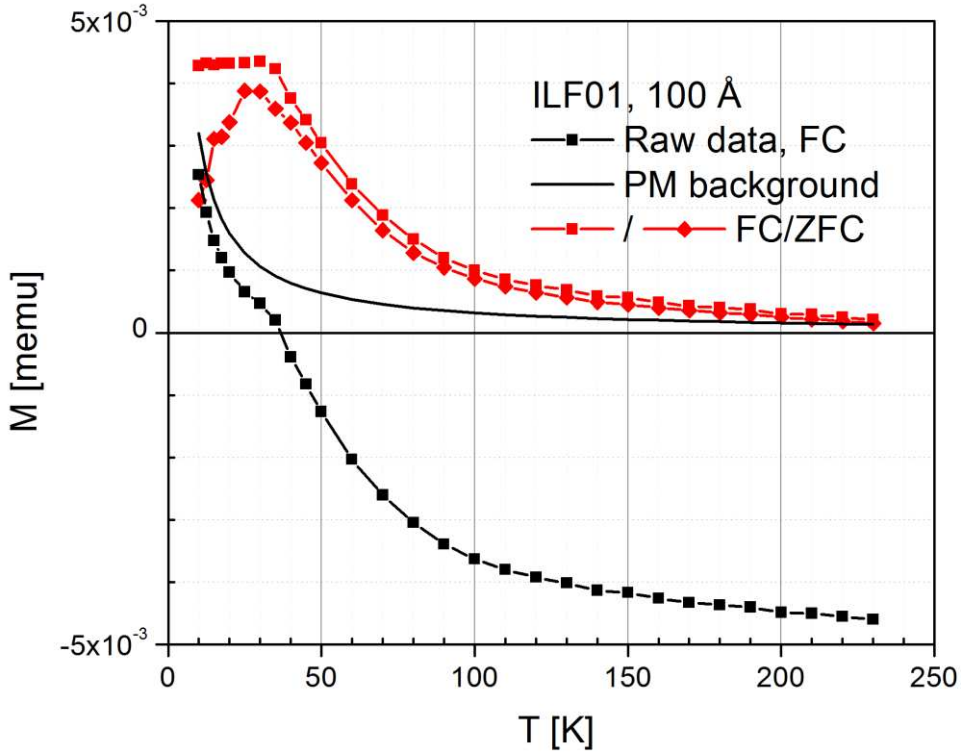

Figure 7.7. An example of FC-ZFC M(T) curves (red squares, red diamonds) after PM background removal. Extrapolated PM background (with zero shift, black line) and raw FC data (black line with squares) are given for comparison.

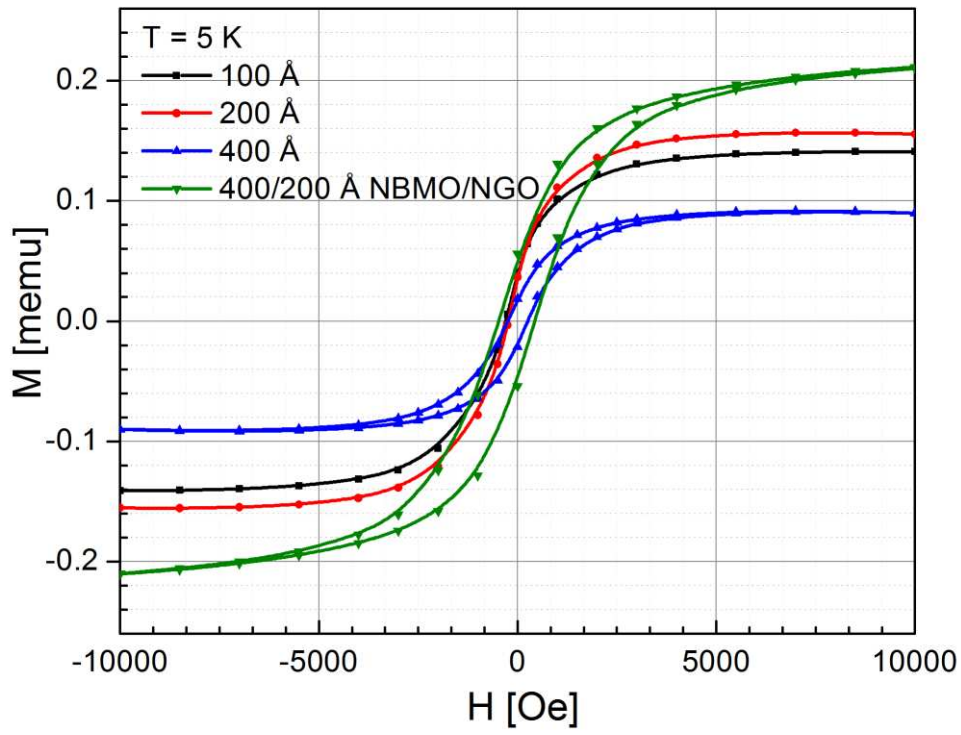

Figure 7.9. An example of hysteresis curves, 5 K, B || ab. Thinner films have higher overall magnetic moment than the thicker one, while the thick film on NGO buffer layer does not follow this trend.

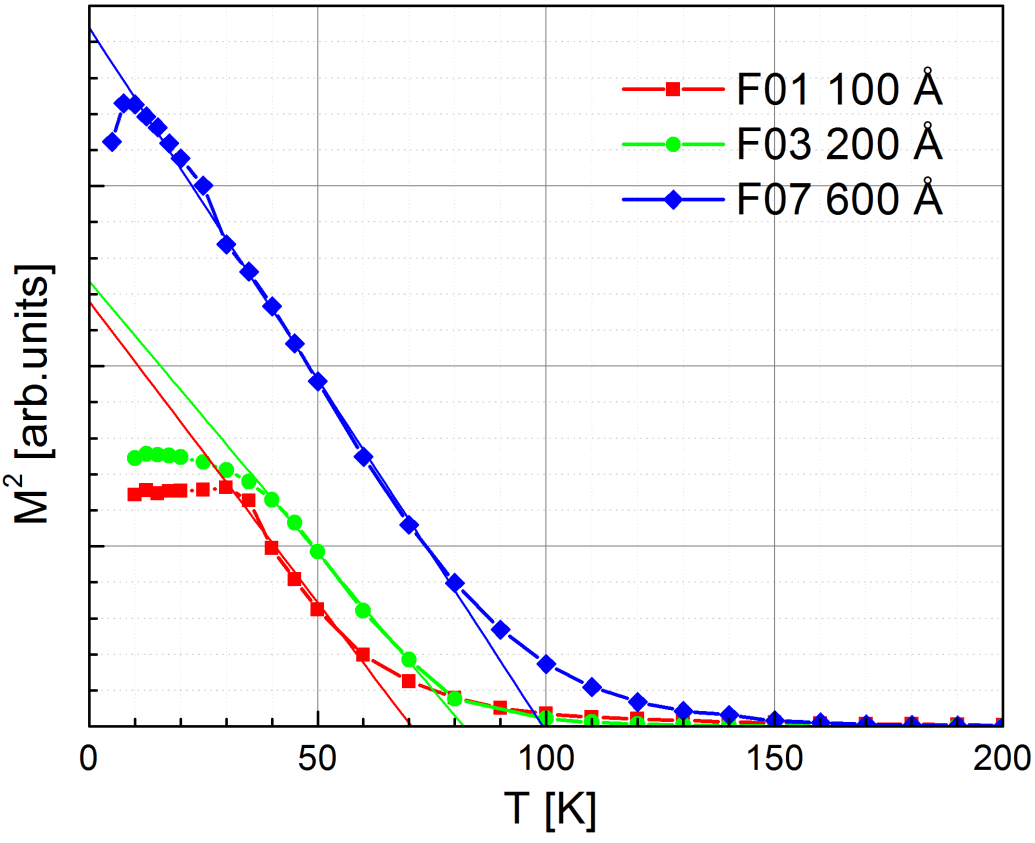

Figure 7.8. Estimation of T_{Curie} is performed by the linear part of $M^2(T)$ curves

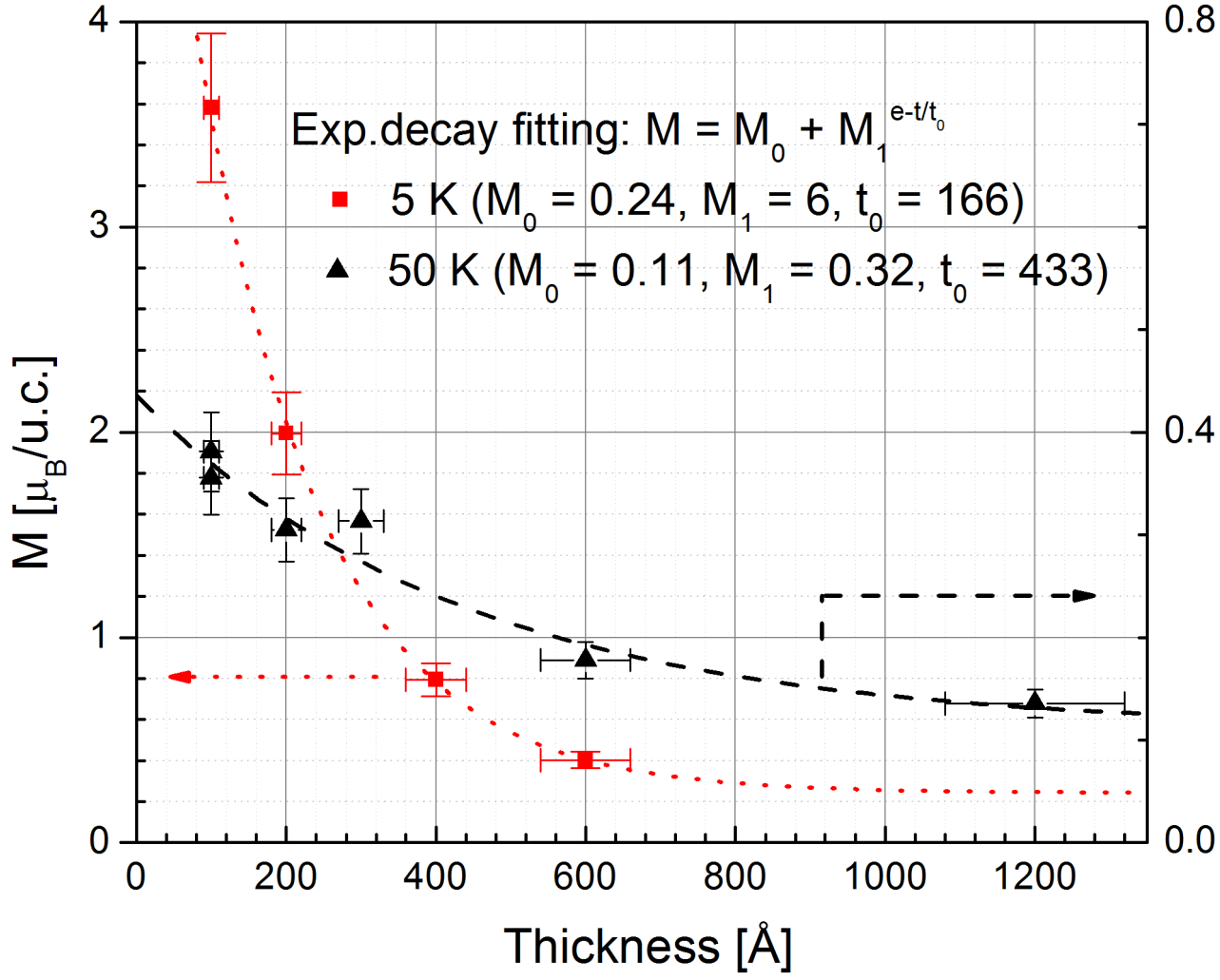

Figure 7.10. Saturated magnetic moment normalized per unit cell versus thickness of the film. 5 K (left scale, red), 50 K (right scale, black).

8 Cuprate-manganate bi-layers

Good lattice match as well as structural and compositional similarity of the NBMO manganate to the superconducting cuprates might be beneficial for the growth of high quality superconducting films. The NBMO-ReBCO layered structures are of interest for two reasons. First, studies of proximity effects require good interfaces between ferromagnetic and superconducting layers. Second, NBMO/ReBCO structures may be used for technical applications, such as tunable S/F filters, and even a possible use of NBMO as a buffer layer for coated conductors is under consideration.

The interest in the NBMO film as a buffer layer is inspired by the potential critical current enhancement in high magnetic fields, due to (1) an increase of pinning force of individual defects, and (2) magnetic field redistribution. This enhancement may take place in sufficiently high magnetic fields, while at low field the effect of the ferromagnetic buffer layer is negative, due to an increase of the magnetic field by the magnetized NBMO layer.

The NBMO layers were deposited under the deposition conditions optimal from the point of view of the crystal structure (650° C, 0.2 mBar, Ar/O_2 = 9.4/0.6, 1.5 J/cm^2, 2 Hz) – at low temperature, low oxygen partial pressure, with expected thickness about 120 nm. The YBCO layers were deposited using standard

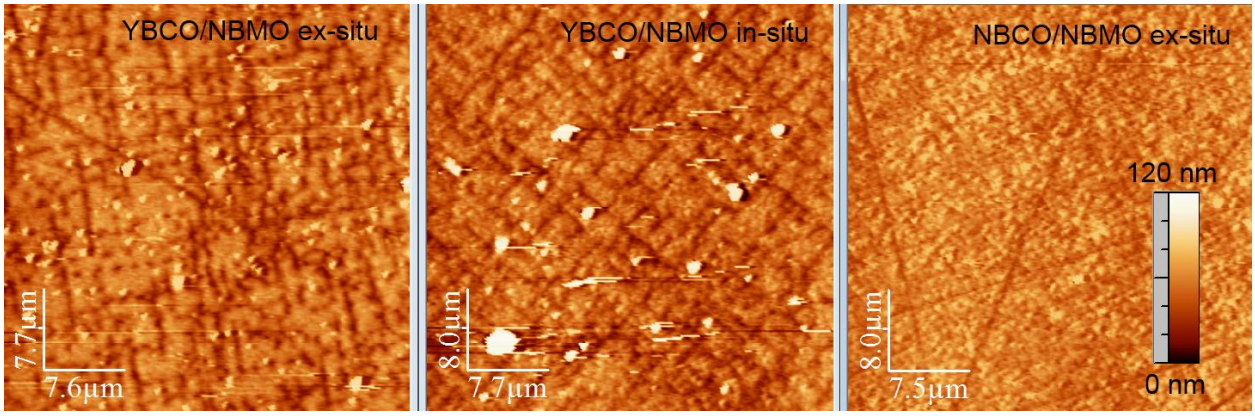

Figure 8.1.Tartan-like ordered cracks structure is present for ex-situ and in-situ deposited YBCO/NBMO bi-layers, while absent for NBCO/NBMO bi-layer film.

deposition conditions (750° C, 0.8 mBar, Ar/O_2 = 8/2, 1.5 J/cm^2, 2 Hz, 1 hour oxygenation in 450 mBar O_2 at 450° C), with an expected thickness of about 280 nm.

Straightforward combinations such as YBCO/NBMO/STO and NBMO/YBCO/STO were fabricated *ex-situ*. The first combination (superconducting layer on top) exhibited both ferromagnetic and superconductive behavior; the T_c (critical temperature) of an YBCO film on NBMO/STO was relatively high (89.6 K), higher than T_c of a reference film deposited in the same cycle on a bare STO substrate (87.5 K).

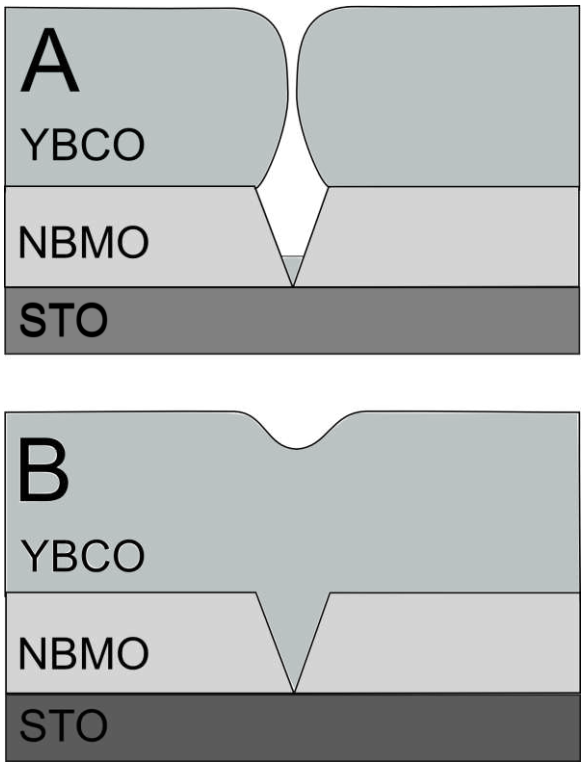

Figure 8.2. Schematic explanation of trenches formation. A – film overgrows the crack, B – film fills the crack.

AFM observations revealed a structure of ordered trenches on the surface of such bi-layer films, with a characteristic depth of about 30-40 nm and a 1-2 μm distance (see Figure 8.1). The probable origin of these trenches should be found in the oppositely directed strains induced into the NBMO layer by the underlying substrate and by the YBCO film growing on top. These trenches were not present in the NBMO layer before the YBCO deposition, and are reproducible for the bi-layers with YBCO layers of this thickness (280 nm), while such cracks are not observed for a 40 nm thick YBCO layer. The process of formation of trenches might be the following: at a certain characteristic thickness (definitely, more than 40 nm) of the growing YBCO film the underlying NBMO layer releases the strain by cracking along the crystallographic axes. The resulting cracks might be partly overgrown (Figure 8.1, A) or filled (Figure 8.2, B) by the subsequent deposited YBCO layer, and, as a result, we see these relatively shallow trenches or even pores arranged in lines on the surface of the YBCO layer. A SEM

micrograph of such a film and EDAX spectra from a spot close to the trench and from a spot within the smooth film area are shown in Figure 8.4. This instrument is different from the one used for EDAX analysis in the Chapter 6, and does not allow changes of the beam energy, which is fixed by an accelerating voltage as high as 15.0 kV. This factor makes the method even less quantitative for the study of thin films, so only a comparison of relative values makes sense. As expected from the geometry depicted in Figure 8.2 "A", we get an estimation of lower Y and Cu, and higher Nd and Mn contents from the trench, than from the clean film area.

Surprisingly, an *in-situ* deposition of YBCO/NBMO on STO resulted in a YBCO film with lower T_c (87 K), while the morphology (Figure 8.1) and the crystal structure of the films are unchanged. This must be an effect of oxygenation, due to a "cancelation" layer of NBMO film, which is formed by exposure to the atmosphere for *ex-situ* grown bilayers (and not formed for *in-situ* grown samples). This "cancelation" layer might act as a barrier for oxygen diffusion and thus protect the growing YBCO film from being depleted of oxygen.

The second combination (FM layer on top) resulted in the suppression of the superconductive properties of the YBCO layer by the deposition of the NBMO layer (T_c was 87.5 K before NBMO deposition and below 80 K afterwards). The superconducting film loses oxygen during the NBMO film deposition at 650° C and it does not recover the oxygen contents after an additional oxygenation.

The $Nd_1Ba_2Cu_3O_x$/NBMO bi-layer structure seems to be more promising than $Y_1Ba_2Cu_3O_x$/NBMO (but harder to produce) for obtaining smoother interfaces, which are important for applications. A test deposition of such a bi-layer gave relatively low T_c of about 83 K due to non-optimal deposition conditions; so several optimization cycles are required. The morphology of the film (the thickness of the superconducting layer is about 120 nm) is different from YBCO/NBMO bi-layers, the surface is smooth and no trenches can be observed (Figure 8.1, right). It is worth noting that in the same way as for YBCO depositions, a reference sample of NBCO on a bare substrate gave inferior results (T_c below 80 K).

This bi-layer was examined for its magnetic properties on a SQUID magnetometer using the in-plane geometry, in order to minimize the superconducting input. The resulting hysteresis curve proves the ferromagnetic ordering of the NBMO films in bi-layers (Figure 8.3).

The superconducting properties of YBCO/NBMO bi-layers were tested by magnetization measurements on a VSM, the results are shown in comparison with other results (of 25% Y-doped sample, sample grown on Y_2O_3 template layer, standard YBCO film) in Figure 9.1, and Figure 9.2. While at 77 K the bi-layer shows the lowest critical current densities (lower than the standard sample), with decreasing temperature it starts showing some improvement of the J_c, approaching the results of the YBCO film on yttria nanoparticles.

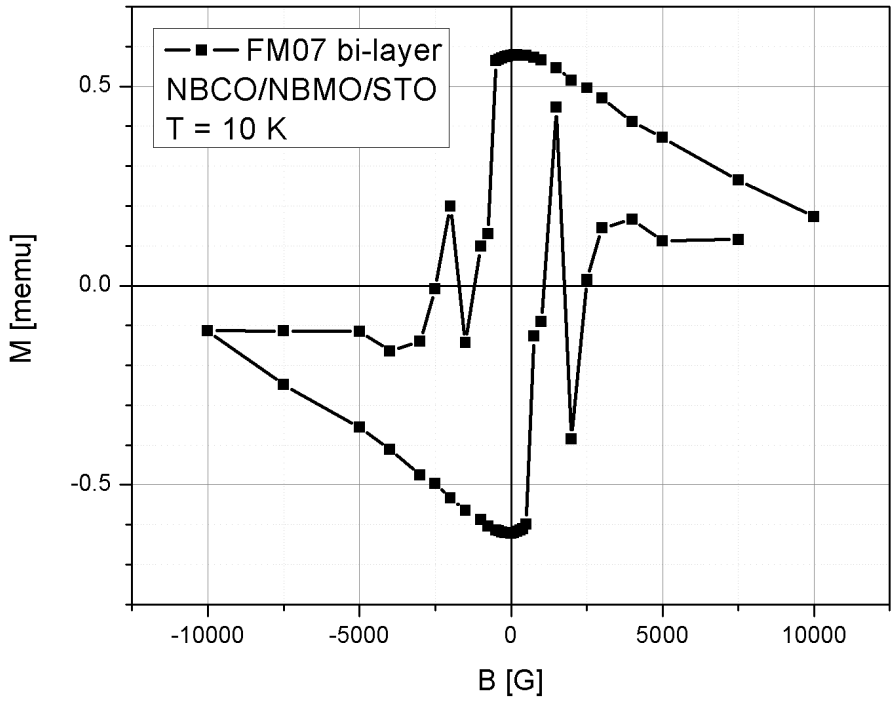

Figure 8.3. Hysteresis curve of NBCO/NBMO bi-layer, at 10 K in the in-plane geometry

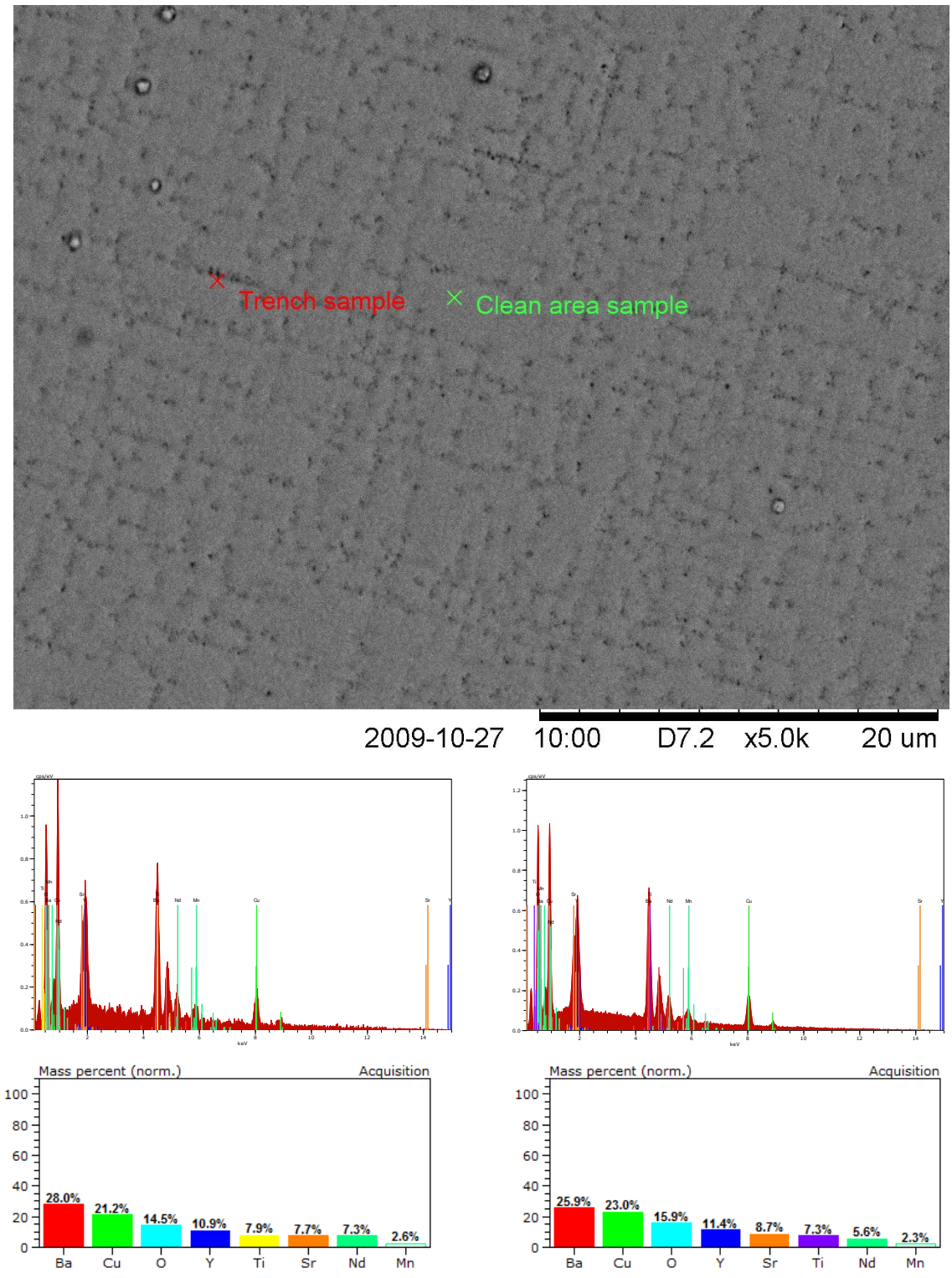

Figure 8.4. SEM micrograph and EDAX spectra of a spot close to the trench (left side) and a spot in the smooth film area (right side) for an YBCO/NBMO bi-layer, deposited on a STO substrate ex-situ

9 Comparison of the best J_c results

Aggregate plots of critical current densities for a variety of samples: 600 nm thick YBCO film with excess of yttria (deposited from $Y_{1.25}Ba_2Cu_3O_x$ target), standard thin (140 – 320 nm) films deposited on yttria nanoparticles template layer, on (NdBa)MnO_3 buffer layer and on a bare substrate, are given in Figure 9.1; the corresponding volume pinning force plots are given in Figure 9.2.

The properties of the film on the NBMO buffer layer show a crossover behavior with the properties of the reference YBCO film. While having somewhat lower J_c at 77 K, at lower temperatures it is improved by 30-50%. This improvement might be related to the influence of the magnetic layer (by redistribution of the magnetic flux or existed pinning sites enhancement) or to the numerous dislocations in the YBCO film formed due to strained growth conditions (which even results in the film cracking during the growth).

The yttria nanoparticles of the template layer are known to induce the formation of dense dislocations in the film, resulting in a significant (2-3x) increase of the critical current densities at 50-77 K and in high magnetic fields. At lower temperatures these dislocations, since they are small, do not produce pinning potentials sufficiently deep and sharp for strong improvement of the critical current density.

The highest J_c through the whole range of temperature and magnetic field was obtained for Y-rich films deposited from $Y_{1.25}Ba_2Cu_3O_x$ target with low deposition rate (0.7 Å/s). At 77 K and magnetic fields above 2 Tesla it exhibits an order of magnitude increase of the critical current densities as compared to a reference high quality YBCO film, deposited from the stoichiometric target. The same picture is correct for 50 K, the current density at 8.5 T is as high as 1 MA/cm^2. At 20 K this sample shows higher J_c than the reference sample at 5 K.

The maxima of the pinning force behave different for different samples (Figure 9.2). For the bi-layer and reference standard film the maximum is observed at 0.5 T (77 K), at lower temperature it moves to the higher fields, at 5 K it is above 15 T.

The picture is similar for the film grown on the yttria template layer, where the maximum is also shifted to higher fields (about 1 T at 77 K). The Y-rich film exhibits the pinning force maximum at about 2 T for 77 K, and with decreasing temperature it moves to 5 T for 50 K, and only 6-7 T for 5-20 K.

We may make an estimate of the matching field for Y-rich samples basing on the EDAX measurements (6.5 vol.% excess yttria in the YBCO grains) and the size of yttria crystallites evaluated from XRD data analysis (11-14 nm). These numbers give the particle density of $9 \cdot 10^{10}$ cm^{-2} for each 100 nm of the sample thickness (that corresponds to 1.8 T), and one could expect the increase of the matching field with thickness. We do not observe this effect for two 400 and 600 nm thick samples, which have almost the same J_c profile, but the explanation seems to be obvious. For a 100 nm thick layer such yttria inclusions, if been evenly distributed, cover 10% of the area of the film. That gives 40% for 400 nm thickness, so we may hardly expect a clear individual pinning at this point, instead, a pinning of a single vortex by multiple defects becomes probable. For making any final conclusions, a cross-sectional TEM study is necessary (and currently is in progress).

The comparison of the pinning force data for the best low deposition rate (0.7 Å/s) Y-rich films with the data for Y-rich films deposited at standard deposition rate (1.4 Å/s) is of interest (Figure 9.3). Another difference is the thickness of the films. With decrease of the deposition rate we expect an increase of yttria inclusions size and regularity, and decrease of their density. Thus, at 77 K bigger inclusions of thick low deposition rate film provide stronger pinning, and due to higher thickness of this film (and, consequently, area density of defects) the maximum pinning force occurred at higher magnetic field. At lower temperatures and high (9-10 T) magnetic fields a crossover of the pinning force values takes place: smaller but more numerous inclusions produce higher overall pinning force. The deposition rate seems to be yet another parameter allowing us to tune the film properties.

Double logarithmic plots of normalized J_c at 5 and 50 K are given in Figure 9.4. The linear parts of these plots represent the regions where the field dependence of

J_c may be described by a power law: $J_c \propto B^{\alpha}$; the corresponding values of the α coefficient are collected in the Table 9.1. While the standard film and the bi-layer have the similar values of about -0.5 at both 5 and 50 K, the film on the template layer has a higher value at 50 K (-0.34) which changes to the standard -0.5 at 5 K; the Y-rich film has the power law exponent almost independent on temperatures of about -0.2. This value is very high and might involve some mechanism of pinning force enhancement with increase of the applied field (like suppression of superconductivity in the areas close to the yttria inclusions).

Sample	50 K	5 K
Y-doped (1.25)	-0.20	-0.23
Y2O3 template	-0.34	-0.49
NBMO buffer	-0.52	-0.48
Standard film	-0.43	-0.46

Table 9.1. Power law exponents for various samples at 5 and 50 K

Finally, a comparison with other high-J_c films of two scientific teams working with popular $BaZrO_3$ artificial pinning centers is given in Figure 9.5. The results [60] marked with (1) in the plot legend were achieved for 3 μm thick BZO-doped YBCO film, the results marked with (2) for 200 nm ([61], 5-50 K) and 1.25 μm ([62], 65-77 K) thick BZO-doped YBCO films, deposited from a nanocrystalline target. Our results for 600 nm thick Y-rich film are marked (3).

As we can see, the Y_2O_3 inclusions allow us to reach the same or even better current-carrying capabilities as compared with the optimal level of BZO doping. We must note that no special optimization to find the optimal level of YBCO target doping (with Y), as well as the deposition conditions for Y-rich films growth, was carried out. These factors leave room for further research and improvements in this field.

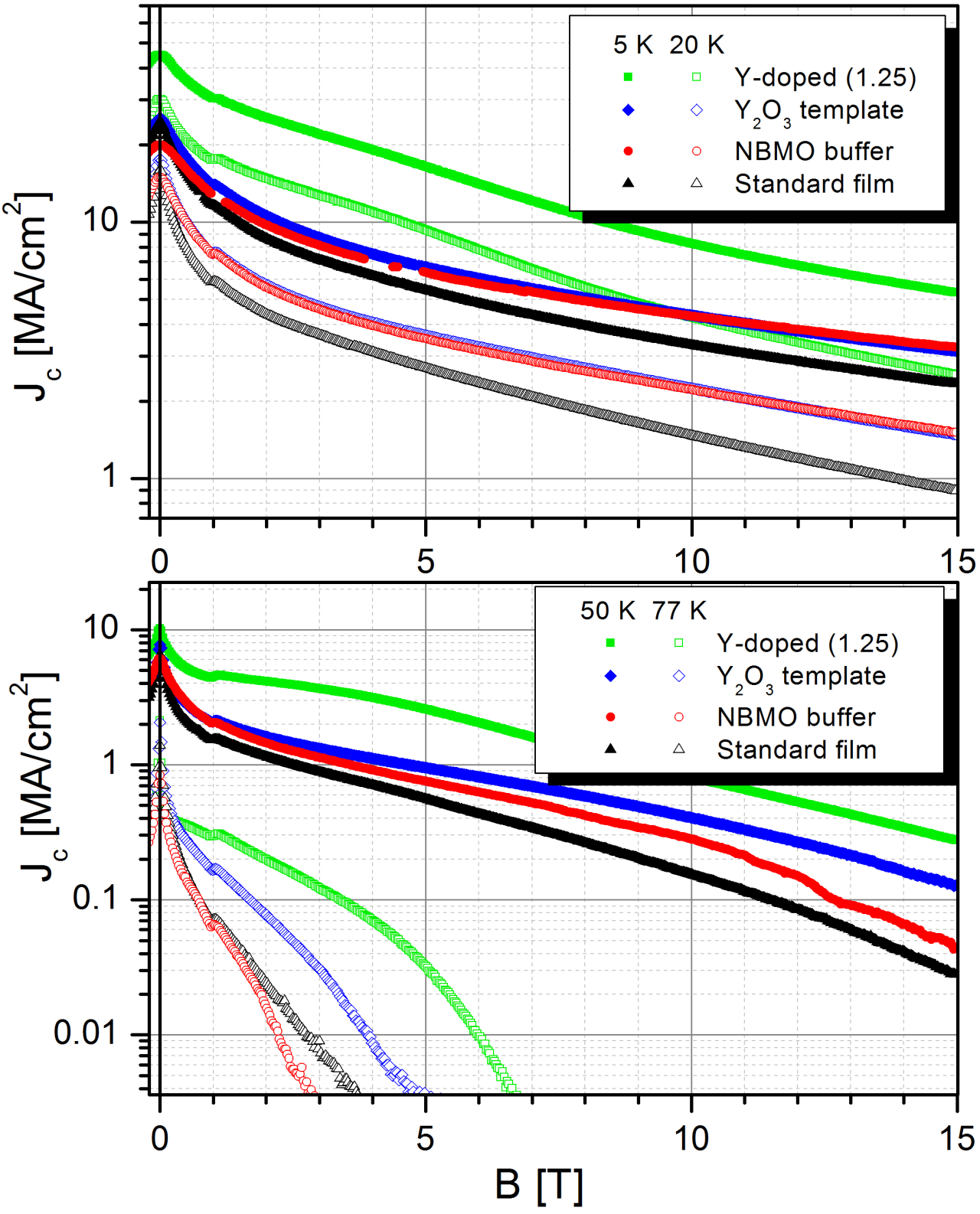

Figure 9.1 Comparison of the best films (thick Y-doped, on yttria template layer, on NBMO buffer layer) with the standard thin stoichiometric film. 5, 20, 50, 77 K

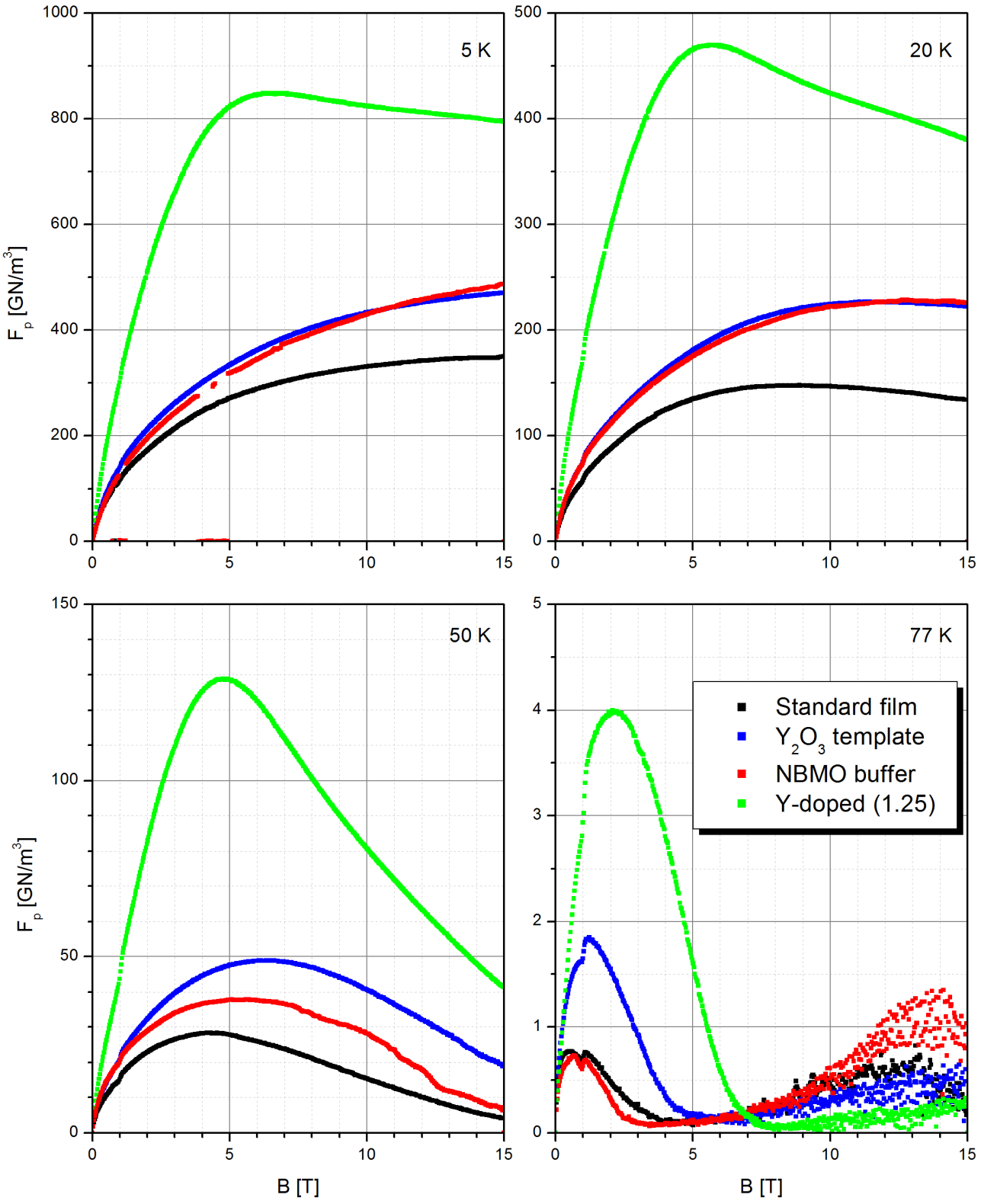

Figure 9.2. Pinning force per unit volume of the films at 5, 20, 50 and 77 K.

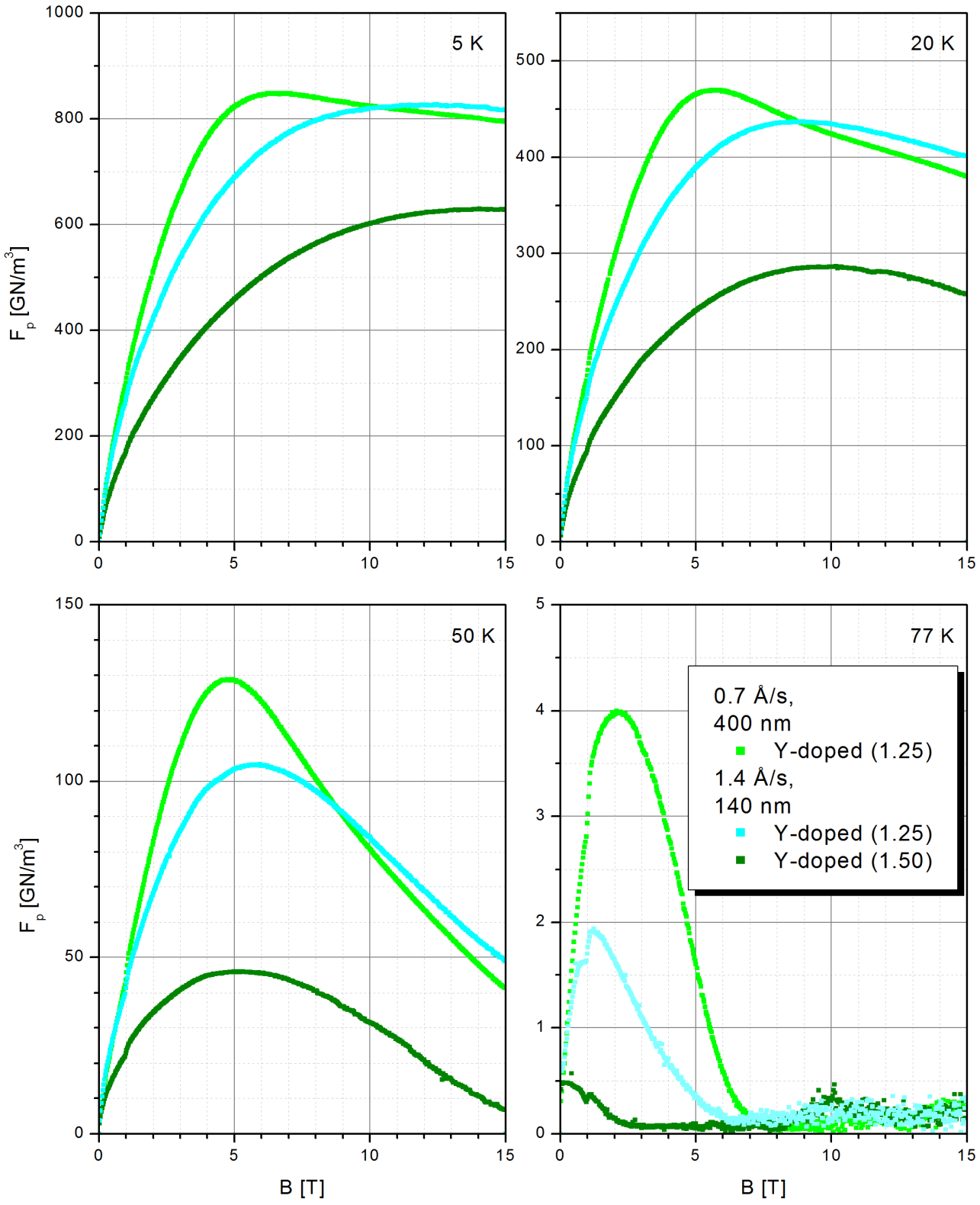

Figure 9.3. Pinning force per unit volume of the Y-rich films at 5, 20, 50 and 77 K.

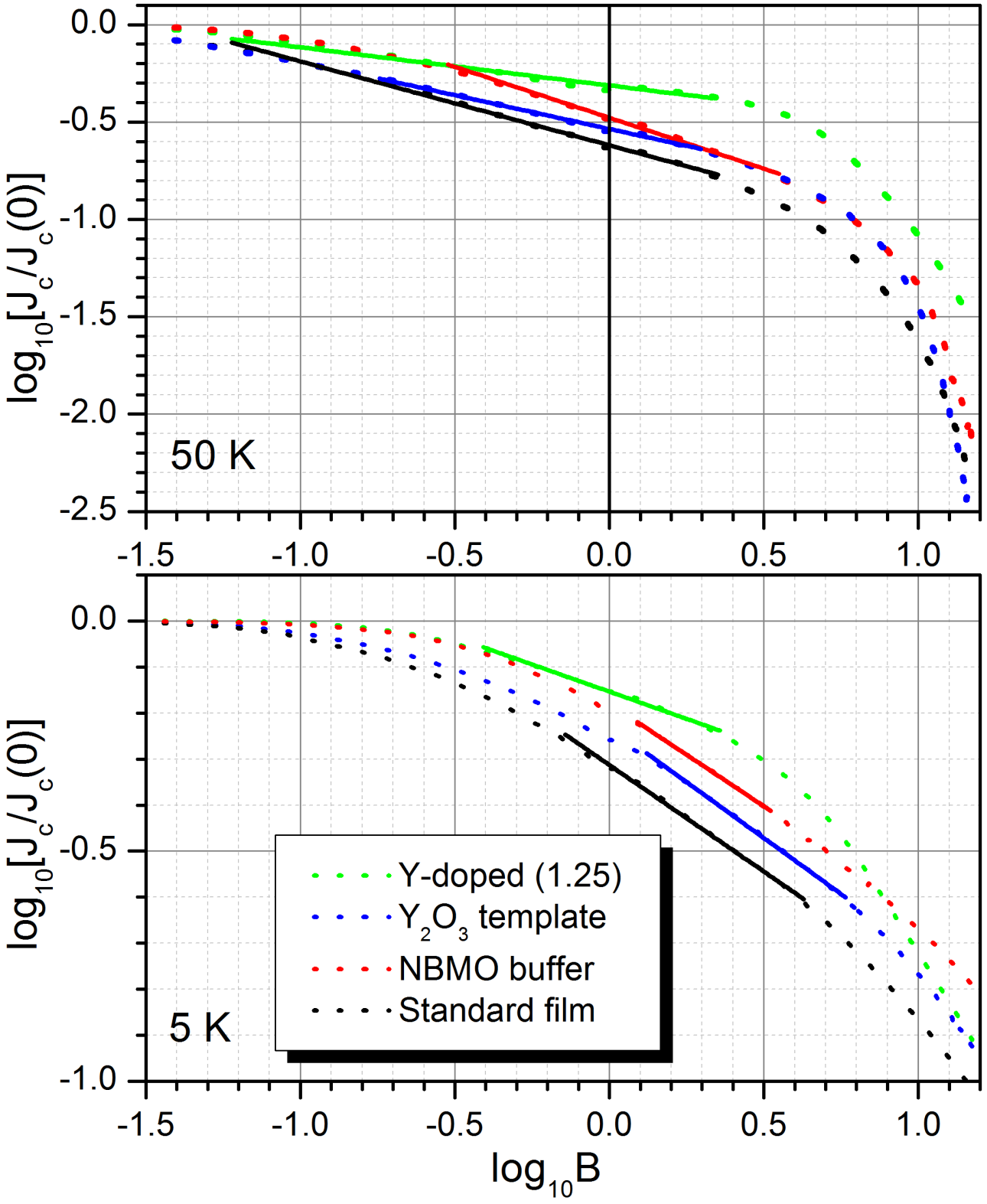

Figure 9.4. Double logarithmic plots of J_c of different films at 5, 50 K.

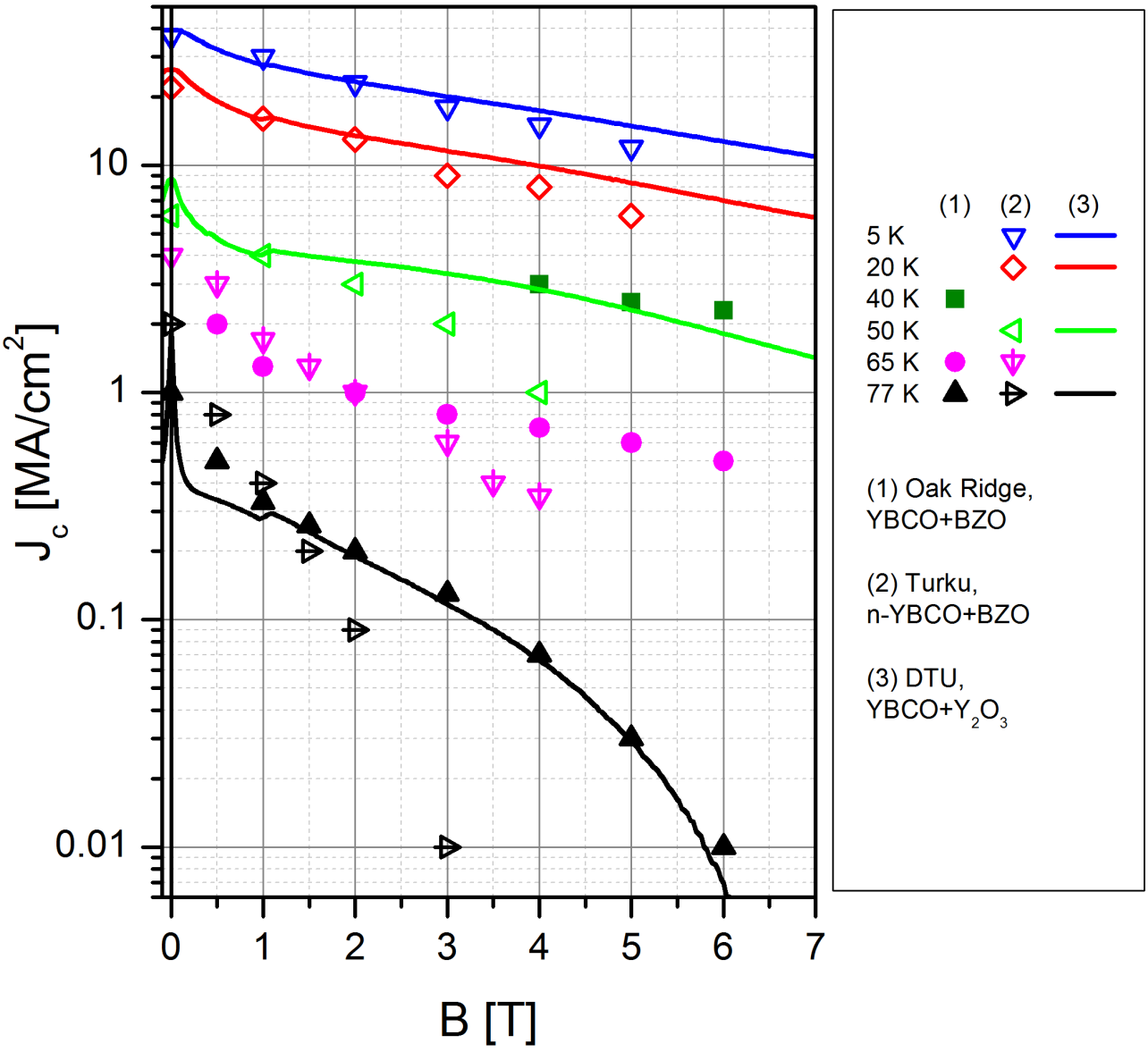

Figure 9.5. Critical current densities of the 600 nm thick Y-rich film in comparison with results for $BaZrO_3$-doped films, (1) - [60], *(2)* - [61], [62].

10 Conclusions

10.1 Results

A transfer of the element composition to the YBCO thin film was investigated for different target compositions, the preferential effect of yttrium contents in the target on the resulting film composition was found. High quality epitaxial yttrium-rich YBCO films were fabricated using direct doping of the target, which is beneficial comparing with the often used composite targets due to better homogeneity of the resulting film.

It was first observed that Y-rich films do not have the tendency of substitution of *c*-orientation by *a*-orientation with increasing thickness. Coherent yttria inclusions provide an effective strain relaxation mechanism, thus thick (more than 0.5 □m thick) *c*-oriented YBCO films of high superconducting and structural properties may be grown. By varying the deposition rate it is possible to tune the yttria segregation process and improve the superconducting properties of the resulting films. The strong improvement of the critical current density of YBCO films in high fields by embedding yttria inclusions into superconducting matrix is comparable with the best results obtained by other methods, like BZO doping. We report J_c(5 T, 77 K) = 30 kA/cm^2, J_c(5 T, 50 K) = 2.3 MA/cm^2; at 50 K the J_c reaches 1 MA/cm^2 in a magnetic field as high as 8.5 Tesla. These high critical current densities allow the implementation of the yttrium-enriched films in technical applications for motors and generators (after a transfer to commercial production technology for long tapes).

A process of yttria nanoparticles formation by the PLD deposition method was studied; a template layer of yttria nanoparticles was successfully utilized for fabrication of YBCO films with significantly improved pinning characteristics. The main improvement of the critical current density of the films on template layers is achieved at high temperature (77 K).

(NdBa)MnO_3 films were for the first time fabricated by a physical deposition method. The influence of deposition parameters, the substrate induced strain and

the film thickness on the structural and magnetic properties was systematically studied. A strong correlation of the structural distortions with the magnetic anisotropy was revealed. An unusual exponential decay of magnetic moment with a growth of the film thickness was observed.

ReBCO/(NdBa)MnO_3 bi-layer structures were fabricated, the superconducting, magnetic and structural properties were studied. The critical current density of the obtained bi-layer structures showed significant improvement over the reference HTSC sample in high magnetic fields.

10.2 Importance

The proposed methods to increase the critical current density are very promising for coated conductors fabrication. High critical current densities of Y-doped films in high magnetic fields are important for the applications of SC tapes in rotary machines. Optimizations of the Y-doping level and the deposition parameters for that level should be carried out and will lead to further improvement of the current-carrying capabilities of Y-doped films. The suppression of the tendency to *a*-orientation preferential growth with an increase of the film thickness allows the fabrication of high quality thick films.

High quality ferromagnetic NBMO films may be used for the fabrication of SC/FM multilayers based only on metal oxides (cuprates and manganates, respectively). The study of external strain and deposition conditions effects of NBMO is important for further applications of the material and supplements an overall picture of rare-earth manganates properties. Good compatibility of NBMO with NBCO high temperature superconductor makes this pair of materials excellent candidates for the fabrication of multilayer structures and devices on this base, such as tunable filters, π-contacts and superconducting switches. Furthermore, NBMO might be utilized as a buffer layer for ReBCO based coated conductors for improvement of their current-carrying capabilities.

Literature

[1] A.A. Abrikosov, “On the magnetic properties of superconductors of the second group,” *Soviet Phys. JETP*, vol. 5, 1957, pp. 1174-1183.

[2] E.H. Brandt, “The flux-line lattice in superconductors,” *Quantum*, vol. 58, 1995, pp. 1465-1594.

[3] D. Nelson and V. Vinokur, “Boson localization and correlated pinning of superconducting vortex arrays.,” *Physical review. B, Condensed matter*, vol. 48, Nov. 1993, pp. 13060-13097.

[4] K. Matsumoto and P. Mele, “Artificial pinning center technology to enhance vortex pinning in YBCO coated conductors,” *Superconductor Science and Technology*, vol. 23, Jan. 2010, p. 014001.

[5] R.M. Scanlan, A.P. Malozemoff, and D.C. Larbalestier, “Superconducting materials for large scale applications,” *Proceedings of the IEEE*, vol. 92, Oct. 2004, pp. 1639-1654.

[6] J.G. Bednorz and K.A. Miiller, “Possible High T_c Superconductivity in the BaLaCuO System,” *Phys.B*, vol. 193, 1986, pp. 189-193.

[7] J.L. Routbort and S.J. Rothman, “Oxygen diffusion in cuprate superconductors,” *Journal of Applied Physics*, vol. 76, 1994, p. 5615.

[8] C. Namgung, J. Irvine, J. Binks, and A. West, “Orthorhombic-tetragonal transition in $YBa_2Cu_3O_x$,” *Superconductor Science and Technology*, vol. 1, 1988, p. 169.

[9] Scheel, “Materials engineering problems in crystal growth and epitaxy of cuprate superconductors,” *MRS Bulletin*, vol. 19, 1994, pp. 26-32.

[10] N. Takezawa and K. Fukushima, “Optimal size of an insulating inclusion acting as a pinning center for magnetic flux in superconductors: Calculation of pinning force,” *Physica C*, vol. 290, 1997, pp. 31-37.

[11] L. Civale, “Vortex pinning and creep in high-temperature superconductors with columnar defects,” *Superconductor Science and Technology*, vol. 10, 1997, p. A11.

[12] N. Harada, H. Yamada, K. Sugai, I. Munechika, M. Tsuda, and T. Hamajima, “Flux pinning property of artificial pinning center introduced by microfabrication,” *Physica C: Superconductivity*, vol. 392-396, 2003, pp. 1043-1047.

[13] J. Lin, M. Gurvitch, S. Tolpygo, A. Bourdillon, S. Hou, and J. Phillips, “Flux pinning in $YaBa_2Cu_3O_{7-\delta}$ thin films with ordered arrays of columnar defects,” *Physical Review B*, vol. 54, Nov. 1996, p. R12717-R12720.

[14] J. Huijbregtse, B. Dam, R. van der Geest, F. Klaassen, R. Elberse, J. Rector, and R. Griessen, "Natural strong pinning sites in laser-ablated $YaBa_2Cu_3O_{7-\delta}$ thin films," *Physical Review B*, vol. 62, Jul. 2000, pp. 1338-1349.

[15] K. Matsumoto, T. Horidea, K. Osamuraa, M. Mukaidab, Y. Yoshidac, and F. Ataru Ichinosed, f and Shigeru Horiie, "Enhancement of critical current density of YBCO films by introduction of artificial pinning centers due to the distributed nano-scaled Y_2O_3 islands on substrates," *Physica C: Superconductivity*, vol. 412-414, Oct. 2004, pp. 1267-1271.

[16] M. Peurla, H. Huhtinen, P. Paturi, Y.P. Stepanov, J. Raittila, and R. Laiho, "YBCO Films Prepared by PLD Using Nanocrystalline Targets Doped With $BaZrO_3$ or Y211," *IEEE Transactions on Appiled Superconductivity*, vol. 15, Jun. 2005, pp. 3050-3053.

[17] C. Cai, J. Zhang, Y. Lu, R. Hühne, and B. Holzapfel, "Artificial Nano-Scale Precipitates for Flux Pinning in $YBa_2Cu_3O_{7-\delta}$ Thin Films and Coated Conductors," *Materials Science Forum*, vol. 546-549, 2007, pp. 1865-1870.

[18] R. Cloots, T. Koutzarova, J.-P. Mathieu, and M. Ausloos, "From RE-211 to RE-123. How to control the final microstructure of superconducting single-domains," *Superconductor Science and Technology*, vol. 18, Mar. 2005, p. R9-R23.

[19] T.I. Selinder, U. Helmersson, Z. Han, and L.R. Wallenberg, "Structural characterization of yttria (Y_2O_3) inclusions in $YBa_2Cu_3O_{7-x}$ films: Growth model and effect on critical current density," *Thin Solid Films*, vol. 229, May. 1993, pp. 237-248.

[20] M. Muralidhar, H. Chauhan, T. Saitoh, K. Kamada, K. Segawa, and M. Murakami, "Effect of mixing three rare-earth elements on the superconducting properties of," *Superconductor Science and Technology*, vol. 10, 1997, p. 663.

[21] P. Malozemoff, S. Annavarapu, L. Fritzemeier, Q. Li, V. Prunier, M. Rupich, C. Thieme, W. Zhang, a Goyal, M. Paranthaman, and D.F. Lee, "Low-cost YBCO coated conductor technology," *Superconductor Science and Technology*, vol. 13, May. 2000, pp. 473-476.

[22] V. Selvamanickam, "Fabrication of 100 A class, 1 m long coated conductor tapes by metal organic chemical vapor deposition and pulsed laser deposition," *Physica C: Superconductivity*, vol. 392-396, Oct. 2003, pp. 859-862.

[23] O. Moran, E. Baca, and F. Perez, "Depression of the superconducting critical temperature and finite-size scaling relation in $YaBa_2Cu_3O_{7-\delta}$ /$La_{2/3}Ca_{1/3}MnO_3$ bilayers," *Microelectronics Journal*, vol. 39, 2008, pp. 556-559.

[24] A. Buzdin, "Proximity effects in superconductor-ferromagnet heterostructures," *Reviews of Modern Physics*, vol. 77, Sep. 2005, pp. 935-976.

[25] S. Piano, De Santis, F. Bobba, F. Giubileo, M. Longobardi, Di Bartolomeo, M. Polichetti, a Scarfato, D. Zola, a Vecchione, and a M. Cucolo, "Structural, electrical and magnetic

characterization of artificial ferromagnetic/superconducting ($La_{0.7}Ca_{0.3}MnO_3/YBa_2Cu_3O_{7-x}$) heterostructures," *Journal of Physics: Condensed Matter*, vol. 21, 2009, p. 254205.

[26] A. Goldman, "Cuprate/manganite heterostructures," *Journal of Magnetism and Magnetic Materials*, vol. 200, Oct. 1999, pp. 69-82.

[27] Y. Ichino, K. Sudoh, K. Miyachi, Y. Yoshida, and Y. Takai, "Orientation Mechanism of $ReBa_2Cu_3O_y$ (Re = Nd, Sm, Gd, Y, Yb) Thin Films Prepared by Pulsed," *Thin Films*, vol. 13, 2003, pp. 2735-2738.

[28] T. Nakajima, "Structures and electromagnetic properties of the A-site disordered Ba-based manganites; $R_{0.5}Ba_{0.5}MnO3$ (R = Y and rare earth elements)," *Journal of Alloys and Compounds*, vol. 383, 2004, pp. 135-139.

[29] Wollan, "Neutron diffraction study of the magnetic properties of the series of perovskite-type compounds $[La_{(1-x)},Ca_x]MnO_3$," *Physical Review*, vol. 100, 1955, pp. 545-563.

[30] de Gennes, "Effects of double exchange in magnetic crystals," *Physical Review*, vol. 118, 1960, pp. 141-154.

[31] P.W. Anderson, "Considerations on double exchange," *Physical Review*, vol. 100, 1955, pp. 675-681.

[32] Y.M. Xiong, G.Y. Wang, X.G. Luo, C.H. Wang, X.H. Chen, X. Chen, and C.L. Chen, "Magnetotransport properties in $La_{1-x}Ca_xMnO_3$ (x=0.33, 0.5) thin films deposited on different substrates," *Journal of Applied Physics*, vol. 97, 2005, p. 083909.

[33] A. Arulraj, A. Biswas, A. Raychaudhuri, C. Rao, P. Woodward, T. Vogt, D. Cox, and A. Cheetham, "Reentrant transition from an incipient charge-ordered state to a ferromagnetic metallic state in a rare-earth manganate," *Physical Review B*, vol. 57, Apr. 1998, p. R8115-R8118.

[34] N.D. Mathur, M.-H. Jo, J.E. Evetts, and M.G. Blamire, "Magnetic anisotropy of thin film $La_{0.7}Ca_{0.3}MnO_3$ on untwinned paramagnetic $NdGaO_3$ (001)," *Journal of Applied Physics*, vol. 89, 2001, p. 3388.

[35] R. Zheng, Y. Wang, J. Wang, K. Wong, H. Chan, C. Choy, and H. Luo, "Tuning the electrical properties of $La_{0.75}Ca_{0.25}MnO_3$ thin films by ferroelectric polarization, ferroelectric-field effect, and converse piezoelectric effect," *Physical Review B*, vol. 74, Sep. 2006, pp. 1-8.

[36] C. Thiele, K. Dörr, O. Bilani, J. Rödel, and L. Schultz, "Influence of strain on the magnetization and magnetoelectric effect in $La_{0.7}A_{0.3}MnO_3$/PMN-PT(001) (A=Sr,Ca)," *Physical Review B*, vol. 75, Feb. 2007, pp. 1-8.

[37] R. Zheng, Y. Wang, H. Chan, C. Choy, and H. Luo, "Determination of the strain dependence of resistance in $La_{0.7}Sr_{0.3}MnO_3$/PMN-PT using the converse piezoelectric effect," *Physical Review B*, vol. 75, Jun. 2007, pp. 1-4.

[38] R. Zheng, C. Chao, H. Chan, C. Choy, and H. Luo, "Converse piezoelectric control of the lattice strain and resistance in $Pr_{0.5}Ca_{0.5}MnO_3$/PMN-PT structures," *Physical Review B*, vol. 75, Jan. 2007, pp. 1-6.

[39] M. Angeloni, G. Balestrino, N.G. Boggio, P.G. Medaglia, P. Orgiani, and A. Tebano, "Suppression of the metal-insulator transition temperature in thin $La_{0.7}Sr_{0.3}MnO_3$ films," *Journal of Applied Physics*, vol. 96, 2004, p. 6387.

[40] R. Zheng, Y. Jiang, Y. Wang, H. Chan, C. Choy, and H. Luo, "Ferroelectric poling and converse-piezoelectric-effect-induced strain effects in $La_{0.7}Ba_{0.3}MnO_3$ thin films grown on ferroelectric single-crystal substrates," *Physical Review B*, vol. 79, May. 2009, pp. 1-7.

[41] A. J. Millis, T. Darling, and A. Migliori, "Quantifying strain dependence in 'colossal' magnetoresistance manganites," *Journal of Applied Physics*, vol. 83, 1998, p. 1588.

[42] T. Kanki, T. Yanagida, B. Vilquin, H. Tanaka, and T. Kawai, "Hall effect in strained $La_{0.85}Ba_{0.15}MnO_3$ thin films," *Physical Review B*, vol. 71, Jan. 2005, pp. 2-4.

[43] Y.A. Boĭkov and V.A. Danilov, "Response of the Electrical Resistance of $La_{0.67}Ca_{0.33}MnO_3$ (40 nm) Films Mechanically Compressed by the Substrate in the Course of Their Formation to Electric and Magnetic Fields," *Physics of the Solid State*, vol. 50, 2008, pp. 451-455.

[44] Y.A. Boĭkov and V.A. Danilov, "Electrical resistivity and magnetotransport properties of $La_{0.67}Ba_{0.33}MnO_3$ epitaxial films biaxially compressed by the substrate," *Physics of the Solid State*, vol. 49, Aug. 2007, pp. 1523-1527.

[45] D. Wang, C. Xiong, G. Liu, Y. Xie, B. Shen, and J. Sun, "Effects of oxygen content on the transport property of $La_{0.7}Ce_{0.3}MnO_{3+\delta}La_{0.7}Ce_{0.3}MnO_{3+\delta}$ film," *Physica B: Condensed Matter*, vol. 371, 2006, pp. 187-191.

[46] O.Y. Gorbenko, R.V. Demin, a R. Kaul', L.I. Koroleva, R. Szymczak, H. Szymczak, and M. Baran, "Crystallographic, magnetic, and electrical properties of thin $Re_{0.6}Ba_{0.4}MnO_3$ epitaxial films (Re = La, Pr, Nd, Gd)," *Physics of the Solid State*, vol. 46, Jul. 2004, pp. 1255-1261.

[47] Z. Trajanovic, L. Senapati, and R. Sharma, "Stoichiometry and thickness variation of $YaBa_2Cu_3O_{7-x}$ in off-axis pulsed laser deposition," *Applied Physics Letters*, vol. 66, 1995, p. 2418.

[48] P. Mozhaev, "Fabrication and properties of epitaxial heterostructures of high-temperature superconductor $YBa_2Cu_3O_x$", Ph.D. thesis, 1999.

[49] M.B. Korzenski, P. Lecoeur, B. Mercey, D. Chippaux, B. Raveau, and R. Desfeux, "PLD-Grown Y_2O_3 Thin Films from Y Metal: An Advantageous Alternative to Films Deposited from Yttria," *Chemistry of Materials*, vol. 12, Oct. 2000, pp. 3139-3150.

[50] T. Okada, K. Kawashima, Y. Nakata, and X. Ning, “Synthesis of ZnO Nanorods by Laser Ablation of ZnO and Zn Targets in He and O_2 Background Gas,” *Japanese Journal of Applied Physics*, vol. 44, p. 688 LP - 691.

[51] A.J. Ying, C.E. Murray, and I.C. Noyan, “A rigorous comparison of X-ray diffraction thickness measurement techniques using silicon-on-insulator thin films,” *Journal of Applied Crystallography*, vol. 42, Apr. 2009, pp. 401-410.

[52] P.B. Mozhaev, A. Kühle, G.A. Ovsyannikov, and J.L. Skov, “Pulsed laser deposition of high-Tc superconducting $YaBa_2Cu_3O_x$ thin films in Ar/O_2 atmosphere,” *Czechoslovak Journal of Physics*, vol. 46, 1996, pp. 1519-1520.

[53] D. Blank, “Epitaxial growth of oxides with pulsed laser interval deposition,” *Journal of Crystal Growth*, vol. 211, Apr. 2000, pp. 98-105.

[54] Y.A. Bo and V.A. Danilov, “Electrical Resistivity and Magnetotransport Compressed by an $NdGaO_3$ (001) Substrate,” *Text*, vol. 50, 2008, pp. 95-100.

[55] Y. a Boikov, R. Gunnarsson, and T. Claeson, “Strain-enhanced phase separation affecting electro- and magnetotransport in $La_{0.67}Ca_{0.33}MnO_3$ films,” *Journal of Applied Physics*, vol. 96, 2004, p. 435.

[56] L. Ranno, a Llobet, R. Tiron, and E. Favre-Nicolin, “Strain-induced magnetic anisotropy in epitaxial manganite films,” *Applied Surface Science*, vol. 188, Mar. 2002, pp. 170-175.

[57] S.V. Trukhanov, a V. Trukhanov, H. Szymczak, C.E. Botez, and a Adair, “Magnetotransport Properties and Mechanism of the A-Site Ordering in the Nd–Ba Optimal-Doped Manganites,” *Journal of Low Temperature Physics*, vol. 149, Aug. 2007, pp. 185-199.

[58] Gajek, “Growth and magnetic properties of multiferroic $La_xBi_{1-x}MnO_3$ thin films,” *Physical Review B (Condensed Matter and Materials Physics)*, vol. 75, 2007, p. 174417.

[59] S. Seiro, E. Koller, Y. Fasano, and O. Fischer, “Homogeneous strain-relaxation effects in $La_{0.67}Ca_{0.33}MnO_3$ films grown on $NdGaO_3$,” *Applied Physics Letters*, vol. 91, 2007, p. 091913.

[60] S. Kang, a Goyal, J. Li, a a Gapud, P.M. Martin, L. Heatherly, J.R. Thompson, D.K. Christen, F. a List, M. Paranthaman, and D.F. Lee, “High-performance high-TC superconducting wires.,” *Science (New York, N.Y.)*, vol. 311, Mar. 2006, pp. 1911-4.

[61] H. Huhtinen, M. Peurla, M. a Shakhov, Y.P. Stepanov, P. Paturi, J. Raittila, R. Palai, and R. Laiho, “Superconducting Properties of Films Deposited From Micro-, Nanocrystalline and Optimally BZO-Doped YBCO Targets,” *IEEE Transactions on Applied Superconductivity*, vol. 17, Jun. 2007, pp. 3620-3623.

[62] A. Crisan, M.M. Awang Kechik, P. Mikheenko, V.S. Dang, A. Sarkar, J.S. Abell, P. Paturi, and H. Huhtinen, “Critical current density and pinning potential in $YBa_2Cu_3O_{7-\delta}$ thick

films ablated from a $BaZrO_3$ -doped nanocrystalline target," *Superconductor Science and Technology*, vol. 22, 2009, p. 045014.